Beeldgebaseerde stromingsanalyse van microscopisch kleine biologische systemen

Image Based Flow Analysis of Microscale Biological Systems

Frédéric Maes

Promotoren: prof. dr. ir. P. Verdonck, prof. dr. ir. P. Van Ransbeeck
Proefschrift ingediend tot het behalen van de graad van
Doctor in de Ingenieurswetenschappen

Vakgroep Civiele Techniek
Voorzitter: prof. dr. ir. J. De Rouck
Faculteit Ingenieurswetenschappen en Architectuur
Academiejaar 2012 - 2013

UNIVERSITEIT GENT

ISBN 978-90-8578-541-5
NUR 954
Wettelijk depot: D/2012/10.500/67

Promotoren

prof. dr. ir. Pascal Verdonck
dr. ir. Peter Van Ransbeeck

Samenstelling van de examencommissie

prof. dr. ir. Hendrik Van Landeghem (voorzitter)
FEA – Universiteit Gent
prof. dr. ir. Patrick Segers (secretaris)
FEA – Universiteit Gent
prof. dr. ir. Pascal Verdonck
FEA – Universiteit Gent
dr. ir. Peter Van Ransbeeck
GTI – Hogeschool Gent
prof. dr. Bill Chaudhry
Newcastle University, UK
prof. dr. ir. Hans Van Oosterwyck
Katholieke Universiteit Leuven
dr. ir. Tom Claessens
GTI – Hogeschool Gent
prof. dr. ir. Stefaan Vandenberghe
FEA – Universiteit Gent
prof. dr. ir. Jan Vierendeels
FEA – Universiteit Gent

ACKNOWLEDGEMENTS

The part you write last of all, rushing against time to reach the ultimate deadline, because, being a professional procrastinator, you hope, against all odds, that they will grant you an extra day. They have trained you to check and recheck every sentence and put at least 10 references with every quote. Now you have to write something about yourself…

This is pretty much my story. The following manuscript originates in the heads of two people. First Prof. Hans Van Oosterwyck, a very dedicated researcher at the Katholieke Univeristeit Leuven, came to question why cells sometimes respond differently in tissue engineered constructs with comparable geometrical characteristics. Some time later Prof. Bill Chaudhry a genius multitasker from the University of Newcastle (UK) for years performing research on developmental cardiac genetics came to question how the embryonic heart is physically pumping. Both came in contact with Prof. Pascal Verdonck, a scientific heavyweight in biomedical engineering circles, at that time the head of the IBiTech research group at Ghent University. Meanwhile a very ambitious Dr Peter van Ransbeeck started up a research unit at University College Ghent containing only one inexperienced person…

And of course it went like everybody knows but no one likes to admit: research is passed on until it reaches the person who is not able to pass it on anymore. This sounds more negative than it is in reality. I've had the privilege to struggle with computer programs who's main job seems to throw errors, to investigate data that are only used because there are no better and postulate conclusions where the world does not agree with; all joys that others have to miss.

Off course I was lucky to have some assistance from real researchers. Dr. Saartje Impens, whom I've never met in person, is responsible for all the experimental data about tissue engineering. Dr Greet kerckhofs who performed the scaffold scanning and Archimedes measurements. Dr Maarten Moessen, the developer of "Democells", without his help I would still be busy manually repairing bad mimics meshes. Dr Silvia Truscello a very smart Italian who provide the oxygen routines for fluent along with all the helpmails when I did again something stupid.

My office coworkers at IBiTech: Koen & Dieter both a with balanced view on soccer and science, Gianlucca trying to teach us the Italian way of life, Peter and Charlotte piling up scientific prices, Matthieu, Abigail, Bram, Thomas, Sofie and former colleagues Sunny, Rado, Guy, Mirko, Jan, Sebastian and Lieve; all showing their love for science.

My peers at BioMech: Tom, a textbook example of a scientist who has the astonishing ability of transforming my gibberish writings into understandable English and is always there to answer any science related question, Matthias, who whatever hard you work always works twice as hard, Mieke, trying to find balance between science, children and house renovations, Benjamin, one of the handiest inventor/scientist I have met and Kim, so zealous that, within few years, even the faculty dean will not be sure of his position.

Special thanks to the members of the Mechanics department who in these turbulent times created a part time dream position for me: low level, and without any scientific obligations, so that I can spent more time on helping others instead of helping myself feeling important and polishing my titles.

Thanks to all the brothers and sisters in the worldwide family of Jehovah's Witnesses helping me to keep focussed on the important things in life.

Nothing of this work would be established without my parents. Of all people they invested the most in me, giving me a head start on the highway called life.

On that way you encounter people. The one that every day makes my eyes glow and my heart rejoice is the one who most of all will be glad that this is over. Sarah especially for you a wholehearted thank you for all the patience and moreover for all the love.

The One that I have to thank most of all is The One who believes in all of us and teaches us that nature in all his beauty and wisdom is more than breathtaking but something you can say thank you for

I shall laud you because
in a fear-inspiring way
I am wonderfully made.
Your works are wonderful,
Psalm 139:4

NEDERLANDSE SAMENVATTING

In dit doctoraatsonderzoek is gefocust op stromingsanalyse van biologische systemen op microschaal waarbij digitale beelden werden gebruikt als input materiaal. Het onderzoek bestaat uit twee delen. Het eerste deel start van µCT beelden waaruit een geometrie wordt gereconstrueerd. Deze wordt geometrie wordt gebruikt als input voor stromingssimulaties. Deze methode werd toepast op onderzoek naar stroming door draagstructuren voor weefselengineering. Het tweede deel vertrekt van microscoopbeeldsequenties en gebruikt beeldverwerkings-technieken voor het bepalen van de stroming van bloed. Dit werd toegepast op het onderzoek van hartontwikkeling in embryo's van zebravissen.

DEEL 1 STROMINGSANALYSE IN DRAAGSTRUCTUREN VOOR BOTWEEFSELENGINEERING

Het doel van botweefselengineering is het maken van structuren met levend botweefsel die kunnen dienen om beschadigd botweefsel te vervangen. De meest gecompliceerde stap in dit proces is het stimuleren van de ingezaaide stamcellen tot het vormen van het gewenste botweefsel. Verschillende factoren kunnen het stimulatieproces beïnvloeden. In deze studie worden wandschuifspanning en zuurstofconcentratie beschouwd.

Er wordt gestart met twee draagstructuren vervaardigd door gelcasten. Beiden zijn van verschillend materiaal maar hebben wel een vergelijkbare poriegrootte en een vergelijkbare porositeit. De ene structuur bestaat uit hydroxyapatiet (de minerale vorm van bot) en de andere uit titanium (een inert metaal). Een voorstudie toonde aan dat cellen proliferatie vertoonden in titanium en niet in hydroxyapatiet. Dit verschil in biologische respons vormt de uitgangsituatie om het verschil in wandschuifspanning en zuurstofconcentratie tussen de twee draagstructuren te onderzoeken.

Door de kleine poriegrootte en de onregelmatige interne geometrie van de draagstructuren is het niet mogelijk om lokale wandschuifspanning en zuurstofconcentratie op te meten met een directe methode. Daarom werd gebruik gemaakt van 430 micro computer tomografie beelden (µCT) met een resolutie van 8µm. Dit digitale model is dan gebruikt als input voor de computer stromingsimulaties (CFD).

Omwille van beperkingen in rekenkracht werd in eerste instantie slechts een deel van de draagstructuur gemodelleerd. Er werd gewerkt met twee concentrische kubusvormige modellen (volume 1mm³ en 3.75mm³) in beide draagstructuren. Er

werd een voorstuk geplaatst aan de inlaat waardoor een snelheid van 34µm/s werd opgelegd (corresponderend met een debiet van 0.04ml/min door een inlaatdoorsnede van 5mm). Er werd een gemiddelde wandschuifspanning bekomen van 1.10 mPa voor het 1 mm³ model van hydroxyapatiet en 1.46 mPa voor het 3.75 mm³ model. Beide titanium modellen vertoonden een gemiddelde wandschuifspanning van 1.40 mPa en 1.95 mPa respectievelijk voor het 1 mm³ en het 3.75 mm³ model. De verschillen tussen de modellen binnen dezelfde draagstructuur reflecteren de invloed van de randvoorwaarden bekomen door het sluiten van kanalen bij het uitsnijden van het model. Om de invloed van deze onrealistische randvoorwaarden te onderzoeken werden er concentrische zones afgebakend waarbinnen de wandschuifspanning werd berekend. Door dit te doen voor zones van verschillende grootte kon de invloed van de naburigheid van de randvoorwaarde gekwantificeerd worden. Op basis van onze resultaten werd de suggestie gedaan om de wandschuifspanning te berekenen in een zone die ten minste één poriegrootte verwijderd is van de modelrand.

Het vorige onderzoek kon geen relatie aantonen tussen wandschuifspanning en celproliferatie omwille van problemen met de modelgrootte en onrealistische randvoorwaarden. Daarom werd een CFD model gemaakt van de volledige draagstructuur. Een inlaatdebiet van 0.04 ml/min resulteerde in en gemiddelde wandschuifspanning van 1.41mPa voor titanium en 1.09 voor hydroxyapatiet. Ook hier was de distributie van de schuifspanning niet significant verschillend tussen beide structuren. Bijkomend werd het rekendomein opgesplitst in zones met een verschillende grootte met de bedoeling inzicht te krijgen in de vereiste modelgrootte. Op basis van onze resultaten werd een modelgrootte voorgesteld van 6 -10 maal de gemiddelde poriegrootte.

Om uit te maken of hypoxia (zuurstoftekort) een oorzaak zou kunnen zijn van het verschil in biologische respons tussen beide structuren werd een zuurstofverbruik algoritme gekoppeld aan de CFD modellen. Gedetailleerde modellen van de volledige interne microstructuur geven aan dat er lokale zones zijn in de hydroxyapatiet draagstructuur waar zuurstoftekort optreedt. Deze zones vormen een mogelijk verklaring voor de afwezigheid van proliferatie in deze structuur. Bijkomend werd onderzoek gedaan naar het belang van gedetailleerde modellen door onze resultaten te vergelijken met resultaten bekomen uit gemiddelde waarden. Op basis van gemiddelde waarden kon er geen enkel onderscheid gemaakt worden tussen beide draagstructuren. Dit ondersteunt dat submodellen en model bestaande uit eenheidcellen niet bruikbaar zijn om lokale verschillen in zuurstofconcentratie te onthullen.

DEEL 2: HOE POMPT HET HART VAN EEN EMBRYO

Het embryonale hart is het eerste orgaan dat begint te functioneren. Nochtans is er nog altijd discussie over wat de werkingsmechanisme is van dit tubulaire hart zonder kleppen. Er bestaan twee modellen voor dit pompmechanisme: peristalsis en dynamische zuigpomp. Het voornaamste verschil is het aantal actieve contracties, een dynamische zuigpomp is gekenmerkt door één actieve terwijl peristalsis er meerdere heeft.

Het doel van dit onderzoek is daarom een beter inzicht te verkrijgen in het pompmechanisme van het embryonale hart. In ons onderzoek is dit uitgevoerd in twee stappen: door bloedsnelheidsmetingen in de aorta en door vastleggen van de beweging van het myocardium (hartspierwand). Als input werd gebruik gemaakt van beelden opgenomen via een normale lichtmicroscoop aan 207 frames/s.

Voor de eerste stap werd een snelle en betrouwbare methode uitgewerkt voor het opmeten van bloedsnelheden in de aorta. De snelheden worden berekend door detectie van de verplaatsing van rode bloedcellen. Voorafgaand werden de beelden bewerkt om de achtergrond te verwijderen door middel van het aftrekken van opeenvolgende beelden of een procedure om de achtergrond te herkennen op basis van verschillende beelden. Voor het berekenen van de snelheden werden vier verschillende methodes ontwikkeld. Één is de automatische detectie en het tracken van bloedcellen de andere drie zijn gebaseerd op micro Particle Image Velocimetry (µDPIV) waarbij beweging van frames wordt opgemeten. Alle methodes werden getest op nauwkeurigheid en robuustheid ten opzichte van zorgvuldig handmatig tracken van rode bloedcellen. De µDPIV methodes toonden aan superieur te zijn in nauwkeurigheid robuustheid en rekentijd ten opzichte van alle andere methodes.

Het bloedsnelheidsalgoritme werd vervolgens toegepast voor het onderzoek naar invloed van leeftijd op de stroming van het bloed en de werking van het hart. Er werd aangetoond dat de maximale snelheid en de maximale acceleratie stijgen met de leeftijd. Dit komt overeen met een toegenomen contractiliteit van het hart. Daarnaast werd ook de invloed van 2.3-butadionemonoxime (BDM) bekeken, een agens dat de spiercellen loskoppelt van het sturende elektrische signaal in het hart. Onze testen toonden een daling van het hartminuutvolume, het slagvolume, de maximale snelheid en de piekacceleratie, allemaal indicatief voor hartfalen. Ook was er een daling van de minimale snelheid wat kan duiden op een verhoogde terugstroming door een incomplete contractie van de hartwand.

Voor de tweede stap werden twee manieren uitgewerkt om te onderzoeken hoe de beweging van de hartwand wordt geactiveerd. Ten eerste werd de beweging van een normaal hart vergeleken met een visualisatie van het elektrische signaal bekomen uit de literatuur. Beiden toonden een parallel verloop wat doet vermoeden dat de

hartwand actief wordt aangestuurd. Ten tweede werd er gebruik gemaakt van een lage dosis medicatie die wordt gebruikt om de connectie tussen de hartwand en het aansturend elektrische signaal te onderbreken. De resultaten toonden een verlaging van de contractiliteit maar deze was enkel lokaal zichtbaar door een zone die niet reageerde en niet over de volledige lengte zoals de bloedsnelheidsmetingen lieten vermoeden. Deze stationaire zone is een onmogelijke situatie in een hartmodel met slechts één actieve contractie waarvan de rest van de beweging wordt veroorzaakt door passieve golven. Dit is dus een argument voor een peristaltische werking van het hart.

De literatuur toont echter aan dat de stroming in het hart gekarakteriseerd wordt door een zuigwerking die niet voorkomt bij een peristaltische pomp. Er werd verondersteld dat de zuigwerking wordt veroorzaakt door de gel die zich bevindt tussen het myocardium en het endothelium (cellaag in contact met het bloed). De gellaag versterkt de amplitude van de contractie en de literatuur toont aan dat er zich elastische moleculen bevinden die het terugveren van de wand kunnen induceren. Dit terugveren van de wand kan een verklaring zijn voor de zuigwerking beschreven in de literatuur. Er werd een nieuw model voorgesteld voor de werking van het embryonale hart waarbij de peristaltische beweging gecombineerd wordt met het elastische effect van de gellaag.

ENGLISH SUMMARY

This doctoral research has focused on image based flow analysis in microscale biological systems using images as input data. It consists of two parts. In the first part we started from µCT images to create a geometrical model as input for computational fluid dynamic simulations. We applied this to the study of flow through scaffolds (support structures) for bone tissue engineering. In the second part we started from microscope images sequences and applied image processing techniques to study the blood flow in zebrafish embryos.

PART 1: ANALYSIS OF FLOW IN SCAFFOLDS FOR BONE TISSUE ENGINEERING

The aim of bone tissue engineering is to create viable bone tissue constructs in order to repair the damaged tissue. The most difficult step in the tissue engineering process is the incubation where the seeded stem cells need to differentiate into the desired tissue. Several factors are known to influence the differentiation of stem cells. In the investigation we focused on wall shear stress exerted on the cells and oxygen availability.

As a proof of principle we started from two irregular scaffolds created through gel casting. Both have comparable pore size and porosity but they are of different material: hydroxyapatite (the mineral form of bone) and titanium (an inert metal). A preliminary experimental study showed that in the titanium scaffold cells proliferated whereas they did not in the hydroxyapatite scaffold, making these scaffolds ideal models to study differences in local wall shear stress and oxygen tension.

Because of the microscale of the pores and the irregular internal architecture of the scaffolds, direct measuring of both local shear stress and local oxygen tension is not possible. Therefore we used 430 micro computed tomography images with a resolution of 8 µm to reconstruct the scaffold geometry. This digital model is then used as input for the computational fluid dynamics (CFD) simulations.

Due to limited computational resources we first created CFD models of only a part of the entire scaffold. To tackle the tradeoff between model size and mesh resolution we created two concentric models (cubes with a volume of 1 mm^3 and 3.375 mm^3, respectively) for both scaffolds. A flow guidance was placed in front of the real inlet surface of the scaffold to mimic realistic inlet conditions. With a flow rate of 0.04 ml/min perfused through a 5 mm diameter scaffold at an inlet velocity of 34 µm/s we obtained an average wall shear stress of 1.10 mPa and 1.46 mPa for the 1 mm^3 and the 3.375 mm^3 model of the hydroxyapatite scaffold compared to 1.40 mPa and

1.95 mPa for the 1 mm³ model and the 3.375 mm³ model of the Titanium scaffold. The discrepancies between two concentric models of the same scaffold demonstrate the important influence of unrealistic boundaries, inevitable when flow channels are chopped off due to model selection. To assess that influence we selected concentric cubic portions, in which the wall shear stress data were calculated. The cubic portions had the same size and the same location within both 1mm³ and 3.375 mm³ cubic models. Varying the size of the inner portions simultaneously in both model selections gives a quantification of the sensitivity to boundary neighborhood. We found out that wall shear stress should be estimated on a region that is one pore size away from the model boundary.

The wall shear stress results of the previous study were inconclusive because of problems with model size and unrealistic boundary conditions. Therefore we created CFD models of the complete scaffold. Imposing a 0.04 ml/min flow rate resulted in a surface area averaged wall shear stress of 1.41 mPa for titanium and 1.09 mPa for hydroxyapatite. The distribution of wall shear stress was not found to be significantly different between both structures. Additionally we subdivided the domain in regions of different size, in order to get insight in required model size. From our results we propose a model size between 6 and 10 times the average pore size.

To find out if hypoxia could be causing the difference in cell proliferation we added an oxygen consumption routine to the CFD models. Through detailed modelling of the entire micro architecture we could demonstrate that the hydroxyapatite scaffold suffers from local zones of low oxygen tension. These hypoxic zones likely are the cause of the rather disappointing cell proliferation in the hydroxyapatite scaffold during *in vitro* culture. In addition we investigated the importance of modelling scaffold micro architecture by comparing our results with averaged oxygen tension values which were incapable of showing any distinction between both structures. This emphasises that sub models and models consisting of unit cells cannot be used to study local differences in oxygen tension.

PART 2: EMBRYONIC HEARTS: HOW DO THEY PUMP

The embryonic heart is the first organ to start functioning. yet today its pumping mechanism in tubular heart stage is still subject of debate. Two pumping models exist for this valveless, tubular shaped heart: peristalsis and dynamic suction. The main difference between the two is the number of active contractions, dynamic suction has one whereas peristalsis is characterized by a number of adjacent cells actively contracting.

The aim of this investigation therefore is to get better insight in the pumping mechanism of the embryonic heart. We did this in two steps: through aortic velocity measurement and through myocardial (heart muscle) wall tracking. Input material for the investigations were bright field microscopic images series of zebrafish embryos taken at 207 frames/s.

During the first step we created a fast and reliable method capable of detecting changes in aortic blood flow. Aortic velocity in zebrafish is estimated through detection of displacement of red bloods cells. Images were preprocessed to remove the background. We used image subtraction and background learning. To capture velocities four different methods were developed; one is automated cell detection and tracking, the three others are based on micro digital particle image velocimetry (µDPIV) where motion of frames are assessed. All methods were evaluated by comparison with careful manual tracking and compared with the linescan method, the only available method reported in literature. The µDPIV based methods were found to outperform all other methods in terms of accuracy, robustness and processing time.

The blood velocity estimating algorithm is used to investigate aortic blood flow changes during development. We found that, besides heart rate, also maximal velocity and peak acceleration increased, indicating an increase of heart contractility. We also investigated the effect of different doses of 2.3-butadionemonoxime (BDM), a drug that uncouples myocardial wall contraction from the governing electrical signal. Our tests displayed a decrease in cardiac output, stroke volume, maximal velocity and peak acceleration, all indicative of a decrease in contractility. Also minimal velocity decreased, indicating an increase in backflow and thus an incomplete occlusion of the myocardial wall.

In the second step we used two pathways to investigate how the heart wall is activated. Firstly we carried out a detailed study of the heart wall motion in normal embryos and compared this with a quantification of the magnitude of the electrical signal reported in literature. Both show parallel behaviour suggesting active contracting in the entire wall. Secondly, we used low doses BDM to pharmacologically disconnect the electrical signal - contraction relationship in order to induce abnormal wall motions. Results show loss of contractility but only local instead of a general weakening of the contractions suggested by the aortic velocity measurements. One zone did not move whereas the adjacent cells responded normally. This stationary zone is impossible in a model consisting of only one contraction where the wall motion is caused by passive wave travelling, instead it indicates that the hearts wall is peristaltically activated.

Literature however demonstrated that fluid dynamics in the embryonic heart show characteristics that are typical for a suction phenomenon, thus contradicting peristalsis. We hypothesize that this suction is caused by the cardiac jelly, an acellular matrix between the myocardial wall and the endothelial wall in contact with the blood. This cardiac jelly amplifies the contraction amplitude and literature demonstrated the presence of elastic molecules likely to cause recoil after deformation. This recoil could induce the suction effect observed in literature. We propose the combination of peristaltic wall activation with recoil of the cardiac jelly as a new model for the pumping mechanism of embryonic heart.

ABBREVIATIONS

Part A

µCT	micro computed tomography
ALP	alkaline phosphatase
BTE	bone tissue engineering
CFD	computational fluid dynamics
HA	hydroxyapatite
HIF alpha	Hypoxia-Inducible Factor alpha
hPDC	human Periosteum Derived Cell
TE	Tissue Engineering
Ti	Titanium
WSS	Wall Shear Stress

Part B

µDPIV	micro Digital Particle Image Velocimetry
BDM	2,3-butanedionemonoxime (drug)
dpf	days post fertilization
hpf	hours post fertilization
IDL	Interactive Data Language (tracking algorithm)
MM	Michaelis Menten
PIV	Particle Image Velocimetry

PREFACE

This manuscript consists of two parts, each applying image based flow analysis on a micro scale biological system.

The first part investigates flow through support structures for tissue engineering. Prof. Hans Van Oosterwyck head of the mechanobiology subdivision of the Prometheus skeletal tissue engineering division at Katholieke Universiteit Leuven is specialized in experimental and computational studies of bone tissue engineering. From experiments performed by Dr. Saartje Impens in collaboration with the group of Prof. Jan Schrooten was found that bone tissue growth responses differently in structures of comparable geometrical properties but made from different materials. Since bone tissue is cultured by perfusion of a culture medium the question arises if differences in internal fluid dynamic environment could explain the dissimilarities in biological response.

The second part investigates aortic flow and the pumping mechanism of hearts of vertebrate embryos. Prof. Bill Chaudhry of the Institute of Human Genetics at Newcastle University is specialized in genetics of vertebrate heart development. As research of heart development involves a lot of comparative tests the question raised if it was not possible to quantify heart condition through an easy measure of the aortic flow. And since the current embryonic heart pumping model is still subjected to a lot of debate the question was extended to unravelling the working principle of the embryonic heart.

Both investigations are characterized by their micro scale, implicating that direct measurement of flow parameters is not possible. Therefore in both studies we start from microscopic imaging techniques and use algorithms to estimate flow characteristics. Because of the nature of the biological systems investigated, two different types in input images were used. The first part starts from 3D µCT images and uses Computational Fluid Dynamics (CFD) to estimate flow. In the second part we started from microscope images sequences and applied image processing techniques to study the blood flow in zebrafish embryos.

PART A:

ANALYSIS OF FLOW IN IRREGULAR SCAFFOLDS FOR BONE TISSUE ENGINEERING

Chapter 1 PROLOGUE

This prologue invites you with a brief introduction. After depicting tissue engineering as an alternative for current bone regeneration procedures it deploys the organisation of this investigational part and postulates the research goals.

1. 1. INTRODUCTION

Jules Verne is for many people one of the inventors of science fiction but he would never have thought of people once cultivating organs.

In the early 90's however a very ambitious concept has been elucidated by Robert Langer, Joseph Vacanti, Linda Grifith and their colleagues working at Massachusetts Institute of Technology (MIT) and Harvard, Cambrigde (Langer and Vacanti 1993; Langer and Vacanti 1999). They introduced Tissue Engineering (TE) as

> *"an interdisciplinary field that applies the principles of engineering and life sciences toward the development of biological substitutes that restore, maintain, or improve tissue function or a whole organ"*
> *(Langer and Vacanti 1993) Science.*

The definition of the field undergoes an implicit expansion when adjacent fields report advances that appear to address core challenges in tissue engineering. A typical example is the emergence of stem cell research. A broader, more applied definition sounds as follows:

> *"understanding the principles of tissue growth, and applying this to produce functional replacement tissue for clinical use."*
> *(MacArthur and Oreffo 2005) Nature.*

However 20 years and over 12 000 articles later only an embarrassing few number of bone tissue engineering applications are currently clinically used (Hollister and Murphy 2011). This is not surprising because, despite the widespread idea of life being evolved by chance, mimicking nature to create living tissues is an issue that appears a lot more complicated than initially thought.

1. 1. 1. Basic steps in bone tissue engineering (BTE)

Following steps are generally taken in BTE (Figure 1-1). BTE makes use of osteoprogenitor cells harvested from a donor (cell extraction *(1)*) and expanded in

vitro to reach a sufficient amount (proliferation *(2)*). Afterwards, cells are seeded into a support structure or scaffold (seeding *(3)*). Under optimized conditions cells develop the desired tissue (incubation *(4)*). Finally the BTE construct is implanted into the bone defect and allows physiological healing (implantation *(5)*)

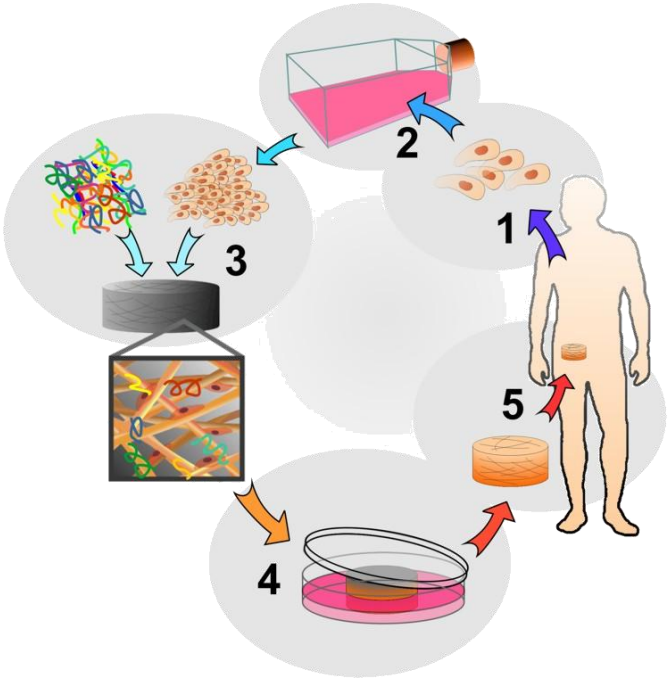

Figure 1-1: flow chart of tissue engineering steps [reproduced from (Van Blitterswijk et al. 2008)]

The most critical step in the complete cycle remains the incubation. Several biological and environmental conditions need to be fiddled adequately in order to obtain a viable construct.

The main motivation for this research part is to get a better insight in the fluid environmental conditions inside the support structure by use of computer simulations. The insights gained could be of use in the design of scaffolds for bone tissue engineering.

1. 2. ORGANISATION

Our approach was to investigate the fluid environment surrounding the seeded cells in a scaffold through computer simulations. This necessitates high resolution images from which the 3D internal geometry can be reconstructed. From this a mesh suitable for computational fluid dynamics (CFD) calculations needs to be made. Creating the necessary input, performing the CFD simulations and analyzing data required demonstrations of principles from biology and engineering.

This research is built upon three milestones which are discussed in deep in the following chapters

- Evaluation of CFD sub model for two scaffold materials
- Models of complete geometries to evaluate sub model limitations
- Simulation of oxygen concentration in two complete scaffold geometries and comparison with in vitro results

Chapter 2 *Introduction to modelling fluid flow in scaffolds for bone tissue engineering.*
This chapter provides background information on BTE. We review scaffold material and design criteria and different bioreactor types to create favorable conditions. We describe the modeling strategies currently used in literature and describe the important environmental parameters and their influence on tissue formation.

Chapter 3 *Modelling fluid flow through scaffolds for perfusion bioreactors*
CFD simulations were carried out on two scaffolds of different material but with similar geometrical characteristics. The rationale behind this investigation is trying to understand different behavior during *in vitro* culture of both scaffolds through assessment of fluid-dynamic parameters such as wall shear stress and pressure.

Chapter 4 *Computational Models for Wall Shear Stress Estimation in Scaffolds: a Comparative Study of two Complete Geometries*
Because of geometrical complexity nearly all reported studies in literature based their CFD model on a sub model of the entire scaffold assuming that the model covers the heterogeneity of the scaffolds sufficiently, however, no guidelines exist in this matter. In order to get insight in required model size we subdivided the domain in regions of different size. The proposed guidelines are reflected on studies reported in literature.
All simulations where carried out on the same samples as in chapter 3 in order to facilitate comparison.

Chapter 5 *Oxygen-distribution in Irregular Bone Scaffolds: in silico and in vitro study*
In vitro experiments show that cell proliferation in hydroxyapatite (HA) scaffolds is less than in titanium (Ti) scaffolds despite the favorable material properties of the HA scaffold. As the previous CFD simulations could not give a suitable explanation for this phenomenon we extend the models with a user defined function capable of simulating oxygen distribution inside a scaffold. The simulation results are compared to the results of in vitro experiments. Simulations are done on the same scaffolds as in the two previous chapters.

1. 3. GOALS

The major goal of this study is to develop a CFD model for estimating fluid environmental parameters in order to enhance insight in incubation behavior of irregular scaffolds. Along the way two intermediate technical goals were established

- Guidelines for CFD model preparation of irregular structures
- Explanations for the different response between two constructs of different material

1. 4. REFERENCES

Hollister, S. J. and W. L. Murphy (2011). "Scaffold Translation: Barriers Between Concept and Clinic." Tissue Engineering Part B-Reviews **17**(6): 459-474.

Langer, R. and J. P. Vacanti (1993). "TISSUE ENGINEERING." Science **260**(5110): 920-926.

Langer, R. S. and J. P. Vacanti (1999). "Tissue engineering: The challenges ahead." Scientific American **280**(4): 86-89.

MacArthur, B. D. and R. O. C. Oreffo (2005). "Bridging the gap." Nature **433**(7021): 19-19.

Van Blitterswijk, C. A., L. Moroni, J. Rouwkela, R. Siddappa and J. Sohier (2008). Tissue engineering - an introduction. Tissue engineering. C. A. Van Blitterswijk, A. Lindahl, J. Hubbellet al, Academic press**:** 13-36.

Chapter 2 INTRODUCTION TO MODELLING FLUID FLOW IN SCAFFOLDS FOR BONE TISSUE ENGINEERING

In this introduction we focus on different parameters playing a role during bone tissue engineering culture. The design criteria for scaffolds are enumerated and discussed and a review of bioreactors types is given. We describe current modelling strategies and put the parameters simulated in the next chapters in a biological context.

2. 1. INTRODUCTION

Orthopaedic surgeons and traumatologists are daily confronted with bone fractures. Most fractures heal uneventfully, however between 5 and 10 % result in nonunion (Einhorn 1999). Large bone defects that do not naturally heal (such as after tumour resection or trauma) present another clinical challenge.

The concept of tissue engineering elucidated by Robert Langer and Joseph Vacanti (1993) might be a solution to heal large bone defects and to overcome some of the drawbacks caused by current treatments. The current gold standard treatment to stimulate bone regeneration involves harvesting autologous bone chips from the iliac chest and transplanting them to the injury site (Donati et al. 2007). Obvious drawbacks are donor site morbidity and pain. In addition, there is often lack of structural integrity and limited graft material volume (Bauer 2007).

Yet, how promising the concept of tissue engineering might be, currently it remains difficult to create large viable constructs (Griffith et al. 2005). Most often the problems occur during the incubation step where the seeded cells have to develop into the desired tissue.

2. 2. CREATING A FAVOURABLE ENVIRONMENT FOR DEVELOPING BONE TISSUE

2. 2. 1. Scaffolds as support structures

Scaffolds for bone tissue engineering are porous structures which are used as a support structure for large or non healing bone defects. Hollister and coworkers did a lot of research on models for scaffold design optimization According to them a scaffold for bone tissue engineering (BTE) should fulfil the 4F requirements: Form, Function, Fixation and Formation (Hollister 2009).

- Form: the requirement that scaffolds fill complex 3D bone defects.
- Function: the requirement that scaffolds provide temporary mechanical load bearing within bone defects.
- Fixation: the requirement that scaffolds are securely attached to bone at the defect location.
- Formation: the requirement that scaffolds enhance bone formation by providing appropriate mass transport, allowing perfusion and delivering osteoinductive factors.

Formation remains the most difficult to accomplish because a lot of target values are often not known or differ considerably among studies (Hollister and Murphy 2011).

The following three structural scaffold parameters are known to influence tissue formation: Porosity, pore size and permeability:

- Porosity is the relative volume of the scaffold void with respect to the total volume. High porosities are expected to enhance tissue formation due to higher nutrient transport but negatively influence scaffold strength (Van Cleynenbreugel et al. 2006).
- Pore size has been reported to influence cell adhesion (O'Brien et al. 2005) scaffolds with low pore sizes showed higher cell content after seeding however higher pore size seems to favour bone formation (Li, Habibovic et al. 2007).
- Permeability is the ability to allow flow through the scaffold. Higher permeability is reported to positively influence seeding (Melchels et al. 2011) and ultimately bone tissue formation (Mitsak et al. 2011).

2. 2. 2. Bioreactors

A bioreactor is a culture system designed to support or expand a population of cells through dynamic culture and a controlled environment during the culture step of the BTE process (Yeatts and Fisher 2011). This definition provides for a wide array of designs. The most commonly used are spinner flask, rotating wall and perfusion bioreactors (reviewed by (Martin et al. 2004) and more recently by (El Haj and Cartmell 2010; Yeatts and Fisher 2011; Carpentier et al. 2012; Salter et al. 2012)). All of the bioreactor types are developed to overcome the limitations of static incubation which, for larger constructs, often resulted in rim of viable cells encompassing a necrotic core (Sutherland et al. 1986; Meinel et al. 2004)

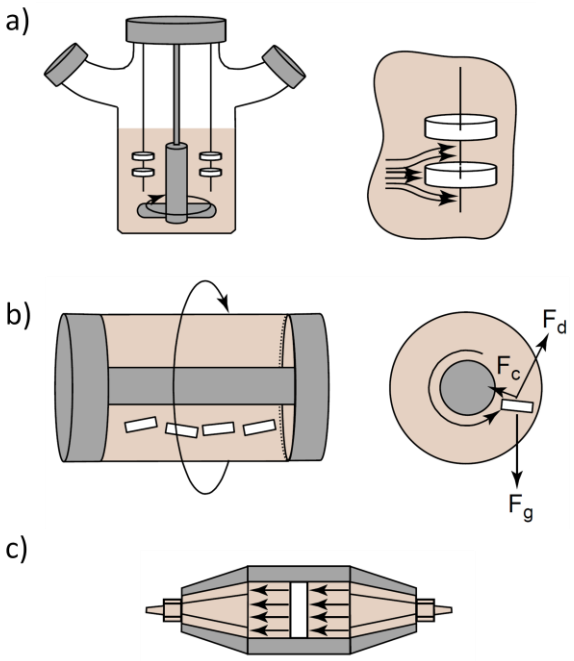

Figure 2-1. Representative bioreactors for bioengineering applications: a) spinner flask, b) rotating wall bioreactor and c) perfusion bioreactor. Adapted from (Martin et al. 2004)

2. 2. 2. a. Spinner flask

Spinner flasks are devices that are used in many disciplines and were among the first to be used in TE. Scaffolds are attached to metal bars and media motion is generated by a magnetic stirrer bar (Figure 2-1a). Several studies point out that spinner flask bioreactors enhance matrix formation compared to static controls. However often is noticed that tissue is only formed at the outer edge of the scaffold (Sikavitsas et al. 2002; Stiehler et al. 2009). Yeats et al. (2011) speculate that in larger scaffolds spinner flask culture does not adequately enhance mass transport and a sharp nutrient gradient results in cell death in the centre of the scaffold. It appears that penetration depth of transport in spinner flask scaffold culture is limited to 1 mm or less (Meinel et al. 2004). The positive results compared to static controls might be explained by shear stress exerted on the scaffold surface which could aid in enhancing osteogenic differentiation (Wang et al. 2009).

2. 2. 2. b. Rotating wall bioreactors

The design of rotating wall bioreactor features two concentric cylinders; an inner stationary cylinder that provides gas exchange and an outer cylinder that rotates (Figure 2-1b). The space between the two cylinders is completely filled with culture media while cell containing scaffolds are placed freely moving in this space. The free movement of the scaffolds leads to a microgravity environment: the

gravitational force is compensated by the drag force exerted on the scaffold. Several studies point out that rotating wall bioreactors are relatively ineffective for the culture of osteoblastic cells (see the following bioreactor comparison studies: (Sikavitsas et al. 2002; Wang et al. 2009). In another study the gene expression was not significantly different from a static control nor was there any proliferation (Goldstein et al. 2001). Also Yu et al. (2004) report no proliferation. It has been hypothesized that the multiple collisions between the scaffolds and the bioreactor wall might be responsible the rather disappointing results. In a follow up study scaffolds of three different densities including one with a specific density less than one (which showed almost no collisions), Yu et al. (2005) showed that the lighter and less colliding scaffold showed increase in calcium composition.

2. 2. 2. c. Perfusion bioreactors

In contrast to the previous systems, perfusion bioreactors actively pump culture medium through a scaffold thus enhancing mass transport. Many different perfusion systems have been developed, but most have a similar design consisting of a culture medium reservoir, a pump, a tubing unit and a perfusion cartridge housing the scaffold (Figure 2-1c). Goldstein et al. (2001) compared spinner flaks, rotating wall bioreactors and perfusion bioreactors with static controls. At 7 days, the perfusion system yielded the most uniform cell density throughout the construct, whereas the other systems showed preferential cell density at the construct boundaries as would be expected for systems in which mass transport into the construct center was insufficient for cell viability. By 14 days, only the perfusion system had statistically significant levels of alkaline phosphatase (ALP) expression. Together, these results demonstrated that only the perfusion system could adequately support uniform bone differentiation throughout the construct.

Several hundreds of studies have been performed using a perfusion bioreactor setup (for reviews see (Yeatts and Fisher 2011; Carpentier et al. 2012)). Many of those studies demonstrate positive results, however, since the system is based on active pumping, flow parameters have to be set correctly (Bancroft et al. 2002; Sikavitsas et al. 2003).

Despite the promising results, perfusion bioreactors show an important drawback for use in clinical applications inherently connected to perfusion. The system is dependent on the media flowing entirely through the scaffold geometry. This works fine for the regular scaffold shapes which fit nicely in the perfusion cartridge. But when it comes to scaffolds engineered to mimic the shape of the bone defect, avoiding side flow is almost impossible in a normal perfusion chamber. This should imply that for every custom built scaffold a new chamber needs to be tailored to fit tightly around the scaffold (for further reading why perfusion bioreactors are currently not used in clinic we refer to the following reviews (Wendt et al. 2005; Martin et al. 2009; Salter et al. 2012).

The fluid flow through scaffolds in a perfusion bioreactor will be the subject of this study and will be further elucidated in the following chapters of the investigation part.

2. 3. BIOLOGICAL CONTEXT OF PERFUSION FLOW RELATED PARAMETERS

As mentioned in §2. 2. 2. c. the success of a perfusion bioreactor in culturing bone tissue is largely due to flow through scaffolds. An interesting study investigated the role of flow in stimulating bone tissue formation (Holtorf et al. 2005). They compared the effect of dexamethasone, a synthetic glucocorticoid hormone used to stimulate osteogenic differentiation, to the effect of fluid induced mechanical stimuli caused by the perfusion itself. The results indicated that perfusion samples with no added dexamethasone showed higher calcium formation than static controls with dexamethasone. Adding dexamethasone to the perfusion reactor further increased calcium production. These results indicate that flow has an important influence on bone tissue formation.
Flow has multiple effects on cells seeded in a scaffold. The two most important effects are shear stress and mass transport (nutrient transport, in particular oxygen, and waste removal). The biological effects of shear stress and oxygen tension will be discussed in the next two paragraphs.

2. 3. 1. The influence of fluid shear stress

In vivo bone continuously remodels in response to mechanical stress. It is hypothesized that *in vivo* these stresses are mainly transmitted via fluid shear stresses (Burger and Klein-Nulend 1999; Sikavitsas et al. 2001). An attempt of measuring fluid shear stress resulted in values between 0.8 and 3 Pa.

In vitro fluid shear stress is believed to stimulate osteogenic differentiation. However it is difficult to evaluate the influence of shear stress in *in vitro* bioreactor conditions since increasing flow not only increases shear stress but also mass transport. To exclude the effect of mass transport while investigating shear stress researchers used fluids with higher viscosity to induce higher shear stresses without changing mass flow (Sikavitsas et al. 2003; Li et al. 2009). A three-fold increase in viscosity, and thus shear stress, resulted in a seven-fold increase of calcium deposition (Sikavitsas et al. 2003).

Since shear stress has an important synergistic effect a lot of attempts have been made to measure shear stress and try to link it with a biological outcome (Figure 2-2).

Besides the magnitude of shears stress also the flow regime might be an important determinant. A study investigated the difference in expression level of osteogenic genes and ALP activity if shear stress was applied continuously compared to intermittently applied shear stress and found higher values for intermittently applied shear stress (Liu et al. 2012). Also oscillatory applied flow has been showed to yield higher expressions (Kavlock and Goldstein 2011; Li et al. 2012).
A schematic view of the biological outcome related to shear stress magnitude is given in Figure 2-2 based on a thorough review of Mc Coy et al. (2010).

As illustrated in Figure 2-2 determining the effect of a biomechanical parameter like shear stress is not a simple operation as “effective” shear stress values tend to vary several orders of magnitude. McCoy (2010) states that the use of non-human cell lines and 2D experimental apparatus can give indications regarding the trends in relation to some of these variables and provide insightful scientific understanding. However transferring data obtained in 2D experiments to 3D bioreactor setups is clearly not straightforward.

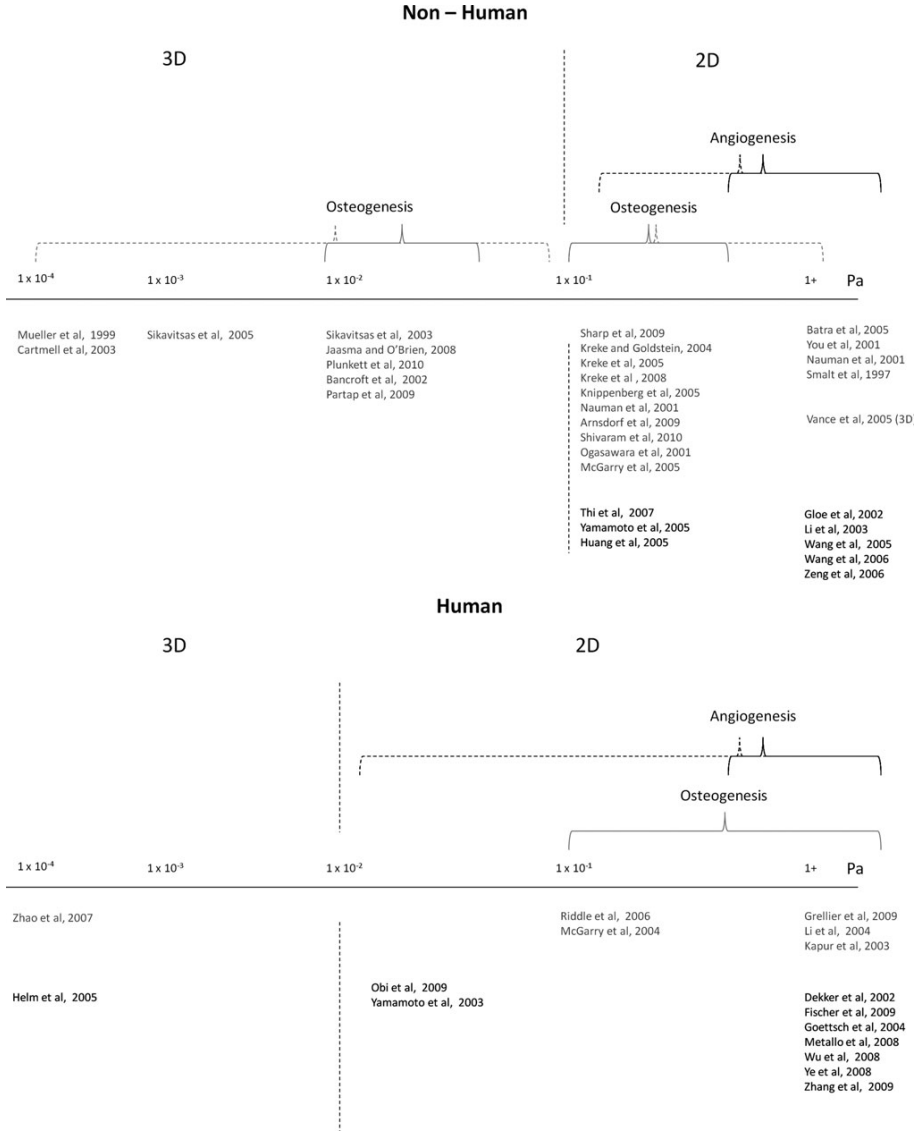

Figure 2-2. Shear stress levels used in experiments for non-human and human cell lines for the induction of osteogenic and angiogenic lineages. Two-dimensional (2D) experiments relate to the application of shear stress on monolayer cultures using a variety of equipment setups: parallel plate flow chambers, radial flow or rotating disc devices, cone and plate viscometers, artificial capillaries, and microfluidic chambers. Three-dimensional (3D) experiments relate to experimental setups using highly porous scaffolds usually in the context of a perfusion bioreactor. References shown are not implemented in the reference list but are added to show the order of magnitude of shear stress applied in the investigation. For detailed references we refer to (McCoy and O'Brien 2010) [reproduced form (McCoy and O'Brien 2010)]

The different behaviour between 2D and 3D setups might be related to the cell attachment morphology (Annaz et al. 2004; Jianbo et al. 2010). Cells in 2D setups are attached in a flat morphology but up to 75% of cells in 3D systems have a bridged morphology (cells are attached across a scaffold channel). It is clear that

cells in a bridged position are more affected by higher shear stress. However this cannot explain the factor 1000 difference in shear stress between 3D systems. We hypothesize a lot of these discrepancies therefore might be explained by the method used for estimating shear stress.

The magnitude of the stress itself, the timing of its application, the flow type, the insertion of rest periods can all influence the cellular response (Yeatts and Fisher 2011). Since there are so many unknown variables a reviewer states that: "The future of shear stress-related investigations should clearly be targeted at filling the current void in knowledge surrounding 3D systems" (McCoy and O'Brien 2010).

The assessment of shear stress in 3D perfusion systems will be the subject of chapter 3 and chapter 4 of this investigation.

2. 3. 2. The influence of oxygen tension

In vivo oxygen is delivered through the cardiovascular system. Osteons (the building blocks of bone) generally consist of different layers of osteoblast (bone forming cells) surrounding the haversian canal in which blood capillaries take care of nutrient and oxygen supply. Transport of oxygen towards the osteoblasts is diffusion driven. Based on numerical modelling using the Krogh cylinder (Krogh 1919), Zahm et al. (2010) estimated that oxygen tension in trabecular bone varies between 5% (near the capillaries) and 1.25% close to the outer ends of the osteon. In the low oxygen zones hypoxia is believed to be a major stimulus for angiogenesis by activating hypoxia-inducible factor alpha (HIF alpha) pathway, which is a central regulator of hypoxia adaptation in vertebrates (Steinbrech et al. 2000). A study has shown that osteoblasts use the HIF alpha pathway to sense reduced oxygen tension and transmit signals that impinge on angiogenic and osteogenic gene programs during bone formation. (Wang et al. 2007) This remodelling strategy ensures sufficient oxygen tension throughout the complete bone structure.

In vitro however the role of oxygen tension and its impact on cell proliferation and differentiation is far less understood and results of experiments often are contradictory. The following study report osteogenesis at low oxygen tension (2-5%) (Lennon et al. 2001) others however report chondrogenesis at 5% oxygen tension (Kanichai et al. 2008). Another comparative study showed that at 5% expansion of mesymchymal stem cells enhanced subsequent osteogenesis whereas differentiation at 5% pO_2 was found to be a more potent promoter of chondrogenesis (Sheehy et al. 2012). Most studies evaluate the effect of hypoxia (2-5% pO_2) compared to the effect of normoxia (20% pO_2). Malladi et al. (2006) showed that osteogenesis is more promoted in normoxia however Qu et al (2012) showed also chondrogenesis, normally hypothesised to developed in hypoxic conditions, was

more promoted by normoxia. Finally Zahm et al. (2008) suggest that the optimal oxygen tension for promoting osteogenesis is in the range of (5-9% pO_2) whereas lower tensions are more promoting chondrogenesis.

Although these results might be interesting, monolayer experiments are not directly transferable to 3D stem cell culture in a scaffold because of the non uniform distribution of cells and nutrients during culture (Melchels et al. 2011). Jontitz et al. (2012) showed increased acidification and a decreased oxygen tension inside a tantalum scaffold cultured under static conditions; as hypothesized by many studies demonstrating the beneficial effect of flow (see § 2. 2. 2. c.). Malda et al. (2004) measured and modelled oxygen tension in 3D cartilaginous constructs and showed a profound decrease of oxygen tension in the central core of the scaffold compared to the oxygen tension closer to the scaffold outer edges.

To the author's knowledge only one study is available where oxygen measurements were performed during perfusion (Volkmer et al. 2008). They compared oxygen tension in scaffolds under static culture conditions with oxygen tension in the same scaffold under perfusion. They found that under static normoxic conditions oxygen decreased to 0% in the central core causing cell death after 5 days of culture. Perfusion successfully prevented cell death however oxygen decreased from 20% to 4%. They conclude that bioreactors prevent cell death but do not eliminate oxygen gradients.

The study of oxygen tension will be the subject of chapter 5.

2. 4. MODELLING FLUID ENVIRONMENT INSIDE A SCAFFOLD FOR BONE TISSUE ENGINEERING

We demonstrated that correctly setting the fluid dynamic environment parameters such as shear stress and oxygen tension in a scaffold is of utmost importance, however there is a major drawback. These parameters, especially shear stress, are almost impossible to measure in a scaffold.
There is one attempt using micro particle image velocimetry to measure the flow field in a regular scaffold (De Boodt et al. 2010). However they used only one scaffold layer because of the 2D nature of their setup. The same method has been used to characterize the 3D hydrodynamics in microcarrier culture spinner vessels for cell culture (Venkat et al. 1996) and for validation of CFD simulation results in a spinner flask (Sucosky et al. 2004). However none can give detailed 3D information of local distribution of shear stress or oxygen tension inside a scaffold.

Today the only way to estimate local shear stress or oxygen tension is by using computational simulation of the fluid dynamic environment in the scaffold void. The

first attempt is reported by Raimondi et al. (2002). They used a 2D CFD approach to investigate local shear stress around the fibres of a fibrous scaffold. Porter et al. (2005) were the first to use a 3D CFD simulation of a scaffold in a perfusion bioreactor. The scaffold geometry was acquired through micro computed tomography (µCT) imaging and they used a Lattice-Boltzmann approach to estimate the fluid flow field. Because their mesh was too coarse to estimate shear stress correctly they proposed a correction factor based on the number of cells in a scaffold channel to estimate the error on shear stress. Cioffi et al. (2006) used the same approach but used a commercial software to solve the Navier-Stokes equations. They focused on modelling small scaffold sample volumes using a very small element size (8 µm) in order to minimize mesh related errors. Although their results were mesh insensitive they are actually prone to errors due to unrealistic boundary conditions since the lateral walls of the model had to be closed in order to run the simulations. In reality those lateral walls do not exist, they are flow providing channels that have been cut off by the CFD model creation. The only way to overcome these artifacts is by modelling an entire scaffold. The only study (to the author's knowledge) reporting a CFD simulation in an entire scaffold is done by Jungreuthmayer et al. (2009). Unfortunately, because their scaffold pore size was in the order of 1 mm, the applied inlet velocity is a factor 1000 higher than what normally is used in bioreactor conditions.

The comparison of the results of sub models with the simulation results of an entire scaffold will be elaborated in chapter 4.

Besides using µCT imaging to acquire the actual geometry of the scaffold a lot of CFD studies have been performed using unit cells. A unit cell is the characteristic volume used as building block to create for example regular scaffolds. The advantage of unit cells is that the CFD simulations are far less computationally demanding. This approach is very valuable for evaluating different scaffold design criteria like pore size and porosity and their influence on shear stress. One of the first reported studies is performed by Boschetti et al. (2006). Another study evaluated different kinds of unit cell shapes and their influence on local shear stress (Olivares et al. 2009). Others connected optimization functions to create unit cells with uniform shear stress distribution (Yuhang et al. 2011) or to create scaffolds with optimized elasticity and permeability (Hollister and Lin 2007). A very interesting study of Truscello et al. (2011) used unit cells to investigate the penetration depth of oxygen in regular scaffolds aiming to set maximal dimensions for scaffolds in other to avoid hypoxic zones.

Obviously modelling results are dependent on parameter settings and as such need to be compared with results of bioreactor experiments. This will be done in the study reported in chapter 5.

2. 5. CONCLUSIONS

In this chapter we discussed some parameters influencing tissue engineering culture. We quoted that today very few bone tissue engineered applications are used in clinic. This is likely due to the limited understanding of the fluid dynamic environment surrounding the cells inside a scaffold. We reviewed the biological impact of oxygen tension and shear stress. Monitoring such parameters during culture represents one of the major challenges. To this respect we discussed the promising role of computational fluid mechanics as a simulation tool in quantifying the fluid dynamic environment in scaffolds in 3D.

2. 6. REFERENCES

Annaz, B., K. A. Hing, M. Kayser, T. Buckland and L. Di Silvio (2004). "Porosity variation in hydroxyapatite and osteoblast morphology: a scanning electron microscopy study." Journal of Microscopy-Oxford **215**: 100-110.

Bancroft, G. N., V. I. Sikavitsas, J. van den Dolder, T. L. Sheffield, C. G. Ambrose, J. A. Jansen and A. G. Mikos (2002). "Fluid flow increases mineralized matrix deposition in 3D perfusion culture of marrow stromal osteloblasts in a dose-dependent manner." Proceedings of the National Academy of Sciences of the United States of America **99**(20): 12600-12605.

Bauer, T. W. (2007). "An overview of the histology of skeletal substitute materials." Archives of Pathology & Laboratory Medicine **131**(2): 217-224.

Boschetti, F., M. T. Raimondi, F. Mighavacca and G. Dubini (2006). "Prediction of the micro-fluid dynamic environment imposed to three-dimensional engineered cell systems in bioreactors." Journal of Biomechanics **39**(3): 418-425.

Burger, E. H. and J. Klein-Nulend (1999). "Mechanotransduction in bone - role of the lacuno-canalicular network." Faseb Journal **13**: S101-S112.

Carpentier, B., P. Layrolle and C. Legallais (2012). "Bioreactors for bone tissue engineering." International Journal of Artificial Organs **34**(3): 259-270.

Cioffi, M., F. Boschetti, M. T. Raimondi and G. Dubini (2006). "Modeling evaluation of the fluid-dynamic microenvironment in tissue-engineered constructs: A micro-CT based model." Biotechnology and Bioengineering **93**(3): 500-510.

De Boodt, S., S. Truscello, S. E. Ozcan, T. Leroy, H. Van Oosterwyck, D. Berckmans and J. Schrooten (2010). "Bi-Modular Flow Characterization in Tissue Engineering Scaffolds Using Computational Fluid Dynamics and Particle Imaging Velocimetry." Tissue Engineering Part C-Methods **16**(6): 1553-1564.

Donati, D., C. Zolezzi, P. Tomba and A. Vigano (2007). "Bone grafting: historical and conceptual review, starting with an old manuscript by Vittorio Putti." Acta Orthopaedica **78**(1): 19-25.

El Haj, A. J. and S. H. Cartmell (2010). "Bioreactors for bone tissue engineering." Proceedings of the Institution of Mechanical Engineers Part H-Journal of Engineering in Medicine **224**(H12): 1523-1532.

Goldstein, A. S., T. M. Juarez, C. D. Helmke, M. C. Gustin and A. G. Mikos (2001). "Effect of convection on osteoblastic cell growth and function in biodegradable polymer foam scaffolds." Biomaterials **22**(11): 1279-1288.

Griffith, C. K., C. Miller, R. C. A. Sainson, J. W. Calvert, N. L. Jeon, C. C. W. Hughes and S. C. George (2005). "Diffusion limits of an in vitro thick prevascularized tissue." Tissue Engineering **11**(1-2): 257-266.

Hollister, S. J. (2009). "Scaffold Design and Manufacturing: From Concept to Clinic." Advanced Materials **21**(32-33): 3330-3342.

Hollister, S. J. and C. Y. Lin (2007). "Computational design of tissue engineering scaffolds." Computer Methods in Applied Mechanics and Engineering **196**(31-32): 2991-2998.

Hollister, S. J. and W. L. Murphy (2011). "Scaffold Translation: Barriers Between Concept and Clinic." Tissue Engineering Part B-Reviews **17**(6): 459-474.

Holtorf, H. L., J. A. Jansen and A. G. Mikos (2005). "Flow perfusion culture induces the osteoblastic differentiation of marrow stromal cell-scaffold constructs in the absence of dexamethasone." Journal of Biomedical Materials Research Part A **72A**(3): 326-334.

Jianbo, C., E. Paetzell, Z. Jikou, L. Lyons and W. Soboyejo (2010). "Osteoblast-like cell ingrowth, adhesion and proliferation on porous Ti-6Al-4V with particulate and fiber scaffolds." Materials Science & Engineering: C (Materials for Biological Applications) **30**(5): 647-656656.

Jonitz, A., K. Lochner, T. Lindner, D. Hansmann, A. Marrot and R. Bader (2012). "Oxygen consumption, acidification and migration capacity of human primary osteoblasts within a three-dimensional tantalum scaffold." Journal of Materials Science-Materials in Medicine **22**(9): 2089-2095.

Jungreuthmayer, C., S. W. Donahue, M. J. Jaasma, A. A. Al-Munajjed, J. Zanghellini, D. J. Kelly and F. J. O'Brien (2009). "A Comparative Study of Shear Stresses in Collagen-Glycosaminoglycan and Calcium Phosphate Scaffolds in Bone Tissue-Engineering Bioreactors." Tissue Engineering Part A **15**(5): 1141-1149.

Kanichai, M., D. Ferguson, P. J. Prendergast and V. A. Campbell (2008). "Hypoxia promotes chondrogenesis in rat mesenchymal stem cells: A role for AKT and hypoxia-inducible factor (HIF)-1 alpha." Journal of Cellular Physiology **216**(3): 708-715.

Kavlock, K. D. and A. S. Goldstein (2011). "Effect of Pulse Frequency on the Osteogenic Differentiation of Mesenchymal Stem Cells in a Pulsatile Perfusion Bioreactor." Journal of Biomechanical Engineering-Transactions of the Asme **133**(9): 6.

Krogh, A. (1919). "The number and distirbution of cappilaries in muscles with calulations of the oxygen pressure head necessary for supplying the tissue." Journal of Physiology **52**: 409-415.

Langer, R. and J. P. Vacanti (1993). "TISSUE ENGINEERING." Science **260**(5110): 920-926.

Lennon, D. P., J. M. Edmison and A. I. Caplan (2001). "Cultivation of rat marrow-derived mesenchymal stem cells in reduced oxygen tension: effects on in vitro and in vivo osteochondrogenesis." J Cell Pysiol **187**(3): 345-355.

Li, D. Q., T. T. Tang, J. X. Lu and K. R. Dai (2009). "Effects of Flow Shear Stress and Mass Transport on the Construction of a Large-Scale Tissue-Engineered Bone in a Perfusion Bioreactor." Tissue Engineering Part A **15**(10): 2773-2783.

Li, J., E. Rose, D. Frances, Y. Sun and L. D. You (2012). "Effect of oscillating fluid flow stimulation on osteocyte mRNA expression." Journal of Biomechanics **45**(2): 247-251.

Liu, L. Y., B. Yu, J. R. Chen, Z. H. Tang, C. Zong, D. Shen, Q. Zheng, X. M. Tong, C. Y. Gao and J. F. Wang (2012). "Different effects of intermittent and continuous fluid shear stresses on osteogenic differentiation of human mesenchymal stem cells." Biomech Model Mechanobiol **11**(3-4): 391-401.

Malda, J., J. Rouwkema, D. E. Martens, E. P. le Comte, F. K. Kooy, J. Tramper, C. A. van Blitterswijk and J. Riesle (2004). "Oxygen gradients in tissue-engineered PEGT/PBT cartilaginous constructs: Measurement and modeling." Biotechnology and Bioengineering **86**(1): 9-18.

Malladi, P., Y. Xu, M. Chiou, A. J. Giaccia and M. T. Longaker (2006). "Effect of reduced oxygen tension on chondrogenesis and osteogenesis in adipose-derived mesenchymal cells." American Journal of Physiology-Cell Physiology **290**(4): C1139-C1145.

Martin, I., T. Smith and D. Wendt (2009). "Bioreactor-based roadmap for the translation of tissue engineering strategies into clinical products." Trends in Biotechnology **27**(9): 495-502.

Martin, I., D. Wendt and M. Heberer (2004). "The role of bioreactors in tissue engineering." Trends in Biotechnology **22**(2): 80-86.

McCoy, R. J. and F. J. O'Brien (2010). "Influence of Shear Stress in Perfusion Bioreactor Cultures for the Development of Three-Dimensional Bone Tissue Constructs: A Review." Tissue Engineering Part B-Reviews **16**(6): 587-601.

Meinel, L., V. Karageorgiou, R. Fajardo, B. Snyder, V. Shinde-Patil, L. Zichner, D. Kaplan, R. Langer and G. Vunjak-Novakovic (2004). "Bone tissue engineering using human mesenchymal stem cells: Effects of scaffold material and medium flow." Annals of Biomedical Engineering **32**(1): 112-122.

Melchels, F. P. W., A. M. C. Barradas, C. A. van Blitterswijk, J. de Boer, J. Feijen and D. W. Grijpma (2011). "Effects of the architecture of tissue engineering scaffolds on cell seeding and culturing." Acta Biomaterialia **6**(11): 4208-4217.

Mitsak, A. G., J. M. Kemppainen, M. T. Harris and S. J. Hollister (2011). "Effect of Polycaprolactone Scaffold Permeability on Bone Regeneration In Vivo." Tissue Engineering Part A **17**(13-14): 1831-1839.

O'Brien, F. J., B. A. Harley, I. V. Yannas and L. J. Gibson (2005). "The effect of pore size on cell adhesion in collagen-GAG scaffolds." Biomaterials **26**(4): 433-441.

Olivares, A. L., E. Marshal, J. A. Planell and D. Lacroix (2009). "Finite element study of scaffold architecture design and culture conditions for tissue engineering." Biomaterials **30**(30): 6142-6149.

Porter, B., R. Zauel, H. Stockman, R. Guldberg and D. Fyhrie (2005). "3-D computational modeling of media flow through scaffolds in a perfusion bioreactor." Journal of Biomechanics **38**(3): 543-549.

Qu, C. J., H. Lindeberg, J. H. Ylarinne and M. J. Lammi (2012). "Five percent oxygen tension is not beneficial for neocartilage formation in scaffold-free cell cultures." Cell and Tissue Research **348**(1): 109-117.

Raimondi, M. T., F. Boschetti, L. Falcone, G. B. Fiore, A. Remuzzi, E. Marinoni, M. Marazzi and R. Pietrabissa (2002). "Mechanobiology of engineered

cartilage cultured under a quantified fluid-dynamic environment." Biomech Model Mechanobiol **1**(1): 69-82.

Salter, E., B. Goh, B. Hung, D. Hutton, N. Ghone and W. L. Grayson (2012). "Bone Tissue Engineering Bioreactors: A Role in the Clinic?" Tissue Engineering Part B-Reviews **18**(1): 62-75.

Sheehy, E. J., C. T. Buckley and D. J. Kelly (2012). "Oxygen tension regulates the osteogenic, chondrogenic and-endochondral phenotype of bone marrow derived mesenchymal stem cells." Biochemical and Biophysical Research Communications **417**(1): 305-310.

Sikavitsas, V. I., G. N. Bancroft, H. L. Holtorf, J. A. Jansen and A. G. Mikos (2003). "Mineralized matrix deposition by marrow stromal osteoblasts in 3D perfusion culture increases with increasing fluid shear forces." Proceedings of the National Academy of Sciences of the United States of America **100**(25): 14683-14688.

Sikavitsas, V. I., G. N. Bancroft and A. G. Mikos (2002). "Formation of three-dimensional cell/polymer constructs for bone tissue engineering in a spinner flask and a rotating wall vessel bioreactor." Journal of Biomedical Materials Research **62**(1): 136-148.

Sikavitsas, V. I., J. S. Temenoff and A. G. Mikos (2001). "Biomaterials and bone mechanotransduction." Biomaterials **22**(19): 2581-2593.

Steinbrech, D. S., B. J. Mehrara, P. B. Saadeh, J. A. Greenwald, J. A. Spector, G. K. Gittes and M. T. Longaker (2000). "VEGF expression in an osteoblast-like cell line is regulated by a hypoxia response mechanism." American Journal of Physiology-Cell Physiology **278**(4): C853-C860.

Stiehler, M., C. Bunger, A. Baatrup, M. Lind, M. Kassem and T. Mygind (2009). "Effect of dynamic 3-D culture on proliferation, distribution, and osteogenic differentiation of human mesenchymal stem cells." Journal of Biomedical Materials Research Part A **89A**(1): 96-107.

Sucosky, P., D. F. Osorio, J. B. Brown and G. P. Neitzel (2004). "Fluid mechanics of a spinner-flask bioreactor." Biotechnology and Bioengineering **85**(1): 34-46.

Sutherland, R. M., B. Sordat, J. Bamat, H. Gabbert, B. Bourrat and W. Muellerklieser (1986). "OXYGENATION AND DIFFERENTIATION IN MULTICELLULAR SPHEROIDS OF HUMAN-COLON CARCINOMA." Cancer Research **46**(10): 5320-5329.

Truscello, S., J. Schrooten and H. Van Oosterwyck (2011). "A Computational Tool for the Upscaling of Regular Scaffolds During In Vitro Perfusion Culture." Tissue Engineering Part C-Methods **17**(6): 619-630.

Van Cleynenbreugel, T., J. Schrooten, H. Van Oosterwyck and J. V. Sloten (2006). "Micro-CT-based screening of biomechanical and structural properties of bone tissue engineering scaffolds." Medical & Biological Engineering & Computing **44**(7): 517-525.

Venkat, R. V., L. R. Stock and J. J. Chalmers (1996). "Study of hydrodynamics in microcarrier culture spinner vessels: A particle tracking velocimetry approach." Biotechnology and Bioengineering **49**(4): 456-466.

Volkmer, E., I. Drosse, S. Otto, A. Stangelmayer, M. Stengele, B. C. Kallukalam, W. Mutschler and M. Schieker (2008). "Hypoxia in static and dynamic 3D culture systems for tissue engineering of bone." Tissue Engineering Part A **14**(8): 1331-1340.

Wang, T. W., H. C. Wu, H. Y. Wang, F. H. Lin and J. S. Sun (2009). "Regulation of adult human mesenchymal stem cells into osteogenic and chondrogenic lineages by different bioreactor systems." Journal of Biomedical Materials Research Part A **88A**(4): 935-946.

Wang, Y., C. Wan, S. R. Gilbert and T. L. Clemens (2007). Oxygen sensing and osteogenesis. Skeletal Biology and Medicine, Pt B: Disease Mechanisms and Therapeutic Challenges. M. Zaidi. Oxford, Blackwell Publishing. **1117:** 1-11.

Wendt, D., M. Jakob and I. Martin (2005). "Bioreactor-based engineering of osteochondral grafts: from model systems to tissue manufacturing." Journal of Bioscience and Bioengineering **100**(5): 489-494.

Yeatts, A. B. and J. P. Fisher (2011). "Bone tissue engineering bioreactors: Dynamic culture and the influence of shear stress." Bone **48**(2): 171-181.

Yu, X. J., E. A. Botchwey, E. M. Levine, S. R. Pollack and C. T. Laurencin (2004). "Bioreactor-based bone tissue engineering: The influence of dynamic flow on osteoblast phenotypic expression and matrix mineralization." Proceedings of the National Academy of Sciences of the United States of America **101**(31): 11203-11208.

Yu, X. J., E. A. Botchwey, E. M. Levine, S. R. Pollack and C. T. Laurencin (2005). Bioreactor based bone tissue engineering: Influence of wall collision on osteoblast cultured on polymeric microcarrier scaffolds in rotating bioreactors. Nanoscale Materials Science in Biology and Medicine. C. T. Laurencin and E. A. Botchwey. Warrendale, Materials Research Society. **845:** 333-338.

Yuhang, C., M. Schellekens, Z. Shiwei, J. Cadman, L. Wei, R. Appleyard and L. Qing (2011). "Design Optimization of Scaffold Microstructures Using Wall Shear Stress Criterion Towards Regulated Flow-induced Erosion." Journal of Biomechanical Engineering **133**(8): 081008 (10 pp.)-081008 (10 pp.)081008 (10 pp.).

Zahm, A. M., M. A. Bucaro, P. S. Ayyaswamy, V. Srinivas, I. M. Shapiro, C. S. Adams and K. Mukundakrishnan (2010). "Numerical modeling of oxygen distributions in cortical and cancellous bone: oxygen availability governs osteonal and trabecular dimensions." American Journal of Physiology-Cell Physiology **299**(5): C922-C929.

Zahm, A. M., M. A. Bucaro, V. Srinivas, I. M. Shapiro and C. S. Adams (2008). "Oxygen tension regulates preosteocyte maturation and mineralization." Bone **43**(1): 25-31.

Chapter 3 MODELLING FLUID FLOW THROUGH IRREGULAR SCAFFOLDS FOR PERFUSION BIOREACTORS

This chapter presents a comparative computational fluid dynamics study between two irregular scaffolds created from different materials. The simulations are performed on cubic portion of the scaffold. Results are compared between both geometries and discussed in relation to current literature. Special attention is given to assess the influence of the size of the region from which the wall shear stress has been calculated in order to get insight in the effect of boundary conditions applied on the cubic model.

3. 1. INTRODUCTION

In general, bone engineering combines carrier materials (scaffolds), cell and signals to produce a tissue construct that once implanted in the defect site, will enhance bone regeneration. Although promising results have been obtained for the healing of large bone defects (Giannoni et al. 2008), much more research is needed before bone engineering can enter the daily clinical practice.

Attempts to culture *in vitro* tissue constructs in static conditions typically result in an outer shell of viable cells, while the inner core becomes necrotic because of a limited diffusive delivery of nutrients (Griffith et al. 2005). Various groups performed 3D *in vitro* perfusion experiments to improve mass transport and nutrient exchange. Results indeed show an increase in cell viability and matrix formation compared to static controls (Glowacki et al. 1998; Bancroft et al. 2002).

In addition, the culture media flow is known to influence osteogenesis through mechanical stimulation of the seeded bone precursor cells (McGarry et al. 2004). The effects of flow-mediated shear on cells have been studied in 2D monolayer cultures. Continuous fluid flow applied to osteoblasts *in vitro* has been shown to upregulate the expression of osteogenic markers (Klein-Nulend et al. 2005). Shear stresses in the range of 0.5-1.5 Pa affect osteoblast proliferation as well as production of nitric oxide (NO) and prostaglandin E2 (PGE_2), both instrumental in bone remodelling. Pulsatile and oscillatory flow conditions applied to osteoblasts using *in vitro* parallel-plate flow chambers have also shown increased gene expression, intracellular calcium concentration, and the production of NO and PGE_2 in comparison to static controls (Bakker et al. 2001). Furthermore, cell responsiveness has been reported to vary with fluid flow rate and the pulsation frequency in pulsatile flow (Mullender et al. 2004). Proposed mechanisms for the stimulation of cells by fluid flow include increased mass transport, generation of

streaming potentials and application of shear stress to the cell membranes (Bakker et al. 2001).

Although many of these studies were performed using 2D cell culture systems for short term experiments, they suggest that variable flow conditions may also have differential effects in 3D tissue culture systems.

However, calculating flow mediated shear stress within an irregular 3D porous scaffold is not trivial. Botchwey et al. (2003) tried to estimate shear stresses analytically by assuming a scaffold to be a uniform porous medium obeying Darcy's law. In combination with nutrient modelling, scaffolds are also usually treated as homogeneous porous media to reduce the computational cost (Coletti et al. 2006; Chung et al. 2007; Wilson et al. 2007). While this approach provides an averaged shear stress, the distribution of local shear stresses cannot be determined. Others have used Computer Aided Design (CAD) approaches where scaffolds are built as a repetitive pattern of unit cells (Boschetti et al. 2006; Singh et al. 2007). Although this method allows estimation of local shear stresses within the model, back-coupling to a realistic scaffold geometry might not be possible due to the simplifications in the CAD design, especially in case of irregular geometries. A more realistic geometric representation of a scaffold is obtained through micro-computed tomography (µCT). Using a Computational Fluid Dynamics (CFD) code it is possible to calculate local shear stresses and to compute distributions of shear stresses (Porter et al. 2005; Cioffi et al. 2006).

The goal of this study is first to compare the shear stress distribution within an irregular hydroxyapatite (HA) and a titanium (Ti) scaffold, and second to develop a methodology to create CFD models that allow to accurately estimate wall shear stress (WSS) and to assess the influence of model boundary conditions (BC's). The second goal will be evaluated using smaller sub models and by comparing different sizes of regions of interest in both the larger and the smaller model.

3. 2. MATERIALS AND METHODS

3. 2. 1. Geometry reconstruction.

In this study we used a HA and a Ti scaffold both produced through gelcasting. Porosities vary from 73% for HA to 77% for Ti, average pore sizes are 270 µm for HA and 280 for Ti. A µCT scanner (HOMX 161 X-ray system with AEA Tomohawk CT-upgrade, Philips X-ray, Hamburg, Germany) was used to obtain µCT images of both a titanium (Ti) and a hydroxyapatite (HA) scaffold with a voxel resolution of 8 µm. From hydrostatic weighing, a method of determining the density of a sample in which the sample is weighed in air, and then weighed in a liquid of

known density, the volume of the sample is calculated based on the loss of weight in the liquid divided by the density of the liquid (Archimedes method). The threshold grey value for 3D representation was assigned by comparing the material volume with the 3D volume calculated from the images through varying the threshold value in Tview (Skyscan, Kontich, Belgium). Since the model reconstruction software Mimics 11.2 (Materialise NV, Leuven, Belgium) uses compression algorithms for the grey scale we first converted the images to binary images using ImageJ (open source).

Table 3-1. Characteristics of the HOMX 161 X-ray system with AEA Tomohawk CT-upgrade

X-ray source voltage	15–160 kV
Maximum current	3.2 mA
Microfocal spot	From 5 to 200 μm
Minimum spatial resolution	10 μm (5 μm voxel size)
Detector	Detector CCD camera with a resolution of 1024_1024 pixels and a 12 bit dynamic range
Maximum sample dimensions	20 cm width and 20 cm height

3. 2. 2. CFD model creation

Calculating flow through a complete scaffold (diameter 5 mm, height 4 mm) with a resolution of 8 μm is far from evident in terms of computational costs. To tackle that problem one can either coarsen the geometry (Porter et al. 2005) or consider only a smaller portion of the complete scaffold (Cioffi et al. 2006). The disadvantage of coarsening the structure is the loss of fine struts within the geometry and the higher element size of the grid which will result in WSS underestimation. The disadvantage of using only a small portion lies in the fact that one cuts off channels of interconnected pores which leads to unrealistic BC's.

To estimate the WSS as accurately as possible a small portion of the complete scaffold is considered in the present study and the influence of the imposed BC's is taken into account.

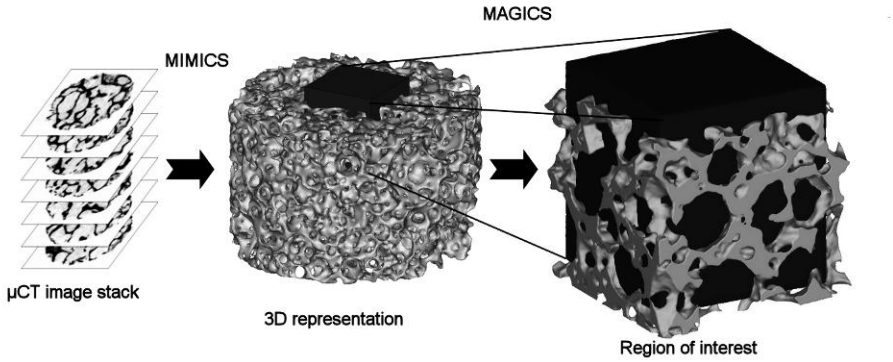

Figure 3-1. Procedure from µCT images to model selection shown for the HA scaffold. Fluid domain of interest is collared black; scaffold material is collared grey.

The fluid domain is obtained by subtracting the scaffold from a cube (with 1 mm or 1.5 mm edge length according to the model size) positioned at the physical inlet of the scaffold (Figure 3-1), using Magics (Materialise NV, Leuven, Belgium). The resulting fluid domain boundary surface is smoothed and the side walls are remeshed to obtain more isotropic elements (element length of 7 µm for the 1 mm models and 10 µm for the 1.5 mm models). Since fluid walls are of no interest for the WSS estimation the surface mesh is gradually coarsened on the fluid surfaces (blue zones in Figure 3-2) until a maximal edge length of 35 µm is acquired. Starting from this surface mesh we used TGrid 4.0 (ANSYS, Inc., Lebanon, USA) to create a volume mesh of 1,000,000 elements for the 1 mm models and 1,800,000 elements for the 1.5 mm models. An edge length based growth ratio of maximum 1.3 was used to gradually increase the 3D element size within the fluid volume in order to reduce the number of tetrahedral elements.

To avoid forcing a predefined mass flow through the channels at the inlet we added a flow guidance in front of the inlet with a height equal to 10% of the model width (Figure 3-2). This way the flow itself will preferentially choose the channels with the least resistance, thus better mimicking realistic inlet conditions.

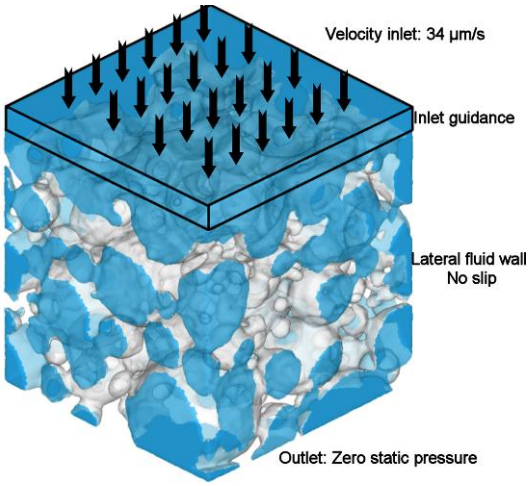

Figure 3-2: BC's adopted for the CFD calculations visualized on the 1.5 mm model of the HA scaffold. Velocity is based on 0.04 ml/min flow through a scaffold of 5 mm diameter. Flow direction is from top to bottom. Scaffold walls are coloured grey, fluid walls are coloured blue.

A flat velocity profile of 34 µm/s (corresponding to a flow rate of 0.04 ml/min through a circular area with a diameter of 5 mm) is imposed at the inlet. The lateral fluid walls are treated as closed walls with a no slip condition and the outlet is modelled as a constant static pressure outlet (Figure 3-2). The culture medium was modelled as an incompressible and homogeneous Newtonian fluid with ρ = 1000 kg/m³ and a measured dynamic viscosity of 8.51×10^{-4} Pa.s. Simulations are performed with Fluent 6.3 (ANSYS, Inc., Lebanon, USA).

3. 2. 3. Influence of the lateral boundary conditions

To estimate the error of the WSS introduced by closing the lateral walls of the fluid domain two concentric cubic models (1 mm edge length and 1.5 mm edge length) are compared in terms of WSS. In other words, the estimated WSS on a portion (called region of interest (ROI)) of the inner surface of the 1 mm model is compared with the WSS estimation from exactly the same surface but calculated in the 1.5 mm model (Figure 3-3). The ROI within the smaller model will have a higher influence of the BC compared to the same ROI within the larger model since the distance from the boundary has increased for the latter model.

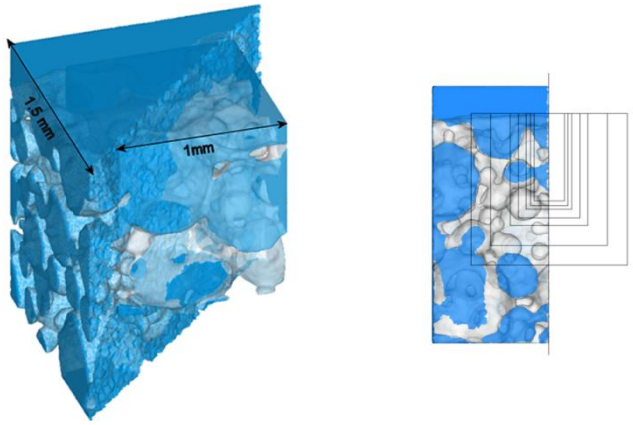

Figure 3-3: Left side: Visualization of two concentric models within a HA scaffold to evaluate the influence of the lateral BC's on the WSS. Right side: Visualization of the different regions of interest ROI's where the WSS is estimated from, showed on the HA scaffold (frontal view and only the left part is show of the HA 1.5 mm model). Different ROI's are concentrically placed in the scaffold model and extended upwards until the inlet region is incorporated in the ROI. The ROI's are named by the length of their shortest edge (200 µm, 250 µm, 300 µm, 400 µm, 500 µm, 750 µm and 1000 µm)

We defined different sizes of ROI (edge lengths of 1 mm (= the complete 1 mm model), 0.75 mm, 0.5 mm, 0.4 mm, 0.3 mm, 0.25 mm and 0.2 mm) in order to build a relationship between the distance towards the BC and the WSS values (Figure 3-3). To avoid unrealistically small surface areas where the WSS is derived from, we incorporated the inlet in the ROI since the inlet guidance makes it possible to create a BC comparable to the conditions in reality.

3. 3. RESULTS

All values and comparisons are derived from the 1.5 mm models as they are assumed to be more accurate. The influence of model size will be evaluated in the discussion section.

The internal steady flow pattern is visualized with streamlines, colour-coded according to the local velocity magnitude using Tecplot 360 (Tecplot, Inc. Bellevue, WA, USA). For both materials the same colour scale is used to enable comparison of the internal flow. Static pressure and WSS are visualized in combination with streamlines in order to link hydrodynamic parameters to each other.

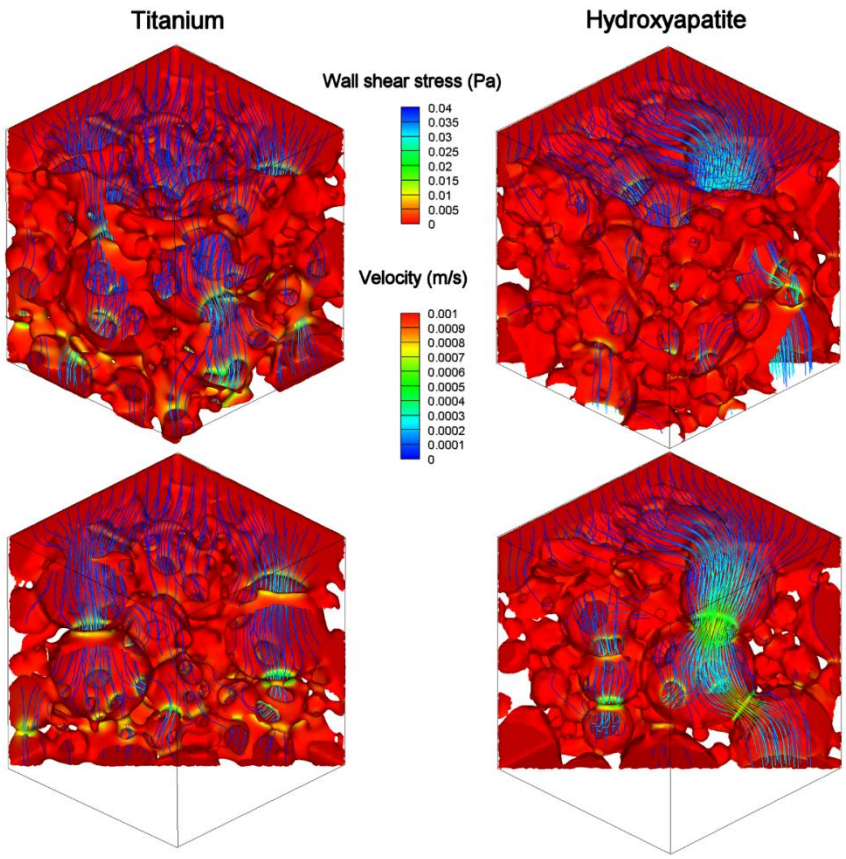

Figure 3-4. Local wall shear stress map (inverted colour scale) in combination with streamlines colour-coded according to velocity magnitude. Flow is from top to bottom. The plots on the left show the results for titanium while the plots on the right are for hydroxyapatite. In the upper plots the lateral fluid walls are removed to enable internal visualization. The lower plots show a diagonal cut-plot.

3. 3. 1. Titanium versus hydroxyapatite scaffold

The velocities cover a wide range of magnitudes and the streamlines show a highly tortuous behaviour as can be seen in the cross-sectional plots of Figure 3-4 and Figure 3-5. The maximal velocity in the HA scaffold (9 µm/s) is much higher than in the Ti scaffold (4 µm/s) although the same inlet conditions were applied for both scaffolds. This results in a higher maximal WSS for HA (0.046 Pa) compared to Ti (0.025 Pa). Considering surface averaged WSS we see an opposite behaviour showing the highest WSS value in the Ti scaffold (1.95 mPa compared to 1.46 mPa for HA). This can be explained by the strong preferential flow seen in the HA scaffold, for which media flow is mostly concentrated in a single path, whereas in the rest of the scaffold void there is virtually no flow. The high velocities obtained in the preferential flow path lead to higher WSS maxima. However, when averaged over the whole surface, the WSS in the HA scaffold declines because of the nearly zero medium flow in the other regions of the scaffold. The WSS for both geometries is below 1 mPa on more than 80% of the surface. Only at the inlet and outlet pores

of a bigger hole higher WSS values appear as a result of the locally higher velocities due to the filling or emptying of the hole. The strong preferential flow in the HA scaffold is also clearly seen on the top views (Figure 3-6), where the fluid tends to flow to the pore on the upper right corner of the image.

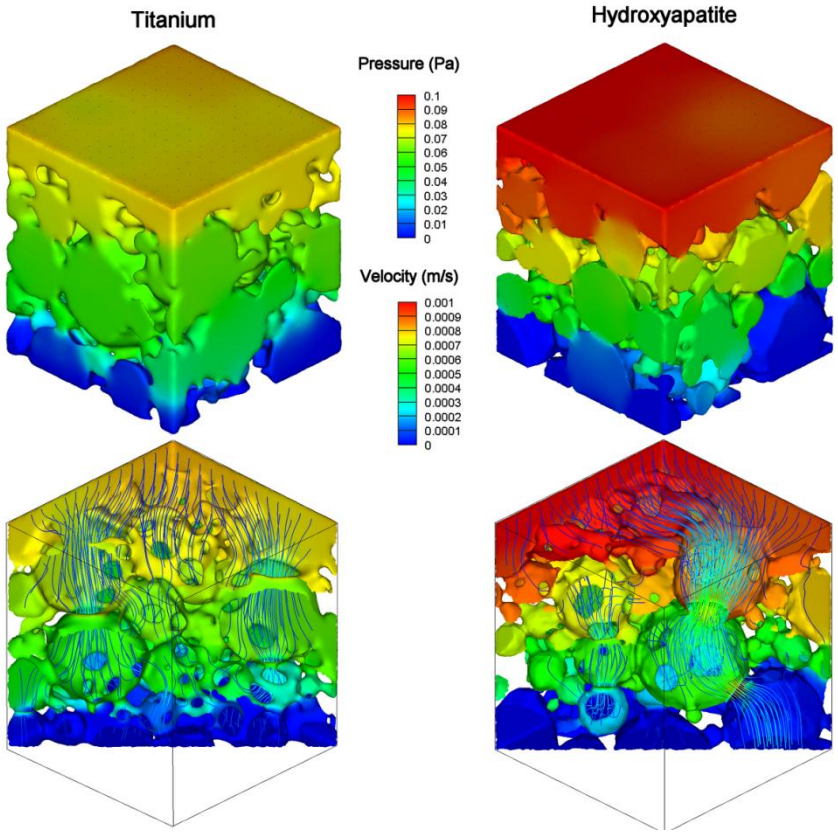

Figure 3-5. Visualization of the static pressure on the walls in combination with streamlines colour-coded according to velocity magnitude. Flow is from top to bottom. The plots on the left show the results for titanium while the plots on the right are for hydroxyapatite. The lower plots show a diagonal cut of the above geometry where also the wall of the inlet is removed to enhance visibility of the inner structure.

Considering the pressure on the scaffold walls a higher maximal value is noticed in the HA scaffold (0.11 Pa for HA versus 0.09 Pa for Ti). Since the same medium flow rate is applied to both materials this pressure difference is an indication of the resistance of the geometry. The higher resistance to fluid flow in the HA scaffold does not seem logical with regard to the high preferential flow. However, when taking a closer look to the geometrical structure one notices that, while nearly every pore is interconnected, the number of connections to other pores is much lower in the HA scaffold than in the Ti scaffold.

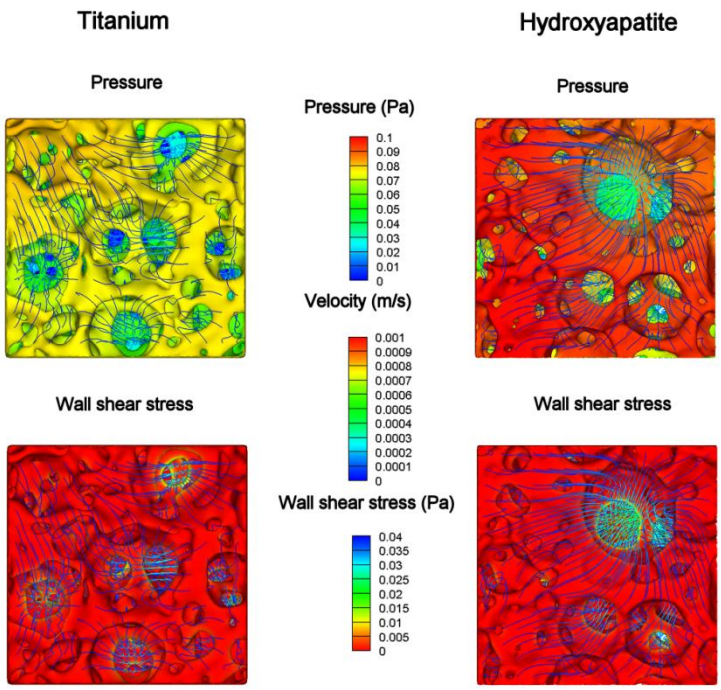

Figure 3-6. Visualization of the inlet region in the direction of the flow for Ti (left) and HA (right) scaffolds. The impact of the flow guidance in front of the inlet region can be appreciated, enabling the flow to follow the path with the least resistance. Upper plots show static pressure distribution, lower plots show wall shear stress (reverse colour scale). All plots are combined with streamlines colour-coded according to velocity.

3. 4. DISCUSSION

The aim of this study was to quantify the flow field through a titanium and a hydroxyapatite scaffold and to estimate the WSS imposed to the scaffold surface (and therefore to the cells attached to the surface) as accurately as possible. To evaluate the accuracy of the estimated WSS we worked with two models and five regions of interest for both scaffold materials

3. 4. 1. Impact of the model size

If we compare the 1 mm models with the 1.5 mm models we see some surprising differences within scaffolds of the same material.

As shown in Table 3-2 the difference in model size causes a non negligible difference in calculated WSS. However the difference in mesh size (7 µm edge length for the 1 mm model compared to 10 µm edge length for the 1.5 mm model) this cannot contribute to such discrepancies in WSS since mesh convergence results of the 1 mm model showed only 3% difference in WSS between 7 µm and 10 µm edge length of the mesh. A possible explanation is the scaffold heterogeneity which

is less covered in the 1 mm model. On the other hand, it is obvious that the 1 mm model experiences a larger influence of the proximity of the lateral BC.

3. 4. 2. Impact of the inlet guidance

Concerning the strong lateral flows showed in Figure 3-6 for the HA scaffold one might conclude that the inlet guidance is not suitably designed for mimicking realistic inlet conditions. However one should keep in mind that in reality the reorganization of flow particles before entering the scaffolds will also occur in a relatively thin region in front of the scaffold. Observing closely the streamlines colour-coded according to velocity in the inlet region of the HA scaffold one notices that velocities rise only when entering the pore. The strong lateral flow in the HA scaffold is not influencing the wall shear stress (Figure 3-6). Since the fluid in the inlet region has no lateral resistance and we are dealing with creep flow (Reynolds number of 0.06) the fluid freely reorganizes itself before entering the scaffold without affecting the WSS pattern on the inlet surface.

If one should be interested in studying the flow patterns in front of a scaffold a thin flow guidance might not be sufficient. Our study focuses on the WSS estimations on the inner walls of a scaffold so we designed a guidance with a small volume to suppress the calculation time.

3. 4. 3. Influence of the lateral boundary conditions

To investigate the influence of the lateral BC's we estimated WSS on a partial ROI of the 1 mm model and compared it with the WSS estimated from exactly the same surface but calculated within the 1.5 mm model. Doing so for different partial ROI sizes and plotting the surface averaged WSS results in the graph depicted in Figure 3-7. It clearly shows the variation in WSS within the scaffold and, as such, allows comparisons between different materials, model sizes and ROI sizes.
Caution is needed when interpreting Figure 3-7; when not considering the plots in Figures 4-6 one could easily conclude that the HA scaffold is much less irregular in behavior than the Ti scaffold. However we demonstrated the disturbance of a preferential flow in the HA scaffold occurring in most of the ROI's and by its abundance causing a smoothing of irregularities in WSS.

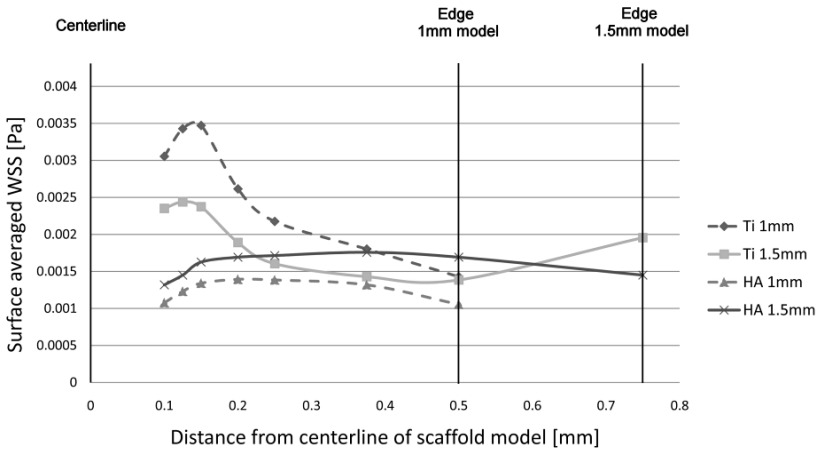

Figure 3-7. Graph depicting surface averaged WSS for titanium and hydroxyapatite scaffold calculated for both 1 mm and 1.5 mm models. The distance is expressed with regard to the centreline of the scaffold since every ROI is concentric with the scaffold model. Marks represent the surface averaged WSS estimated from an ROI with an edge length equal to twice the distance to the centreline.

Following the trend in WSS from the lateral walls of the cubic models towards the centreline it can be seen that there is a pronounced variation in surface averaged WSS from 0.25 mm to the centre (increasing for the Ti scaffold and decreasing for the HA scaffold). This variation in WSS suggests that the ROI has become irrelevantly small to derive accurate WSS from. In our case this occurs for a ROI smaller than 0.5 mm. Since this behaviour must be related to pore size (in our case approximately 275 µm for both scaffolds) we suggest a minimal ROI size for WSS estimation in irregular scaffolds equal to approximately twice the pore size. The relevance of this finding is obvious since taking a ROI of twice the pore size will always contain a scaffold surface whereas a smaller ROI might consist of only a scaffold pore.

The optimal size for ROI should be as large as possible without being affected by the imposed boundary conditions. In Figure 3-7 this can be found by looking at zones of constant WSS suggesting that the size of that ROI is representative for the irregular scaffold. For the Ti scaffold as well for the HA scaffold this is seen between 0.375 mm and 0.5 mm from the centreline. One notices that this is only the case for the 1.5 mm models of both scaffolds. The explanation lies in the fact that the distance of 0.5 mm from the centreline corresponds to the boundary of the 1 mm model so this WSS magnitude is lower due to the lower velocities in lateral cut off tubes in the proximity of the boundaries. Out of these results we are able to derive the minimal distance from the lateral boundaries being 0.25 mm or approximately one pore size. This seems relevant since the boundary effects are caused by cut off tubes with nearly no flow and these tubes will certainly no longer be the size of one pore.

Also important to notice is that, for the Ti scaffold, a deviation from the lowering trend of the WSS exists from 0.5 mm from the centreline toward the boundaries of the 1.5 mm model. This cannot be explained by boundary effects since the WSS tends to lower in proximity of boundaries. From this finding we must conclude that heterogeneity is not completely covered by a ROI with an edge length of 1 mm. This can also be seen in Figure 3-4; for Ti one notices the higher abundance of ring shaped zones with higher WSS at the bottom of the scaffold. These zones are not taken into account in the 1 mm model nor in the ROI with 1 mm edge length of the 1.5 mm model.

Another finding for the Ti scaffold is that the WSS values estimated from the 1 mm model are approximately 30 % higher than the ones estimated from the 1.5 mm model. This can be clarified by the effect of virtual narrowing of the fluid volume caused by closing pores on the lateral walls. In these virtually cut-off tubes there is nearly no flow. As a fixed mass flow was imposed based on the cross-sectional area of the inlet region, the fluid was forced to flow through a narrower cross-section, resulting in higher velocities. Since this effect is more pronounced in a smaller volume the velocities and WSS tend to be higher in the 1 mm model. Therefore one has to keep in mind that WSS estimations will always be overestimated in a model with artificially closed lateral boundaries. However the degree of overestimation will decrease with the number of pores modelled. On the other hand for the HA scaffold the trend in Figure 3-7 is quite the opposite, a finding that is mainly explicable by the disturbance of a preferential flow.

3. 4. 4. Comparison with literature

Results of µCT based models existing in literature are gathered in combination with results of our study in Table 3-2. Our results are in the same order of magnitude as the estimations found in literature. The result of Porter et al. (2005) is approximately half of ours. Boschetti et al. (2006) modelled WSS in scaffolds based on a CAD model of multiple unit cells. They concluded that the WSS magnitude is highly dependent on the pore size. This can be confirmed when comparing results from the Ti scaffold from our study to the model of Porter et al. (2005). Both models are calculated with approximately the same inlet velocity; a nearly doubling of the pore size (from 275 µm to 645 µm) results in halving the WSS (from 1.95 mPa to 1 mPa). The higher result of Cioffi et al. (2006) is due to the higher inlet velocity. Cioffi et al. (2006) found a linear relationship between WSS and imposed flow as a result of the very low Reynolds numbers causing the convective terms in the Navier-Stokes equations to be negligible. This allows us to compare the results of their model with the results of ours. Using a scaling factor of 0.642 to obtain our imposed inlet velocity of 34 µm/s would result in a WSS of 2.23 mPa for their model. This is

slightly higher than what we found but isn't enough to prove the hypothesis that WSS is dependent on pore size. A possible explanation lies in the fact that the scaffold material used by Cioffi et al. (2006) is a polyesterurethane foam while Porter et al. (2005) and a part of our simulations are based on µCT images of Ti scaffolds. This means that the actual micro-architecture plays a non-negligible role in predicting the overall WSS.

The fact that pore size is not the only variable influencing WSS magnitude can also be concluded from our simulations. A Ti and a HA scaffold lead to WSS differences up to 35 % although they have approximately the same porosity and pore size. This suggests an important influence of the structure geometry.
However, comparing values from other authors warrants caution since our simulations clearly show that there might be an important difference (up to 40%) in WSS due to a difference in modelled scaffold volume. This means that estimation of WSS imposed on seeded cells by culture media flow in irregular scaffolds is highly dependent on the methodology used.

Table 3-2. Results of µCT based modelling compared to present modelling results

Properties	**Present study**				**Cioffi et al. (2006)**	**Porter et al. (2005)**
Material	Titanium		Hydroxyapatite		Polyester-urethane	Titanium
	Ti 1 mm	Ti 1.5 mm	HA 1 mm	HA 1.5 mm		
Porosity	77 %		73 %		77 %	82 %
Pore size	280 µm		270 µm		100 µm	645 µm
Voxel size	8 µm				8 µm	68 µm
Modelled volume	1 mm³	3.375 mm³	1 mm³	3.375 mm³	0.064 mm³	85 mm³
# elements	1 000 000	1 800 000	1 000 000	1 800 000	600 000	500 000
Inlet velocity	34 µm/s				53 µm/s	36 µm/s
Average WSS	1.40 mPa	1.95 mPa	1.10mPa	1.46 mPa	3.48 mPa	1 mPa

3. 4. 5. Biological context

Cells subjected to perfusion undergo differentiation due to shear stresses imposed on the cell walls. Various experiments have been set up to measure the mechanosensitivity of stem cells. Most of these experiments are based on 2D flat plate experiments and as such not comparable with complex 3D flow through irregular support structures (Smith et al. 2004). Mullender et al. (2004) also suggested that imposing the same shear stresses might not be appropriate in 3D structures.

A combination of in vitro culture perfusion results and numerical WSS estimations in irregular scaffolds is listed in Table II. According to Cartmell et al. (2003) the estimated WSS of our models (ranging from 1.1 mPa to 1.95 mPa) would result in differentiation of the seeded cells, while Raimondi et al. (2006) suggested that it would have no effect. This discrepancy might be explained by the difference in WSS estimation methodology.

Table 3-3. Critical WSS values for seeded cells in a scaffold subjected to culture media perfusion

WSS [mPa]	**Effect**	**Author**
1.5-13.5	Stimulation	(Raimondi et al. 2002)
0.05	Proliferation	(Cartmell et al. 2003)
1	Differentiation	
57	Apoptosis	
4.6	No effect	(Raimondi et al. 2006)
14-25	Differentiation	
56	Cell wash out	

The scaffold geometries used for our simulations were also used in preliminary bioreactor experiments. Periosteum-derived precursor cells were seeded in the scaffolds and cell proliferation and differentiation (ALP expression) were quantified. In these first experiments cells seeded in the Ti scaffold showed proliferation and differentiation whereas in the HA scaffold this was not the case. This might be difficult to explain when only interpreting averaged WSS values.

Another important and sometimes limiting factor, besides the mechanoregulation of the culture media, is nutrient delivery to the seeded cells (Griffith et al. 2005). This shortness could explain for the different behaviour of the cells within the HA scaffold. The prominent preferential flow distinguishes the HA from the Ti scaffold (Figure 3-4, Figure 3-5). This difference in flow pattern leads to high WSS and flow in the neighbourhood of the preferential flow probably causing apoptosis or cell wash-out. On the other hand the cells in the remaining scaffold void might suffer

from the limited nutrient supply or might not be stimulated because of the WSS being too low.

3. 4. 6. Study limitations

One has to keep in mind that to date it is not possible to visualize cells inside a titanium or hydroxyapatite scaffold using μCT. This means that CFD simulations can only be performed on an empty scaffold.

It is easy to understand that WSS values will change when the scaffold is seeded and that cells will sense a different shear stress than modelled in an empty scaffold. Although this may seem an important limitation it is known that cells will adhere in the low shear stress regions and thus the difference in WSS might be negligible.
However, as cells tend to differentiate they will form an extracellular matrix (ECM). At the end of a successful incubation it happens that the support structure is filled with ECM leading to an important geometrical change of the scaffold void (Porter et al. 2007). This, however, is considered a minor limitation of our study since it is more important to achieve good starting conditions.

3. 5. CONCLUSIONS

We have transformed a micro-CT-based reconstruction of a highly irregular 3D geometry into a mesh suitable for computational fluid dynamics simulations. Using concentric models we were able to get insight in the sensitivity of wall shear stress to model size and proximity of boundary conditions. We were able to derive a minimal ROI size and a minimal distance from the lateral boundaries. Applying this modelling methodology on irregular titanium and hydroxyapatite scaffolds it was feasible to compare the scaffold materials and to evaluate the internal fluid-mechanical environment.

This methodology combined with *in vitro* experiments allows to get more insight in the complex concept of tissue engineering and will likely help to understand and eventually improve the fluid-mechanical aspects.

3. 6. REFERENCES

Bakker, A. D., K. Soejima, J. Klein-Nulend and E. H. Burger (2001). "The production of nitric oxide and prostaglandin E-2 by primary bone cells is shear stress dependent." Journal of Biomechanics **34**(5): 671-677.

Bancroft, G. N., V. I. Sikavitsas, J. van den Dolder, T. L. Sheffield, C. G. Ambrose, J. A. Jansen and A. G. Mikos (2002). "Fluid flow increases mineralized matrix deposition in 3D perfusion culture of marrow stromal osteloblasts in

a dose-dependent manner." Proceedings of the National Academy of Sciences of the United States of America **99**(20): 12600-12605.

Boschetti, F., M. T. Raimondi, F. Mighavacca and G. Dubini (2006). "Prediction of the micro-fluid dynamic environment imposed to three-dimensional engineered cell systems in bioreactors." Journal of Biomechanics **39**(3): 418-425.

Botchwey, E. A., S. R. Pollack, S. El-Amin, E. M. Levine, R. S. Tuan and C. T. Laurencin (2003). "Human osteoblast-like cells in three-dimensional culture with fluid flow." Biorheology **40**(1-3): 299-306.

Cartmell, S. H., B. D. Porter, A. J. Garcia and R. E. Guldberg (2003). "Effects of medium perfusion rate on cell-seeded three-dimensional bone constructs in vitro." Tissue Engineering **9**(6): 1197-1203.

Chung, C. A., C. W. Chen, C. P. Chen and C. S. Tseng (2007). "Enhancement of cell growth in tissue-engineering constructs under direct perfusion: Modeling and simulation." Biotechnology and Bioengineering **97**(6): 1603-1616.

Cioffi, M., F. Boschetti, M. T. Raimondi and G. Dubini (2006). "Modeling evaluation of the fluid-dynamic microenvironment in tissue-engineered constructs: A micro-CT based model." Biotechnology and Bioengineering **93**(3): 500-510.

Coletti, F., S. Macchietto and N. Elvassore (2006). "Mathematical modeling of three-dimensional cell cultures in perfusion bioreactors." Industrial & Engineering Chemistry Research **45**(24): 8158-8169.

Einhorn, T. A. (1999). "Clinically applied models of bone regeneration in tissue engineering research." Clinical Orthopaedics and Related Research(367): S59-S67.

Giannoni, P., M. Mastrogiacomo, M. Alini, S. G. Pearce, A. Corsi, F. Santolini, A. Muraglia, P. Bianco and R. Cancedda (2008). "Regeneration of large bone defects in sheep using bone marrow stromal cells." Journal of Tissue Engineering and Regenerative Medicine **2**(5): 253-262.

Glowacki, J., S. Mizuno and J. S. Greenberger (1998). "Perfusion enhances functions of bone marrow stromal cells in three-dimensional culture." Cell Transplantation **7**(3): 319-326.

Griffith, C. K., C. Miller, R. C. A. Sainson, J. W. Calvert, N. L. Jeon, C. C. W. Hughes and S. C. George (2005). "Diffusion limits of an in vitro thick prevascularized tissue." Tissue Engineering **11**(1-2): 257-266.

Klein-Nulend, J., R. G. Bacabac and M. G. Mullender (2005). "Mechanobiology of bone tissue." Pathologie Biologie **53**(10): 576-580.

McGarry, J. G., J. Klein-Nulend, M. G. Mullender and P. J. Prendergast (2004). "A comparison of strain and fluid shear stress in stimulating bone cell responses - a computational and experimental study." Faseb Journal **18**(15): 482-+.

Mullender, M., A. J. El Haj, Y. Yang, M. A. van Duin, E. H. Burger and J. Klein-Nulend (2004). "Mechanotransduction of bone cells in vitro: mechanobiology of bone tissue." Medical & Biological Engineering & Computing **42**(1): 14-21.

Porter, B., R. Zauel, H. Stockman, R. Guldberg and D. Fyhrie (2005). "3-D computational modeling of media flow through scaffolds in a perfusion bioreactor." Journal of Biomechanics **38**(3): 543-549.

Porter, B. D., A. S. Lin, A. Peister, D. Hutmacher and R. E. Guldberg (2007). "Noninvasive image analysis of 3D construct mineralization in a perfusion bioreactor." Biomaterials **28**(15): 2525-33.

Raimondi, M. T., F. Boschetti, L. Falcone, G. B. Fiore, A. Remuzzi, E. Marinoni, M. Marazzi and R. Pietrabissa (2002). "Mechanobiology of engineered cartilage cultured under a quantified fluid-dynamic environment." Biomech Model Mechanobiol **1**(1): 69-82.

Raimondi, M. T., M. Moretti, M. Cioffi, C. Giordano, F. Boschetti, K. Lagana and R. Pietrabissa (2006). "The effect of hydrodynamic shear on 3D engineered chondrocyte systems subject to direct perfusion." Biorheology **43**(3-4): 215-222.

Singh, H., E. S. Ang, T. T. Lim and D. W. Hutmacher (2007). "Flow modeling in a novel non-perfusion conical bioreactor." Biotechnology and Bioengineering **97**(5): 1291-1299.

Smith, R. L., D. R. Carter and D. J. Schurman (2004). "Pressure and shear differentially alter human articular chondrocyte metabolism - A review." Clinical Orthopaedics and Related Research(427): S89-S95.

Wilson, D. J., J. R. King and H. M. Byrne (2007). "Modelling scaffold occupation by a growing, nutrient-rich tissue." Mathematical Models & Methods in Applied Sciences **17**(1): 1721-1750.

Chapter 4 COMPUTATIONAL MODELS FOR WALL SHEAR STRESS ESTIMATION IN SCAFFOLDS: A COMPARATIVE STUDY OF TWO COMPLETE GEOMETRIES

Because of geometrical complexity of irregular scaffolds nearly all studies model only parts of the geometry assuming that the model covers the heterogeneity sufficiently. The investigation presented in this chapter focuses on providing guidelines in this matter. Aiming to avoid unrealistic boundary conditions we modeled two complete scaffold geometries. In order to get insight in required model size we subdivided the domain in regions of different size and compared the wall shear stress. Results from this chapter are discussed in relation with the findings in the previous chapter and used to propose suggestions for future model creation.

4. 1. INTRODUCTION

Bone tissue engineering is a promising technique to overcome the drawbacks of current bone replacing procedures like allografts and autografts. Autologous osteoprecursor cells are seeded upon a support structure (scaffold) and cultured in vitro, in order to form a bone construct. Significant hurdles after seeding are, among others, maintaining cell viability and forcing cells to differentiate towards an osteogenic lineage.

The first challenge occurs when trying to form viable constructs of clinically relevant sizes. Large (>1 cm^3) constructs often result in a necrotic central region with only a dense layer of cells at the construct's periphery. This is a typical result of a nutrient supply problem. When the consumption rate exceeds the diffusion of nutrients, active medium transport is required. This can be achieved using perfusion bioreactors, which improve mass transport and nutrient exchange during *in vitro* culture in macroporous scaffolds. Results indeed show an increase in cell viability and matrix formation compared to static controls (Glowacki et al. 1998; Bancroft et al. 2002).

Besides being important for mass transport, studies have shown that flow can have an effect on the osteogenic differentiation of precursor cells. Holtorf et al. (2005) compared the effect of a osteogenic differentiation stimulating to the effect of fluid induced mechanical stimuli caused by the perfusion itself. They found that perfusion induced stimuli had similar effect on differentiation.

Several *in vitro* studies demonstrated the positive effect of fluid shear stress on the differentiation of osteoprecursor cells (McGarry et al. 2004; Kreke et al. 2005;

Kreke et al. 2008; Scaglione et al. 2008). In these 2D laminar flow studies mass flow is altered to change wall shear stress. Results mostly show enhanced calcium and collagen production compared to static controls.

As shear stress appears to be an important player in bone tissue engineering it merits quantitative assessment. Direct measurements are impossible because of the complex channel distribution and small channel size. Computer simulation of wall shear stress inside scaffolds appears to be far from trivial, regarding the very limited literature concerning this issue. To date a number of fluid dynamic models have been created to describe fluid dynamic characteristics of irregular scaffolds (Cioffi et al. 2006; Cioffi et al. 2008; Jungreuthmayer et al. 2009). Nearly all of them are simulated on sub models (i.e. a portion of the entire scaffold) because of limitations in computer resources. Although all studies claim that the used model is sufficiently representative to capture the irregularities of the scaffolds, to the authors' knowledge no study exists providing guidelines in this matter. Our previous study indicated that the computed flow variables in these sub models are affected considerably by the lateral boundaries (Maes et al. 2009). The only way to overcome this potential drawback is modeling a complete geometry with a sufficiently high spatial resolution.

The aim of this study is therefore twofold: First, we will create CFD models of the complete irregular scaffold and compare major fluid dynamic variables (velocity, pressure, shear stress,..) with current literature primarily on sub models. Second, we will use different sizes of regions of interest within the complete scaffold to get more insight in the required model size for irregular scaffolds.

4. 2. MATERIALS AND METHODS

4. 2. 1. Geometry Reconstruction

In order to ensure ease of comparison we used the same scaffolds as in our previous work (Maes et al. 2009): A titanium (Ti) and a hydroxyapatite (HA) scaffold, both produced through gelcasting (for specifications of both scaffolds, see Table 4-1. specifications of the investigated scaffolds and scaffold models).
A µCT scanner (HOMX 161 X-ray system with AEA Tomohawk CT-upgrade, Philips X-ray, Hamburg, Germany) was used to acquire images of both scaffolds with a voxel resolution of 8 µm. The threshold gray value was determined by matching the material volume obtained from Archimedes measurements to that of the solid 3D volume calculated from the images in Tview (Skyscan, Kontich, Belgium).

Table 4-1. specifications of the investigated scaffolds and scaffold models

	Hydroxyapatite	**Titanium**
Diameter	5	5
Height	3.7	4.2
Porosity	73%	77%
Pore size	270 µm	280 µm

4. 2. 2. CFD model creation

Democells, an in-house developed meshing program based on the CGAL C++ library (*Computational Geometry Algorithms Library.* http://www.cgal.org.), was used to create triangular surface meshes from µ-CT images of the entire scaffold. The underlying algorithm guarantees that the triangles satisfy strict quality and size constraints and approximate the scaffold surface within a user-defined error bound (Boissonnat and Oudot 2005). The continuity conditions required by the algorithm were fulfilled by selecting an appropriate interpolation scheme for the µ-CT images and by lowering their resolution to match the level of detail desired from the mesh. As a resolution of 8 µm would be computationally too expensive we coarsened the input images resulting in a maximum triangle circumdiameter of 20 µm (HA) and 24 µm (Ti). Mimics 13 (Materialise NV, Leuven, Belgium) was used to remove boundary artifacts that caused volume mesh problems.

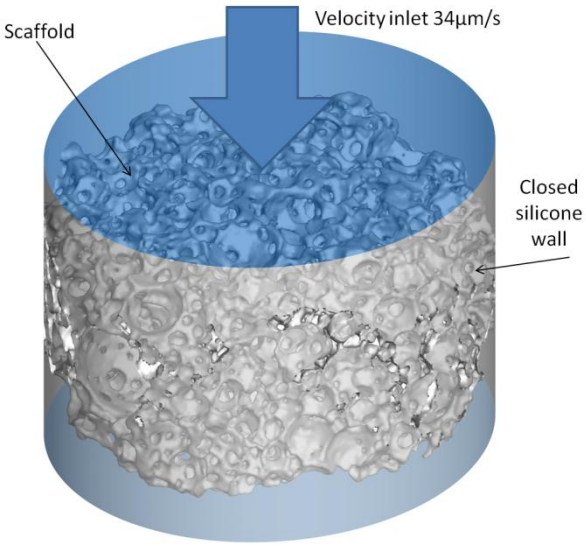

Figure 4-1. BC's adopted for the CFD calculations visualized on the HA scaffold. Velocity is based on 0.04 ml/min flow through a scaffold of 5 mm diameter. Flow direction is from top to bottom. Scaffold walls are coloured light grey. Vertical cylindrical wall represents the silicone embedded around the scaffold. Openings in the wall occur when the scaffold makes contact with the silicone.

The resulting geometry represents the void phase of the scaffold. To avoid forcing a predefined mass flow through the channels at the inlet we added a flow guidance in front of the inlet with a height of 0.5 mm. This way we anticipate that the flow itself will choose the channels with the least resistance and thus better mimic realistic inlet conditions. To avoid the need to work with multiple outlets we also constructed an outlet flow guidance of 0.5 mm (Figure 4-1).

Similarly to our previous study we created concentric cubic zones within the scaffold model. These regions of interest (ROIs) will be used to analyze the variance of wall shear stress inside the scaffold. ROIs have edge lengths varying from 0.5 mm to 2 mm and 3.25 for HA en Ti, respectively, with a step of 0.25 mm (Figure 4-2).

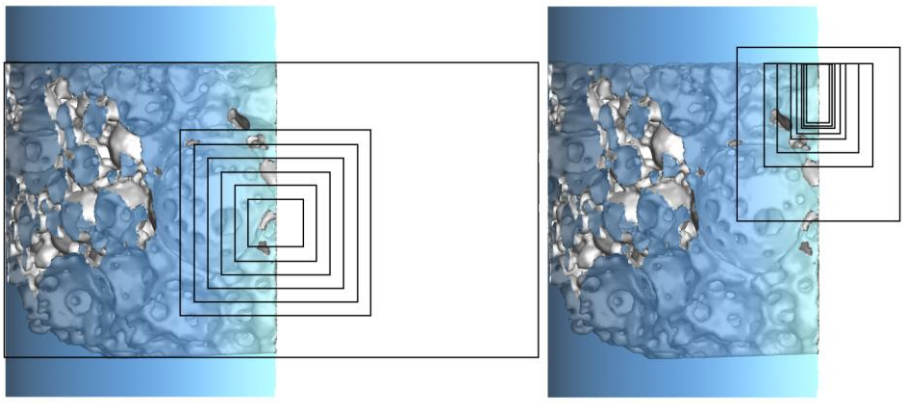

Figure 4-2: Visualization of the Regions of Interest (ROI) from which wall shear stress are calculated in the hydroxyapatite scaffold (analogous for titanium). Left: present study; outer lines are the boundaries of the scaffold, inner lines are the different ROIs (from inside to outside ROI edge lengths of 0.5mm; 0.75mm; 1mm; 1.25mm; 1.5mm; 1.75mm; 2mm and complete scaffold of 5mm). Right: previous study; outer lines are the 1.5 mm model boundaries, inner lines are the ROIs from the previous study (from inside to outside edge lengths of 0.2mm; 0.25mm; 0.3mm; 0.4mm; 0.5mm; 0.75mm; 1mm; 1.5mm) (Maes et al. 2009). The dots shown in the graph of figure 5 represent surface averaged wall shear stress values from the depicted ROIs.

Starting from this surface mesh we used TGrid 5.0 (ANSYS, Inc., Lebanon, USA) to create a volume mesh of $25 \cdot 10^6$ elements for the HA scaffold and $23 \cdot 10^6$ elements for the Ti scaffold. A maximum growth ratio of 1.3 for neighboring cells was set to gradually increase the 3D element size within the fluid volume in order to reduce the number of tetrahedral elements.

A uniform velocity profile of 34 µm/s (corresponding to a flow rate of 0.04 ml/min) through a circular area with a diameter of 5 mm is imposed at the inlet. The lateral

walls of the scaffolds are modeled as being embedded in a silicon tube. As scaffolds were not perfectly circular we used Democells to model an elliptical cylinder, with a small transverse/conjugate diameter ratio (1.1 for HA and 1.03 for Ti), wrapped as tight as possible around the scaffold. To avoid side flow between the cylindrical wall and the scaffold, some extremities of the scaffold were cut off enabling a closer wrapping of the cylinder (Figure 4-1 and Figure 4-3 3D views)).

The culture medium was modeled as an incompressible and homogeneous Newtonian fluid (density ρ = 1000 kg/m³ and dynamic viscosity $8.51 \cdot 10^{-4}$ Pa.s at 37°C). Simulations are performed with Fluent 6.3 (ANSYS, Inc., Lebanon, USA) on a cluster with 8 AMD Athlon dual core 2.4 GHz CPUs with 64 GB RAM. Pre and post processing are done on a workstation with two quad core Intel Xeon 2.53 GHz CPUs with 24 GB RAM.

4. 3. RESULTS

In Figure 4-3A-D the internal steady flow pattern is visualized with streamlines, color-coded according to the velocity magnitude using Tecplot 360 (Tecplot, Inc. Bellevue, WA, USA). The velocity data are combined with other hydrodynamic parameters such as WSS (panels A-C in Figure 4-3) and static pressure (panel D). For both scaffolds the WSS is inverse color coded to enhance visualization.

4. 3. 1. Titanium (Ti) versus hydroxyapatite (HA) scaffold

As shown in Figure 4-3, the streamlines show a highly tortuous behavior. Given the extremely slow flow rate (Reynolds number based on average porosity and average velocity is in the order of 10^{-3}), this behavior is entirely due to the highly irregular geometry. The maximum fluid velocity as well as the WSS are of the same order of magnitude in both scaffolds with values of 1.1 mm/s and 0.025 Pa resp. in HA and 0.9 mm/s and 0.026 Pa for Ti. In contrast, a considerable difference in surface averaged WSS was noted between HA (0.00109 Pa) and Ti (0.00141 Pa). These values are much lower than their maximal values which is due to highly skewed WSS distributions as shown in Figure 4-4.

The top views of both scaffolds (Figure 4-3B) display the inlet regions of both scaffolds indicating zones with highly preferential flow paths for both scaffolds. These zones are associated with low pressure (low resistance) and occur primarily at the entrance of subsequent large pores that make a strong interconnection between top and bottom (Figure 4-3D). On the other hand, zones with no apparent preferential flow display much less, almost zero, flow and are associated with higher pressure (signifying higher resistance). Qualitatively one could say that preferential flow paths occur more prominently at the inlet of the HA scaffold.

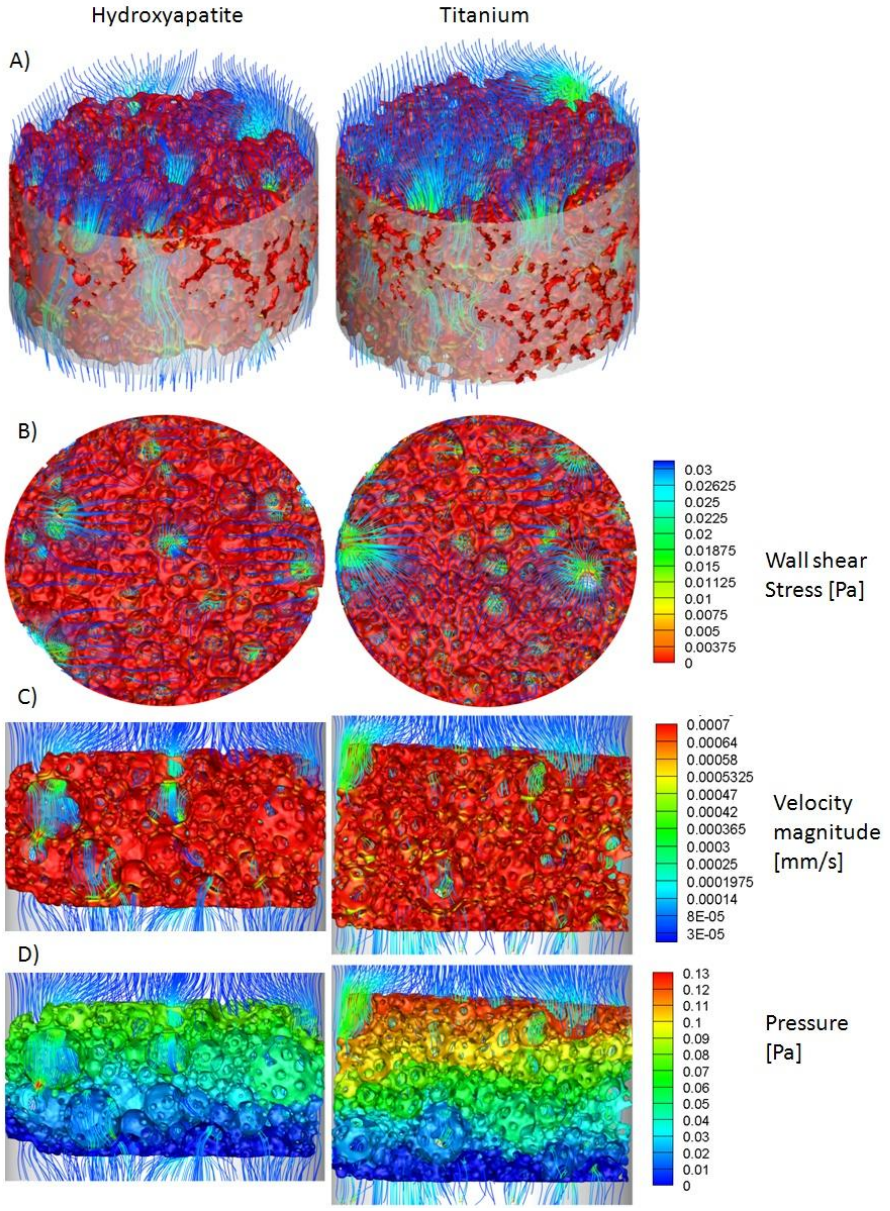

Figure 4-3. Visualization of the wall shear stress (WSS, inverse colour coding is used to enhance visualization) and the static pressure (P) on the walls, all panels are in combination with streamlines colour-coded according to velocity magnitude. Flow is from top to bottom. The plots on the left show the results for titanium while the plots on the right are for hydroxyapatite. From top to bottom: A: 3D impression showing WSS, B: top view of the inlet (WSS), C: transversal plot showing the internal structure in the middle of the geometry (WSS), D: same plot but showing the pressure.

Also, an important difference in maximum pressure (at the fluid wall interface) was observed (0.13 Pa for Ti and versus 0.09 Pa for the HA). Since the same media flow rate is applied to both geometries this difference in pressure difference between the inlet and outlet is indicative of the difference in permeability. The higher prevalence of preferential flows in HA is likely the result of its higher permeability.

4. 4. DISCUSSION

4. 4. 1. Scaffold fluid dynamics versus scaffold geometry

The first aim of this study was to quantify the flow field through a titanium (Ti) and a Hydroxyapatite (HA) scaffold and to estimate the WSS exerted on the seeded cells. Results are in line with literature (Table 4-2). Depending on the value of WSS the proliferation and osteogenic differentiation of cells subjected to perfusion may be enhanced. Results of in vitro culture perfusion experiments performed in literature in relation to numerical WSS estimations in irregular scaffolds are listed in Table 4-2. According to Cartmell et al. (2003) our estimated WSS range would enhance differentiation of the seeded cells, also Raimondi et al. (2006) suggested stimulation of the seeded cells for our WSS region. Obviously, this needs to be confirmed by means of experiments with the scaffolds under investigation.

Table 4-2. Critical WSS values for seeded cells in a scaffold subjected to culture media perfusion

WSS [mPa]	**Effect**	**Author**
1.5-13.5	Stimulation	(Raimondi et al. 2002)
0.05	Proliferation	(Cartmell et al. 2003)
1	Differentiation	
57	Apoptosis	
4.6	Stimulation	(Raimondi et al. 2006)
14-25	Differentiation	
56	Cell wash out	

Besides WSS local flow rate might influence local cell viability. This can easily be seen in particular in the HA scaffold. The large preferential flow paths could compromise cell growth since a large amount of the culture medium is flowing through a comparably small part of the scaffold void. This causes less nutrients and oxygen to be available for the cells outside this region. The non-uniform flow distributions is also reflected in the highly skewed WSS histograms in Figure 4-4.

There one notices that the WSS distribution of the HA scaffold is even more skewed than that of the Ti scaffold, resulting in a larger surface area with almost zero shear stress in the HA scaffold. Apparently there are more zones in the HA scaffold with virtually no flow at all, resulting in less optimal cell culture conditions.

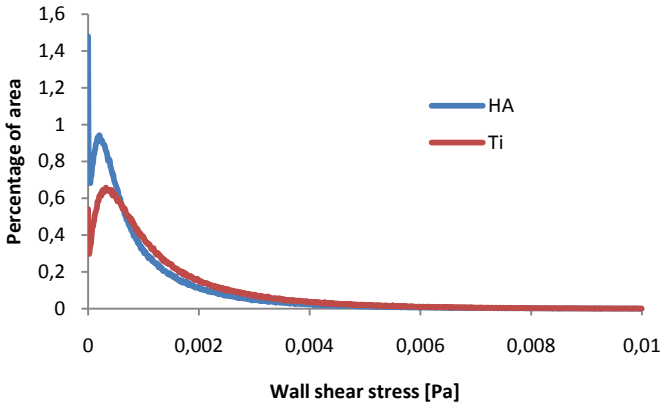

Figure 4-4: Histogram of WSS in hydroxyapatite (blue) and titanium (red). 1000 divisions are calculated and only the top line of the histogram is shown. The plot is truncated at 0.01Pa.

We anticipate that the above mentioned findings are due to geometrical differences. From the flow simulation results it seems that although both scaffolds have similar pore size and porosity, the number of connections between pores in the HA scaffolds is lower or less evenly distributed than in the Ti scaffold. It might be that the difference in material properties is causing the difference in connectivity. Both scaffolds are created through gel casting, but, because of different material diffusivity of Ti versus HA, different parameters were set to obtain similar pore size and porosity.

4. 4. 2. Guidelines for CFD model construction

Given that experimental determination of WSS in scaffolds is impossible all reported WSS results are based on simulations (Table 4-3). Table 4-3 shows that all reported WSS values estimated with analogous inlet conditions are in the same order of magnitude as our results. Importantly, however, all but one of the reported simulation studies are performed on a small sub model of the actual geometry due to high computational costs.

Of particular interest is the comparison between the present results and the results computed in two smaller models (1% and 4% of the complete volume) which show important differences (Table 4-3). Before trying to explain one has to keep in mind that a mesh with an element size of 20 µm underestimated surface averaged wall

shear stress with almost 15% compared to a mesh with an element size of 8 µm (between 20 µm and 24 µm the difference was of the order of 1%). The values reported in tables and graphs are the results of individual simulations, no corrections are applied.

We hypothesize that these differences are caused by 2 factors: (i) heterogeneity and (ii) unrealistic boundary conditions.

To describe heterogeneity we calculated averaged WSS in sub regions in the complete CFD models. Since the scaffolds used in the current and the previous study are identical we combined the results of both studies in Figure 5. In this figure each point on the line of a given model represents the surface averaged WSS of a ROI inside that model (for visualization of the ROIs of both studies we refer to (Figure 4-2). Despite differences in location and shape of the ROIs the graph in (Figure 4-5) shows for Ti a remarkably good agreement between the ROIs in the 1.5 mm model and the ROIs in the complete model except when WSS is calculated for the entire 1.5 mm model (largest ROI). The ideal model size for this Ti scaffold should therefore be a cube of 1.5 mm edge length (5.5 times the pore size). For WSS variation in HA the 1 mm model shows good agreement with the entire scaffold model. However this model size is obviously not representative since the larger 1.5 mm model shows a strong deviation for WSS variation compared to the complete scaffold. The HA model probably needs to be larger than 1.5 mm to account for the heterogeneity that induces the large preferential flow covering a prominent part of the smaller sub models. We propose a model size of 8-10 times the average pore size.

Table 4-3. Comparative table of available µCT based CFD models according to Voronov et al. (Voronov et al. 2010). To facilitate comparison of the estimated value for wall shear stress, details of the models are provided. Additionally model dimensions are expressed in number of pores to evaluate the model size. For models only taken from a sub part of the geometry where the wall shear stress is estimated on a small sub region, the distance from the sub region to the boundary of the CFD model is also expressed in number of pores. D=Diameter, H= height and L = Length

reference	Scaffold type	Pore size µm	Model size mm (**number of pores**)	Distance from the boundary mm (number of pores)	Number of elements	Element length µm	Inlet velocity µm/s	Average Wall shear stress mPa
Cioffi et al. (2006)	Degrapol	100	3 Cubes 0.4 (**4**)	0.15 (**1.5**)	600 000	0.8	53	3.28 3.75 3.94
Sandino et al. (2008)	Calcium phosphate	300-400	Cilinder D=1 (**2.85**) H=2 (**5.7**)	/	636 183		10	37 (max)
	glass				174 710			46 (max)
Cioffi et al. (2008)	Polyethylene glycol tetraphtalate	100	Cube L=0.4 (**4**)	/	315 000		11.45 And 114.5	2.56 And 25.6
Jungreuther-mayer et	Collagen-glycosamino-	96	Cube		1 700 000	4.7	235	200

al.(2009)	glycan		0.64x0.64x0.48 (**6.6x6.6x5**)	0.08-0.16 (**0.83-1.66**)				
	Calcium-phosphate	350	Cilinder D= 5 (**14**) H= 3.9 (**11**)	Entire scaffold	8 000 000	23.8	53800	7500
Maes et al. (2009)	Titanium	270	Cube L=1 (**3.7**) L=1.5 (**5.5**)	/ 0.25 (**0.95**)	1 000 000 1 800 000	8 10	34	1.4 1.95
	Hydroxyapatite	280	Cube L=1 (**3.6**) L=1.5 (**5.4**)	/ 0.25 (**0.89**)	1 000 000 1 800 000	8 10		1.1 1.46
Present study	Titanium	270	Cilinder D= 5 (**18**) H= 4.2 (**15**)	Entire scaffold	23 000 000	24	34	1.41
	Hydroxyapatite	280	Cilinder D= 5 (**18**) H= 3.7 (**13**)	Entire scaffold	25 000 000	20		1.09

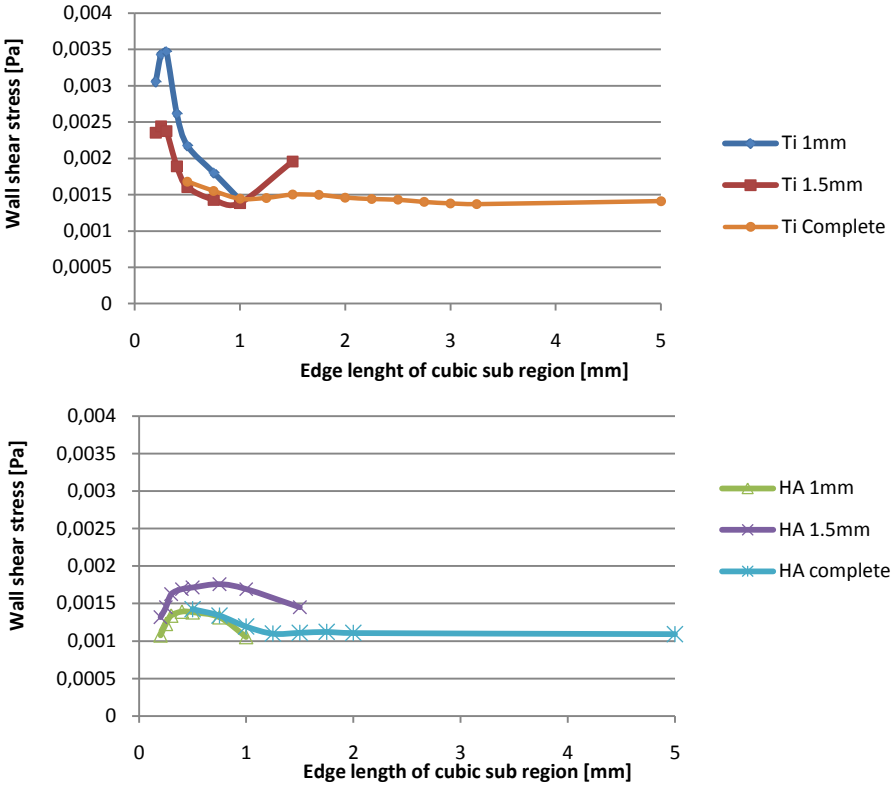

Figure 4-5: surface area averaged wall shear stress for a number of regions of interest calculated in 3 CFD models created for both Ti (left) and Ha (right). "Ti 1mm" and "Ti 1.5 mm" are cubic models from our previous study (Maes et al. 2009). "Ti complete" and "HA complete" refer to the complete scaffolds simulated in the present study. Horizontal axis depicts the size of the region of interest (ROI) expressed as edge length of the cubic ROI. Points on the line of one of the models represent the surface averaged wall shear stress for a cubic ROI with given edge length inside that model; Last point of every line shows the WSS of the complete CFD model. For locations of the ROIs in every model we refer to Figure 2.

The influence of unrealistic boundary is caused by the lateral walls of the sub model closing off channels where in reality media flow is passing trough. Logically this influence would not reach further than the size of closed pore. This influence is also visible in the graph in Figure 4-5. Both the Ti and HA 1.5 mm models show a deviation at the last point of the line. We suggest therefore that the WSS is modeled in sub region which is one pore size away from the model boundaries.

Comparison with model size used in literature. Applying the guidelines of model creation to other WSS estimation studies of irregular scaffolds reported in literature could help to compare results. For that reason every distance in Table 4-3 is also expressed in terms of pore sizes. Assuming none of the scaffolds reported in Table 4-3 suffers from strong heterogeneities we suggest five to six times the pore size as a lower bound for the model size. From Table 4-3 we could notice that only the

models of Jungreuthermayer et al. (2009) are sufficiently large to cover heterogeneity. The other studies worked with models that appear too small. The work of Cioffi et al. (2006) gives an idea of possible wall shear stress variance in the a scaffold geometry between CFD models of insufficient size. The variance between their three models is in the order of 20%.

Except for the models of Sandino et al. (2008) all wall shear stress values are estimated on a sub model of the scaffold. Taking a minimal distance from the boundaries of the CFD model of approximately one pore size, all reported sub portions were chosen at a sufficient distance.

From this we can conclude that caution is required when comparing values reported in literature, especially if the CFD models did not account for boundary artifacts or if the models are too small to cover heterogeneity.

4. 5. CONCLUSIONS

To avoid any impact of unrealistic boundary conditions in CFD models based on a sub portion of the entire scaffold, we created CFD models of two complete scaffold geometries. Computed WSS values were in line with literature data. Our approach enabled to assess the influence of model size and model boundaries. We propose the following guidelines determining the dimensions of sub models of scaffolds. For scaffolds with a rather homogenous pore distribution (no expectance of high preferential flows) model size should be at least six times the average pore size. Other scaffolds should be modeled with at least a model size of eight to ten times the average pore size. To avoid unwanted influence of boundaries we propose estimating wall shear stress in a sub region of the model. This sub region should be at least one pore size away from the lateral walls. We reflected these guidelines to values gathered from literature and demonstrated that comparison is possible but needs to be done with precaution. The guidelines presented in this work could be of help for further detailed modeling of for example oxygen and nutrient uptake and cellular proliferation in irregular scaffolds for bone tissue engineering.

4. 6. REFERENCES

Bancroft, G. N., V. I. Sikavitsas, J. van den Dolder, T. L. Sheffield, C. G. Ambrose, J. A. Jansen and A. G. Mikos (2002). "Fluid flow increases mineralized matrix deposition in 3D perfusion culture of marrow stromal osteloblasts in a dose-dependent manner." Proceedings of the National Academy of Sciences of the United States of America **99**(20): 12600-12605.

Boissonnat, J. D. and S. Oudot (2005). "Provably good sampling and meshing of surfaces." Graphical Models **67**(5): 405-451.

Cartmell, S. H., B. D. Porter, A. J. Garcia and R. E. Guldberg (2003). "Effects of medium perfusion rate on cell-seeded three-dimensional bone constructs in vitro." Tissue Engineering **9**(6): 1197-1203.

Cioffi, M., F. Boschetti, M. T. Raimondi and G. Dubini (2006). "Modeling evaluation of the fluid-dynamic microenvironment in tissue-engineered constructs: A micro-CT based model." Biotechnology and Bioengineering **93**(3): 500-510.

Cioffi, M., J. Kuffer, S. Strobel, G. Dubini, I. Martin and D. Wendt (2008). "Computational evaluation of oxygen and shear stress distributions in 3D perfusion culture systems: Macro-scale and micro-structured models." Journal of Biomechanics **41**(14): 2918-2925.

Glowacki, J., S. Mizuno and J. S. Greenberger (1998). "Perfusion enhances functions of bone marrow stromal cells in three-dimensional culture." Cell Transplantation **7**(3): 319-326.

Holtorf, H. L., J. A. Jansen and A. G. Mikos (2005). "Flow perfusion culture induces the osteoblastic differentiation of marrow stromal cell-scaffold constructs in the absence of dexamethasone." Journal of Biomedical Materials Research Part A **72A**(3): 326-334.

Jungreuthmayer, C., S. W. Donahue, M. J. Jaasma, A. A. Al-Munajjed, J. Zanghellini, D. J. Kelly and F. J. O'Brien (2009). "A Comparative Study of Shear Stresses in Collagen-Glycosaminoglycan and Calcium Phosphate Scaffolds in Bone Tissue-Engineering Bioreactors." Tissue Engineering Part A **15**(5): 1141-1149.

Kreke, M. R., W. R. Huckle and A. S. Goldstein (2005). "Fluid flow stimulates expression of osteopontin and bone sialoprotein by bone marrow stromal cells in a temporally dependent manner." Bone **36**(6): 1047-1055.

Kreke, M. R., L. A. Sharp, Y. W. Lee and A. S. Goldstein (2008). "Effect of intermittent shear stress on mechanotransductive signaling and osteoblastic differentiation of bone marrow stromal cells." Tissue Engineering Part A **14**(4): 529-537.

Maes, F., P. Van Ransbeeck, H. Van Oosterwyck and P. Verdonck (2009). "Modeling fluid flow through irregular scaffolds for perfusion bioreactors." Biotechnol Bioeng **103**(3): 621-30.

McGarry, J. G., J. Klein-Nulend, M. G. Mullender and P. J. Prendergast (2004). "A comparison of strain and fluid shear stress in stimulating bone cell responses - a computational and experimental study." Faseb Journal **18**(15): 482-+.

Raimondi, M. T., F. Boschetti, G. B. Fiore, G. Dubini, L. Falcone, A. Remuzzi, E. Marinoni, M. Marazzi and R. Pietrabissa (2002). Integration of computational and experimental methods in the study of cartilage mechanobiology.

Raimondi, M. T., M. Moretti, M. Cioffi, C. Giordano, F. Boschetti, K. Lagana and R. Pietrabissa (2006). "The effect of hydrodynamic shear on 3D engineered chondrocyte systems subject to direct perfusion." Biorheology **43**(3-4): 215-222.

Sandino, C., J. A. Planell and D. Lacroix (2008). "A finite element study of mechanical stimuli in scaffolds for bone tissue engineering." Journal of Biomechanics **41**(5): 1005-1014.

Scaglione, S., D. Wendt, S. Miggino, A. Papadimitropoulos, M. Fato, R. Quarto and I. Martin (2008). "Effects of fluid flow and calcium phosphate coating on

human bone marrow stromal cells cultured in a defined 2D model system." Journal of Biomedical Materials Research Part A **86A**(2): 411-419.

Voronov, R., S. VanGordon, V. I. Sikavitsas and D. V. Papavassiliou (2010). "Computational modeling of flow-induced shear stresses within 3D salt-leached porous scaffolds imaged via micro-CT." Journal of Biomechanics **43**(7): 1279-1286.

Chapter 5 OXYGEN DISTRIBUTION IN IRREGULAR SCAFFOLDS: IN SILICO AND IN VITRO STUDY

This chapter compares results from oxygen tension simulations with results of in vitro studies. After a brief introduction we explain the methodologies applied and post the goals of the investigation. Special attention is given to explaining the different behaviour of a titanium scaffold and a hydroxyapatite scaffold.

5. 1. INTRODUCTION

Bone tissue engineering might present an alternative for current autologous bone grafting in treating large bone defects. Yet up till now scaffold based bone tissue engineering of clinically relevant sized constructs failed (Hollister and Murphy 2011). Several studies report inhomogeneous cellular proliferation and differentiation (Malda et al. 2004; Lewis et al. 2005; Malladi et al. 2006). They all showed that these tissue heterogeneities are most likely a reflection of local oxygen tension gradients. The main reason is that oxygen is known to have a poor diffusion capacity in aqueous conditions. Therefore *in vitro* maximal distances for oxygen transport due to diffusion are reported to be limited to 100-200µm (Muschler et al. 2004). This means that the bigger the scaffold the more difficult it will be to guarantee an homogeneous distribution of oxygen and nutrients in static conditions. However, maintaining a stable oxygenation is a prerequisite for creating a viable tissue that can be used for clinical applications (Martin et al. 2009). Several types of bioreactor systems have been developed with the aim of improving culture conditions (Martin et al. 2004; Yeatts and Fisher 2011). Comparative experiments have pointed out that perfusion bioreactors are among the most promising (Goldstein et al. 2001).

Literature search will come up with a lot of hits concerning 3D perfusion bioreactors and their promising perspectives, on the other hand a lot of studies show the importance of oxygen tension in proliferation and differentiation of cells. However very limited information is available concerning oxygen distribution in 3D cultures. Volkmer et al. (2008) are the first to make a comparison of oxygen tension in static and perfusion conditions during culture. They showed that dynamic culture rescues cell survival and mitigates hypoxia in the centre of larger scaffolds. However, since they could only measure at three locations, local variation of oxygen tension could not be assessed. Cioffi et al. (2008) performed the first attempt to estimate local oxygen tension using a mixed approach consisting of two interlinked models. They modelled a scaffold based on homogeneous porous medium and placed a detailed µCT based model in the centre. The difference in oxygen tension between the two

models was found to be negligible. A more recent investigation used unit cells to model a part of the scaffold (Truscello et al. 2011). The aim was to compare the influence of model strategy on oxygen tension. In the first strategy oxygen consumption was presumed to take place in the entire fluid volume whereas in the second strategy oxygen consumption took place in a small cell layer close to the scaffold wall (mimicking a thin oxygen consuming cell layer). Simulations outcomes were found to be similar and comparable with results from analytical calculations.

However, despite these results presuming rather uniform oxygen tension conditions, our *in vitro* experimental results showed different behaviour for scaffolds of comparable porosity and pore size but of different material, both cultivated under the same conditions.

Our hypothesis was that actual micro architecture would influence local oxygen tension. The aim of this investigation therefore was to model oxygen tension inside two irregular scaffolds and try to relate the simulation results to the results from the *in vitro* experimental setup.

5. 2. MATERIALS AND METHODS

5. 2. 1. Geometry Reconstruction

Porous cylindrical titanium (Ti) and hydroxyapatite (HA) scaffolds were produced via gelcasting (Impens et al. 2009). The geometrical properties were characterized by micro-computed tomography (µ-CT). Briefly, radiographic images with a voxel resolution of 8 µm were acquired and reconstructed (HOMX 161 X-ray system with AEA Tomohawk CT-upgrade, Philips X-ray, Hamburg, Germany). The threshold gray value of the reconstructed images was determined by matching the material volume obtained from Archimedes porosity measurements to that of the solid 3D volume calculated in Tview (Skyscan, Kontich, Belgium) (Van Cleynenbreugel 2005). The geometrical scaffold characteristics are summarized in Table 5-1.

Table 5-1: Geometrical characteristics of the Ti and HA scaffolds

Scaffold	Diameter [mm]	Length [mm]	Porosity [%]	Mean pore size [mm]
Ti	5	4.2	77	0.28
HA	5	3.7	73	0.27

5. 2. 1. a. CFD model creation

Democells, an in-house meshing program based on the CGAL C++ library, was used to create triangular surface meshes from micro-CT images of the entire scaffold. The underlying algorithm (Boissonnat and Oudot 2005) warrants that the triangles satisfy strict quality and size constraints and approximate the scaffold surface within a user-defined error bound. The continuity conditions required by the algorithm were fulfilled by selecting an appropriate interpolation scheme for the micro-CT images and coarsening their resolution to match the level of detail desired from the mesh. To reduce the computational costs, the input images were coarsened to a triangle circumdiameter of 20 µm and 24 µm for the HA and the Ti geometrical model respectively. The boundary artefacts were removed using Mimics 13 (Materialise NV, Leuven, Belgium). A cylindrical guidance with a length of 0.5 mm was added above the inlet region to mimic realistic inlet conditions. Similarly, an outlet flow guidance of 0.5 mm was created in order to avoid problems caused by multiple outlets. As scaffolds were not perfectly circular we used Democells to model an elliptical cylinder (with little difference between the shortest and longest diameter (HA ratio 1 to 1.1; Ti ratio 1 to 1.03)) wrapped as tight as possible around the scaffold to mimic the conditions of a silicon tube. To avoid side flow between the cylindrical wall and the scaffold some extremities of the scaffold were cut off enabling a closer wrapping of the cylinder (Figure 5-1).

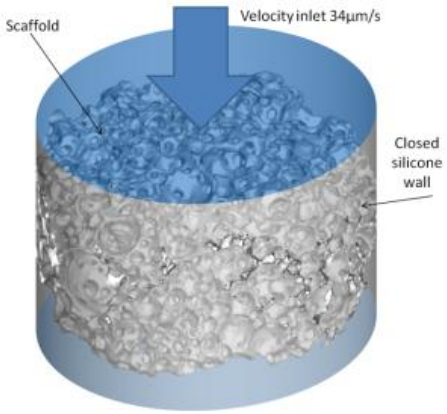

Figure 5-1: Boundary conditions adopted for the CFD calculations visualized on the HA scaffold. Velocity is based on 0.04 ml/min flow through a scaffold of 5 mm diameter. Flow direction is from top to bottom. Scaffold walls are colored light grey. Vertical cylindrical wall represents the silicone tubing around the scaffold. Openings in the wall occur when the scaffold makes contact with the silicone.

Starting from this surface mesh, a volume mesh was created using TGrid 5.0 (ANSYS, Inc., Lebanon, USA) consisting of $25 \cdot 10^6$ elements and $23 \cdot 10^6$ elements for the HA and the Ti scaffold respectively. A growth ratio of maximum 1.3 for neighbouring cells was used to gradually increase the 3D element size within the fluid volume in order to reduce the number of tetrahedral elements.

A uniform velocity profile of 34 µm/s (corresponding to a flow rate of 0.04 ml/min) through a circular area with a diameter of 5 mm) was imposed at the inlet of the flow guidance and the outlet pressure was set to zero Pa. The lateral walls of the scaffolds are embedded in a silicon tube and therefore they could correctly be modelled applying no slip boundary conditions.
The culture medium was assumed to be an incompressible and homogeneous Newtonian aqueous fluid with density ρ = 1000 kg/m³ and a measured dynamic viscosity of 8.51×10^{-4} Pa·s at 37°C.

5. 2. 1. b. Oxygen model

The oxygen distribution inside the domain was obtained by solving the steady state mass conservation law taking into account advection diffusion and consumption:

$$\rho \mathrm{v} \cdot \nabla c = \rho D \nabla^2 c - r \qquad 5\text{-}1$$

where c is the oxygen concentration, expressed in terms of mass fraction (ratio between oxygen mass and fluid mass), D is the diffusion coefficient of oxygen (equal to $3\cdot10^{-9}$ m^2/s when assuming water as diffusion medium), and r is the volumetric oxygen consumption rate (in $kg/s\cdot m^3$), r was set to zero in the inlet and outlet flow guidances and was assumed to follow a Michaelis-Menten (MM) kinetic law within the porous scaffolds' domain:

$$r = (r_{max,cell}\ \rho_{cell}) \frac{c}{K_m + c} \qquad 5\text{-}2$$

with $r_{max,cell}$ being the cellular maximum consumption rate, ρ_{cell} the volumetric cell seeding density (Truscello et al. 2011) and K_m corresponding to the oxygen concentration at which the consumption rate is equal to half of the maximum oxygen consumption rate.
A value of $r_{max,cell}$ equal to $3.8\text{x}10^{-17}$ mol/cell·s and a K_m of 0.68% of oxygen tension were adopted in this study, corresponding to the constants normally used for embryonic stem cells (Malda et al. 2004; Cochran et al. 2006). A ρ_{cell} equal to $2\cdot10^7$ cells/ml was assigned to both the HA and Ti scaffold. The oxygen tension at the inlet was taken equal to 5% corresponding to a mass fraction of $1.9\cdot10^{-6}$.

Calculations were done using Fluent 6.3 (ANSYS, Inc., Lebanon, USA). Plots are created with the aid of Tecplot 360 (Tecplot, Inc. Bellevue, WA, USA).

5. 2. 1. c. *In vitro* bioreactor experiments

In vitro cell seeding and culturing experiments of HA and Ti scaffolds were performed in a bioreactor with human periosteum derived cells (hPDCs), a heterogeneous cell population containing osteoprogenitor as well as more mature

bone cells (De Bari et al. 2008). When seeded on composite materials such as Collagraft™, VitOss® or NuOss™, hPDCs were reported to form bone *in vivo* after subcutaneous implantation in nude mice (Eyckmans and Luyten 2006; De Bari et al. 2008; Roberts et al. 2011).

Prior to cell seeding, Ti and HA scaffolds were cleaned, sterilized and prewetted in cell culture medium. Ti scaffolds were cleaned in an ultrasonic bath by immersing the scaffolds for 10 minutes in acetone, 10 minutes in ethanol 70% and 10 minutes in distilled water. HA scaffolds were gently rinsed with ethanol. Ti and HA scaffolds were dried overnight and sterilized by ethylene oxide. To enhance cell seeding, the scaffolds were prewetted in 1 ml cell culture medium (high glucose Dulbecco's modified Eagle's medium (D-MEM, Invitrogen, Merelbeke, Belgium) supplemented with 10% fetal bovine serum (FBS, io-Whittaker, Verviers, Belgium), 1% Antibiotic-antimycotic solution (100 units/ml penicillin, 100 mg/ml streptomycin and 0.25 mg/ml amphotericin B (Invitrogen), and 1% sodium pyruvate) (Vunjak-Novakovic and Radisic 2004) and dried overnight.

The bioreactor used in the investigation makes use of a peristaltic perfusion pump (IPC-24, Ismatec SA, Switzerland) that controls the perfusion flow through the scaffolds. To decrease the risk of cross-contamination and to allow easy manipulation of the bone constructs, each scaffold was seeded and cultured in an individual bioreactor circuit, composed of a medium reservoir and a bone chamber (Figure 5-2).

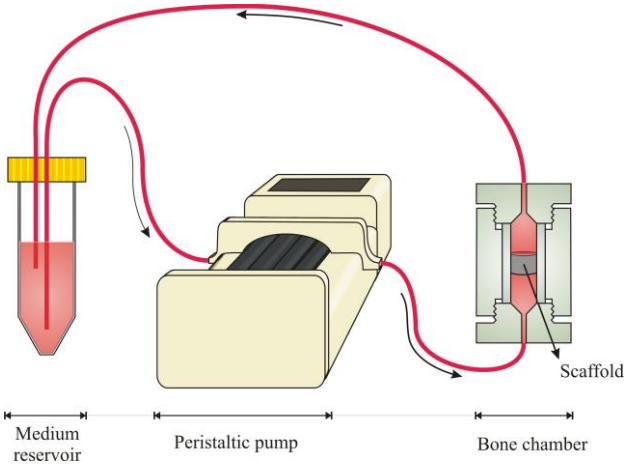

Figure 5-2: Schematic representation of a single bioreactor unit. Each circuit contains an individual medium reservoir and bone chamber, housing the perfused scaffold, which are interconnected via tubing. With the aid of a cassette, the soft-wall tubing passes a programmable peristaltic pump. The pump enables the culture of 24 bone constructs in parallel.

Both parts were interconnected via medical grade soft wall tubing (Pharmed Ismaprene, Ismatec SA) that passes the programmable, peristaltic pump via a two-stop cassette. Conical disposable falcon tubes (BD Biosciences, Belgium) served as medium reservoir. Holes in the lids allowed for incoming and outgoing culture medium.

The flow chambers were composed of non-disposable polycarbonate bone chambers. To ensure fluid flow through the centre of a scaffold, the perfused scaffolds were positioned in tightly enclosing silicon tubes (Degania Silicone, Germany) of 22 mm length and an outer diameter of 9 mm (equal to the inner diameter of the bone chamber).

All bioreactor experiments were performed in 10 ml of cell culture medium at a flow rate of 0.2 ml/min. HA and Ti scaffolds were seeded by adding $3 \cdot 10^6$ hPDCs to the mediumreservoir, and were subsequently cultured for 1 or 7 days. Cell culture medium was refreshed at day 1 and day 4.

The cellularity in the cultured TE constructs was characterized by a DNA based assay. Briefly, TE constructs were rinsed with 350 µl PBS 1X (Sigma) and vortexed during 5 seconds in 350 µl 0.05% Triton-X-100 cell lysis buffer. The lysed samples were spun down for 10 min at 180g. The supernatants were stored at -80°C prior to DNA analysis. The cellularity of the scaffolds was obtained with the aid of a fluorescent, Hoechst 33258 dye based, DNA Quantitation KIT (BIO-Rad, Veenendaal, the Netherlands), according to the manufacturer's instructions. The cellular fluorescent signal (CFS) was quantified with the aid of a Gemini fluorescence plate reader (Molecular Devices, Sunnyvale, CA, USA) and SoftmaxPRO software. The obtained values were expressed as a percentage of the average CFS of the TE constructs after seeding (CFS_s).

5. 3. RESULTS

5. 3. 1. In silico

5. 3. 1. a. Fluid dynamic environment, model prediction

Results of the hydrodynamic environmental parameters (fluid velocity field, wall shear stress) were discussed in detail in the publications of (Maes et al. 2009; Maes et al. 2012.). Briefly, the maximal fluid velocity in the HA scaffold (1.1 mm/s) was slightly higher compared to the maximal fluid velocity in the Ti scaffold (0.9 mm/s). Hence, the maximal surface wall shear stress (WSS) that occurred in the HA and Ti scaffold was in the same order of magnitude (0.025 Pa in the HA scaffold and 0.026 Pa in the Ti scaffold). Averaged surface WSS, however, was much lower than the maximal values (0.00109 Pa for the HA scaffold and 0.00141 Pa for the Ti scaffold). The large difference between the average and maximum WSS was the result of a largely skewed WSS distribution. Considering the pressure at the wall, a higher maximal value was noticed in the Ti scaffold (0.13 Pa) than in the HA scaffold (0.09

Pa). This higher value for Ti is mainly due to the fact that the Ti scaffold was longer than the HA scaffold. For a thorough description and discussion of the fluid dynamic environment we refer to chapter 4.

5. 3. 1. b. Oxygen tension, model prediction

The oxygen tension in the HA and Ti scaffolds are depicted in Figure 5-3. The oxygen tensions were visualized at the walls of the scaffolds. In order to link the hydrodynamic parameters (velocity and WSS) to each other, the steady flow pattern was visualized in the cut-plots using streamlines, colour-coded according to the local velocity magnitude.

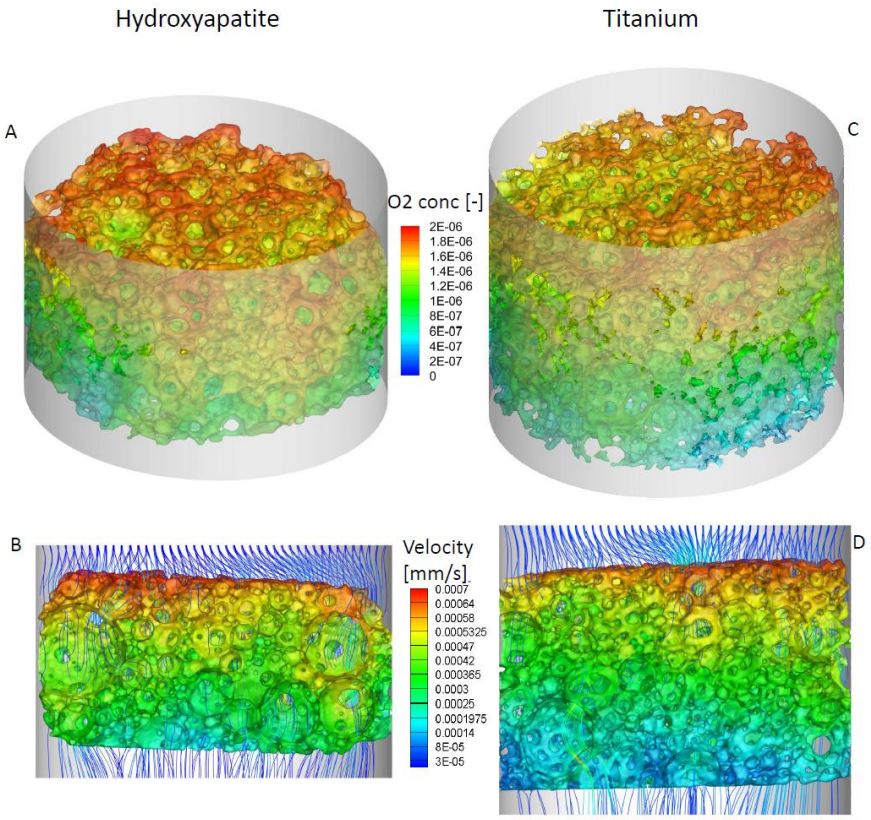

Figure 5-3: Oxygen concentration contour plots expressed as mass fraction in the HA (A and B) and Ti (C and D) scaffold. A and C show a 3D visualization of the oxygen values plotted at the wall. The cylindrical wall, representing the silicon tube in which the scaffold is positioned, is set transparent to enhance visibility. Streamlines colour-coded according to the velocity magnitude are added in B and D.

The model generally resulted in a gradual oxygen consumption throughout the depth of the HA and Ti scaffold. In case of homogenous oxygen distribution one would expect horizontal gradients however in our case disturbances in these gradient arise (left in the HA transversal plot, middle of the Ti transversal plot and Figure 5-3) these are likely to be caused by preferential flow paths, resulting in a better penetration of oxygen into the scaffold.
Oxygen tension at the outlet of the scaffold is lower for the Ti scaffold than for the HA scaffold, and correlated well with the length of the scaffold (see also lines of average oxygen tension in Figure 5-4) (Truscello et al. 2011).

In order to visualize the oxygen tension in the longitudinal direction (flow direction), several parallel cross sections (distance of 0.1 mm) were considered perpendicular to the direction of flow and for each cross-section the minimum, maximum and average of oxygen tension were calculated (Figure 5-4). Both the average and the maximal oxygen tension values show an almost linear decrease. However the minimum oxygen tension in the longitudinal direction shows more oscillations for the HA scaffold in particular in the middle of the scaffold.

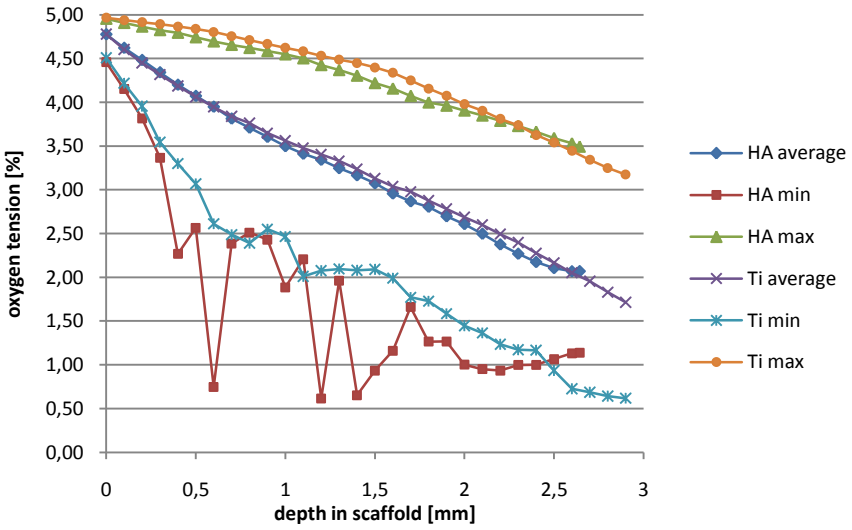

Figure 5-4. Graph showing oxygen tension versus the depth in the scaffold. Plotted values are from planes perpendicular to the direction of flow. Planes are drawn every 0.1 mm. In every plane maximal, average and minimal tensions are calculated and plotted.

A histogram of the oxygen tension values for the HA and Ti scaffold is plotted in Figure 5-5. Since the Ti scaffold is longer than the HA scaffold (and thus will have a lower oxygen tension at the outlet) it was virtually cut to the HA length thereby enabling a direct comparison. Furthermore Ti is modelled with a larger element size so the number of elements for both volumes did not match (HA: 2582154 and Ti: 2025215). Therefore numbers of cells are expressed as a percentage of the total

number of elements in the region of interest. Both frequency distributions show similar behaviour. However the HA scaffold tends to have more elements with a lower oxygen tension whereas higher oxygen tensions are more prominent in the elements of the Ti scaffold.

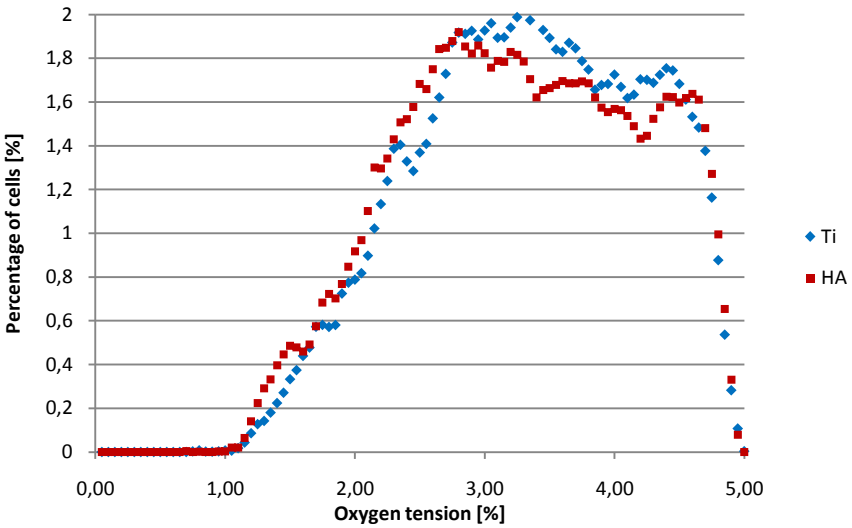

Figure 5-5: Histogram of oxygen concentration in Hydroxyapatite (HA) and Titanium (Ti) with 100 bins. To be able to compare results, the data for Ti are clipped to the size of the HA scaffold (by cutting the Ti scaffold). To enable comparison, the number of elements is expressed as a percentage.

5. 3. 2. In vitro

Bioreactor seeding of hPDCs on Ti and HA scaffolds resulted in a comparable cellularity (Figure 5-6, day 1).

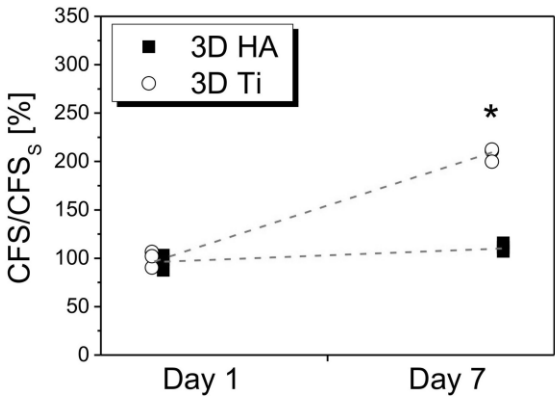

Figure 5-6. Cellularity in HA and Ti scaffolds in function of the culture time (day 1 versus day 7). The DNA content was expressed by the cellular fluorescent signal (CFS) compared to the average CFS obtained after seeding (CFS_s)(day 1).

Culturing cells for 7 days on HA and Ti scaffolds resulted in a doubling of CFS/CFS_s value in the Ti scaffolds compared to the HA scaffolds. The cellularity of the HA scaffolds after 7 days was not significantly higher compared to day 1. However, cells were able to proliferate, doubling the total cellularity, when cultured for 7 days on Ti scaffolds.

5. 4. DISCUSSION

This study aimed to quantify the oxygen tension in irregular scaffolds for bone tissue engineering. As a proof of principle two different scaffold materials having a comparable porosity and pore size were selected.

The negative slope reflecting the decrease in oxygen in the direction of flow shown in Figure 5-4 is similar to the ones reported by Malda et al. (2004) in static conditions and by volkmer et al. (2008) in a perfusion bioreactor. Cioffi et al. (2008) made a combined model by placing a detailed micro-CT based small sub model in a larger continuum Darcy based porous model. For two inlet flow conditions they found an almost linearly decreasing oxygen concentration as a function of scaffold depth. Simulations in regular scaffolds demonstrate similar outcome and thus allow designing a maximal scaffold length in order to avoid hypoxic zones (Truscello et al. 2011).

Despite the strong similarities of the oxygen concentration in the modelled HA and Ti scaffold in our *in silico* tests, the results from the *in vitro* tests indicated that the culture conditions in HA were less favourable for hPDC proliferation. In our previous study (see chapter 4) we tried to explain this phenomenon by the hydrodynamic parameters (fluid velocity, WSS). Our conclusion was that HA suffered from highly preferential flow paths. This conclusion could only be drawn from a visual perspective, since we had no quantitative measure for it. Since oxygen tension reflects residence time of the culture medium in the scaffold (Devarapalli et al. 2009) we were able to re-evaluate the former preliminary conclusion.

Preferential flows are marked by higher velocities so residence time of the culture medium is lower resulting in penetration of oxygen rich medium deeper into the scaffold. This should be noticeable as a higher maximal oxygen tension line in Figure 5-4. However Figure 5-4 displays almost no differences between the maximal oxygen tension of the HA compared to the Ti scaffold. This means that, if preferential flows were present in the HA scaffold, they were as prevalent as in the Ti scaffold.

The number of interconnections was another factor that was thought to influence the proliferative difference of hPDCs in both scaffolds. Since pores with very few

connections (one or two) flow rate is low, residence time of the culture medium is high thus more oxygen is consumed. Therefore this hypothesis could be interpreted as the prevalence of zones with lower oxygen levels. This is exactly what is displayed in Figure 5-7.

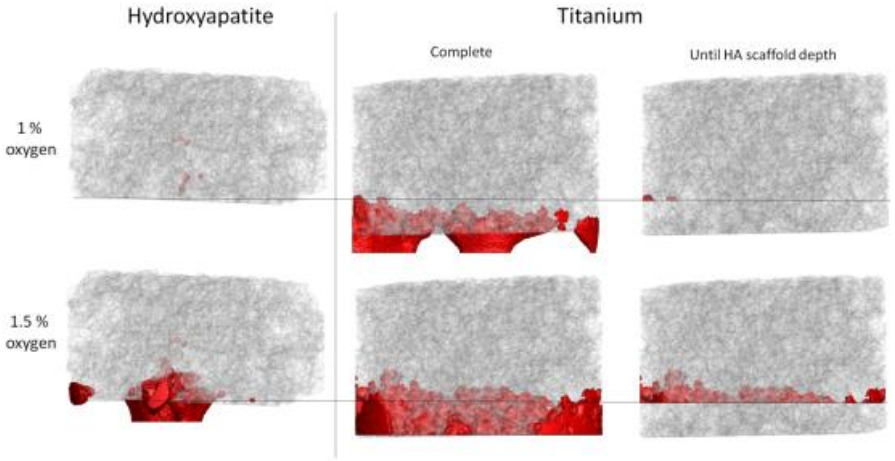

Figure 5-7. Contours of possible oxygen insufficiency drawn at 1% and 1.5 % oxygen tension for HA (left) and Ti middle and right). The structure is set highly transparent to make internal zones visible. Since Ti scaffold is longer than HA. To avoid the influence of scaffold length on oxygen concentration and to enable visible comparison between the two structures we visualized the oxygen insufficiency in titanium in the right part of the image only until the depth of the HA scaffold.

In HA local spots of low oxygen concentration are present, while in Ti no such locations are found. These spots correspond to the minimal oxygen concentration lines plotted in Figure 5-4. From this we quantitatively see that these local spots in HA show a very low concentration of oxygen. These spots in HA are small zones which are only connected by one or two channels. If we choose a higher minimal oxygen tension level (minimal level of 1.5%) we notice that for Titanium the zone of insufficient oxygen tension moves upwards of the scaffold in an almost uniform way (Figure 5-7). This is in contrast with HA. There we see that the initial spots of oxygen insufficiency are growing into the core of the scaffold. This is partly due to the presence of large pores close to the edge of the HA scaffold providing side flow.

These findings demonstrate that, however tempting to interpret the linear trend of the average oxygen tension value shown in Figure 5-4 as homogeneous consumption, one could never make a distinction between those two irregular scaffolds using a multiplication of unit cells or using a uniform porous model. Only because of a complete geometrical model, we could understand why the HA and Ti scaffold behaved differently under perfusion conditions. Simplified assumptions should only be used for modelling general behaviour or comparing average values. The available literature indeed demonstrates that there is not much difference

between modelling based on a detailed reconstruction of the inner architecture and general Darcy based porous modelling (Cioffi et al. 2008). They found a discrepancy between their detailed sub model and a Darcy based porous model of only 0.15%. A previous study about oxygen uptake in regular scaffolds also indicated that when oxygen consumption is assumed to take place in the entire fluid volume there is little variation between different modelling strategies (Truscello et al. 2011).

To be able to make accurate predictions of the oxygen consumption rate in a scaffold during perfusion, the dynamics of the cells and the synthesized matrix should be taken into account. Hence, the simulations performed in this study only provide information on the initial flow, WSS and oxygen distribution in perfused scaffolds. We hypothesize that the observed differences in initial *in vitro* proliferation of hPDCs in HA and Ti scaffolds are mainly caused by differences in the local oxygen tension, implying that the applied local model is able to generate information on the initial *in vitro* cell behaviour.

This hypothesis should be further investigated as the cell behaviour is not only related to the oxygen concentration, but also to parameters such as surface roughness, surface free energy and chemical composition (Hollister 2006).

5. 4. 1. Model limitations

The model proposed in this study, although computationally demanding because of its large number of cells, is a simplification of the reality. First of all, we modelled the cellular oxygen uptake as taking place in the whole scaffold void. A more realistic approach would be to model a thin layer close to the wall where oxygen consumption would take place like is previously done for regular scaffolds (Truscello et al. 2011). In reality however cells are seldom uniformly distributed inside a scaffold (Melchels et al. 2011). Additionally our model consists only of an empty scaffold. However, throughout the culturing process of a TE construct, the number of cells and, hence, the amount of matrix that is synthesized, will increase, thereby occupying an increasing volume, that alters the geometrical shape of the fluid volume. To follow oxygen tension during perfusion one should model the geometrical changes based on the dynamics of cell proliferation (Chung et al. 2006; Chung et al. 2007; Chung et al. 2008; Chung et al. 2010) and models of matrix deposition (Sengers et al. 2004). Such combined simulations are promising but today they can only be used on very simple geometries.

Despite these limitations our models permitted to give a quantify the oxygen availability at the very start of the perfusion process. And they showed to be valid in explaining differences of in vitro culture results.

5. 5. CONCLUSIONS

This study aimed to quantify the oxygen tension in irregular scaffolds for bone tissue engineering. As a proof of principle two different scaffold materials (titanium and hydroxyapatite) having a comparable porosity and pore size were selected. Surprisingly a different *in vitro* outcome was observed. By detailed modelling of the entire micro architecture we could demonstrate that the HA scaffold suffers from local zones of low oxygen tension. These hypoxic zones likely are the cause of the rather disappointing cell proliferation during *in vitro* culture. To investigate the importance of scaffold micro architecture we compared our results with averaged oxygen tension values which were incapable of showing any distinction between both structures. This emphasise that sub models and models consisting of unit cells cannot be used to study local differences in oxygen tension.

5. 6. REFERENCES

Boissonnat, J. D. and S. Oudot (2005). "Provably good sampling and meshing of surfaces." Graphical Models **67**(5): 405-451.

Chung, C. A., C. P. Chen, T. H. Lin and C. S. Tseng (2008). "A compact computational model for cell construct development in perfusion culture." Biotechnology and Bioengineering **99**(6): 1535-1541.

Chung, C. A., C. W. Chen, C. P. Chen and C. S. Tseng (2007). "Enhancement of cell growth in tissue-engineering constructs under direct perfusion: Modeling and simulation." Biotechnology and Bioengineering **97**(6): 1603-1616.

Chung, C. A., T. H. Lin, S. D. Chen and H. I. Huang (2010). "Hybrid cellular automaton modeling of nutrient modulated cell growth in tissue engineering constructs." Journal of Theoretical Biology **262**(2): 267-278.

Chung, C. A., C. W. Yang and C. W. Chen (2006). "Analysis of cell growth and diffusion in a scaffold for cartilage tissue engineering." Biotechnology and Bioengineering **94**(6): 1138-1146.

Cioffi, M., J. Kuffer, S. Strobel, G. Dubini, I. Martin and D. Wendt (2008). "Computational evaluation of oxygen and shear stress distributions in 3D perfusion culture systems: Macro-scale and micro-structured models." Journal of Biomechanics **41**(14): 2918-2925.

Cochran, D. M., D. Fukumura, M. Ancukiewicz, P. Carmeliet and R. K. Jain (2006). "Evolution of oxygen and glucose concentration profiles in a tissue-mimetic culture system of embryonic stem cells." Annals of Biomedical Engineering **34**(8): 1247-1258.

De Bari, C., F. Dell'Accio, A. Karystinou, P. V. Guillot, N. M. Fisk, E. A. Jones, D. McGonagle, I. M. Khan, C. W. Archer, T. A. Mitsiadis, A. N. Donaldson, F. P. Luyten and C. Pitzalis (2008). "A biomarker-based mathematical model to predict bone-forming potency of human synovial and periosteal mesenchymal stem cells." Arthritis & Rheumatism **58**(1): 240-250.

Devarapalli, M., B. J. Lawrence and S. V. Madihally (2009). "Modeling Nutrient Consumptions in Large Flow-Through Bioreactors for Tissue Engineering." Biotechnology and Bioengineering **103**(5): 1003-1015.

Eyckmans, J. and F. P. Luyten (2006). "Species Specificity of Ectopic Bone Formation Using Periosteum-Derived Mesenchymal Progenitor Cells." Tissue Engineering **12**(8): 2203-2213.

Goldstein, A. S., T. M. Juarez, C. D. Helmke, M. C. Gustin and A. G. Mikos (2001). "Effect of convection on osteoblastic cell growth and function in biodegradable polymer foam scaffolds." Biomaterials **22**(11): 1279-1288.

Hollister, S. J. (2006). "Porous scaffold design for tissue engineering (vol 4, pg 518, 2005)." Nature Materials **5**(7): 590-590.

Hollister, S. J. and W. L. Murphy (2011). "Scaffold Translation: Barriers Between Concept and Clinic." Tissue Engineering Part B-Reviews **17**(6): 459-474.

Impens, S., R. Schelstraete, J. Luyten, S. Mullens, I. Thijs, J. van Humbeeck and J. Schrooten (2009). "Production and characterisation of porous calcium phosphate structures with controllable hydroxyapatite/beta-tricalcium phosphate ratios." Advances in Applied Ceramics **108**(8): 494-500.

Lewis, M. C., B. D. MacArthur, J. Malda, G. Pettet and C. P. Please (2005). "Heterogeneous proliferation within engineered cartilaginous tissue: The role of oxygen tension." Biotechnology and Bioengineering **91**(5): 607-615.

Maes, F., T. Claesens, M. Moesen, H. Van Oosterwyck, P. Van Ransbeeck and P. Verdonck (2012). "CFD models for wall shear stress estimation; a comparative study of two complete scaffold geometries."

Maes, F., P. Van Ransbeeck, H. Van Oosterwyck and P. Verdonck (2009). "Modeling fluid flow through irregular scaffolds for perfusion bioreactors." Biotechnol Bioeng **103**(3): 621-30.

Malda, J., J. Rouwkema, D. E. Martens, E. P. le Comte, F. K. Kooy, J. Tramper, C. A. van Blitterswijk and J. Riesle (2004). "Oxygen gradients in tissue-engineered PEGT/PBT cartilaginous constructs: Measurement and modeling." Biotechnology and Bioengineering **86**(1): 9-18.

Malladi, P., Y. Xu, M. Chiou, A. J. Giaccia and M. T. Longaker (2006). "Effect of reduced oxygen tension on chondrogenesis and osteogenesis in adipose-derived mesenchymal cells." American Journal of Physiology-Cell Physiology **290**(4): C1139-C1145.

Martin, I., T. Smith and D. Wendt (2009). "Bioreactor-based roadmap for the translation of tissue engineering strategies into clinical products." Trends in Biotechnology **27**(9): 495-502.

Martin, I., D. Wendt and M. Heberer (2004). "The role of bioreactors in tissue engineering." Trends in Biotechnology **22**(2): 80-86.

Melchels, F. P. W., B. Tonnarelli, A. L. Olivares, I. Martin, D. Lacroix, J. Feijen, D. J. Wendt and D. W. Grijpma (2011). "The influence of the scaffold design on the distribution of adhering cells after perfusion cell seeding." Biomaterials **32**(11): 2878-2884.

Muschler, G. E., C. Nakamoto and L. G. Griffith (2004). "Engineering principles of clinical cell-based tissue engineering." Journal of Bone and Joint Surgery-American Volume **86A**(7): 1541-1558.

Roberts, S. J., L. Geris, G. Kerckhofs, E. Desmet, J. Schrooten and F. P. Luyten (2011). "The combined bone forming capacity of human periosteal derived cells and calcium phosphates." Biomaterials **32**(19): 4393-4405.

Sengers, B. G., C. C. Van Donkelaar, C. W. J. Oomens and F. P. T. Baaijens (2004). "The local matrix distribution and the functional development of tissue engineered cartilage, a finite element study." Annals of Biomedical Engineering **32**(12): 1718-1727.

Truscello, S., J. Schrooten and H. Van Oosterwyck (2011). "A Computational Tool for the Upscaling of Regular Scaffolds During In Vitro Perfusion Culture." Tissue Engineering Part C-Methods **17**(6): 619-630.

Van Cleynenbreugel, T. (2005). Porous Scaffolds for the Replacement of Large Bone Defects: A Biomechanical Design Study. Biomechanics and Engineering Design. Leuven, Belgium, Katholieke Universiteit Leuven.

Volkmer, E., I. Drosse, S. Otto, A. Stangelmayer, M. Stengele, B. C. Kallukalam, W. Mutschler and M. Schieker (2008). "Hypoxia in static and dynamic 3D culture systems for tissue engineering of bone." Tissue Engineering Part A **14**(8): 1331-1340.

Vunjak-Novakovic, G. and M. Radisic (2004). Cell Seeding of Polymer Scaffolds

Biopolymer Methods in Tissue Engineering. A. P. Hollander and P. V. Hatton, Humana Press. **238:** 131-145.

Yeatts, A. B. and J. P. Fisher (2011). "Bone tissue engineering bioreactors: Dynamic culture and the influence of shear stress." Bone **48**(2): 171-181.

Chapter 6 GENERAL CONCLUSIONS AND FUTURE PROSPECTS OF PART A

The first section of this chapter summarizes the contents of the main of this investigation part. The most important conclusions are highlighted and discussed in relation to the goals of this investigation. The second section indicates some perspectives for future research

6. 1. SUMMARY AND CONCLUSIONS

Despite ever growing knowledge in different fields of tissue engineering, the technique of tissue culture is still far from being a standard medical procedure. One of the main causes for this is that biological systems, as always, show a very complex design. Therefore a lot of studies focus on trying to unravel biological pathways in order to enhance insight in stem cell behaviour. However since almost all such studies are performed on monolayer setups, the outcome of those studies is seldom directly transferable to a 3D system. As such the lack of adequate quantification and control sometimes results in unsatisfying 3D perfusion tissue culture outcome.

This investigation is therefore dedicated to deepen our understanding of the impact of the local fluid dynamic environment in scaffolds for perfusion bioreactors. Because of the micro scale it is however impossible to directly measure flow in scaffolds. Therefore we used µCT images as input for computational fluid dynamic (CFD) simulations

As a proof of principle this investigation uses two irregular scaffolds, both having comparable porosity and pore size, but gelcasted from a different material (hydroxyapatite (HA) and titanium (Ti)). In vitro tests showed that, despite HA being mineral form of bone, cells proliferated best in Ti. Since bone tissue engineering culture was done under perfusion of a culture medium it was hypothesized that local variations in fluid dynamical environment might be causing this unexpected outcome.

Following the introductory chapters 1 and 2, chapter 3 described a first attempt to simulate fluid dynamic environment inside two scaffolds with a focus to wall shear stress. Because of computational cost, simulations were only performed on small cubic sub models. To investigate if our model sufficiently covered the heterogeneity of scaffold, the cubic CFD model was subdivided in concentric regions of interest from which the WSS was calculated. This was repeated in both scaffolds for a cubic

model with an edge length of 1 mm and a model with an edge length of 1.5 mm. From the results it was concluded that:

- Average wall shear stress is approximately 30% higher in Titanium compared to Hydroxyapatite. This was however not found conclusive to explain the different in vitro response between the two scaffolds.
- Average wall shear stress is approximately 30% higher in the 1.5 mm models compared to the 1 mm models suggesting important influence of model size.
- Sub models are subjected to boundary artefacts caused by closing pores at the lateral side of the model. Averaged wall shear stress should therefore be estimated on a concentric region inside the model. The region should be at least the distance of one pore away from the lateral boundary to minimize boundary artefacts.

In chapter 4 we developed two models of entire irregular scaffolds in order to avoid problems caused by unrealistic boundary conditions inevitable when using small sub models. To allow comparison the scaffold geometries were exactly the same as in chapter 3. Similarly as in chapter 3 the domain is also subdivided in concentric regions of interest to study the minimal size of the region of interest. The results were used to propose guidelines for sub model creation. These guidelines were reflected on the available literature to test if the reported models were sufficiently covering the heterogeneity of the modelled the irregular scaffold. From this study it was concluded that:

- Average wall shear stress is again approximately 30% higher in Titanium compared to Hydroxyapatite but the estimated values are 30% lower compared to the previous study indicating the model size in chapter 3 was probably not large enough.
- The Hydroxyapatite has more zones with extreme low wall shear stress indicating zones of very slow flow. This could indicate that the different results during in vitro culture might be due to a mass transport problem implying a shortage of nutrients, possible hypoxia or accumulation of waste products causing intoxication.
- Guidelines are difficult to set. We propose a minimal model size of at least six times the pore size for more regular scaffolds. If scaffolds show more irregular internal architecture the model should be at least eight to ten times the pore size.
- Results from models in literature should be interpreted with precaution as, according to our proposed lower bound for model size, all but one of the examined models were too small to cover heterogeneity sufficiently.

Since chapter 4 indicated that the hydroxyapatite scaffold might have zones where the concentration of oxygen might be too low, the CFD models are extended in

Chapter 5 as functions are added that describe oxygen consumption. From the simulation results in this chapter it can be concluded that:

- Oxygen consumption causes a more or less gradual decrease in oxygen tension from the inlet to outlet. Thus limiting the maximal length of a scaffold.
- Preferential flows where velocities are relatively high result local zones where oxygen tension is higher than the surrounding zone. They are found in both scaffolds. However they are more prevalent in titanium.
- In hydroxyapatite there exist local pores which show hypoxia. These zones tend to enlarge if higher oxygen tension levels are required. They are most likely pores with very few interconnections.
- The oxygen model is able to explain the different in vitro response of both scaffolds. This would not have been possible using a simplified models which are not able to model local oxygen tension.

The above mentioned conclusions demonstrate that CFD models are a powerful tool useful for simulating the fluid dynamic environment in irregular scaffolds for bone tissue engineering, achieving the general aim. Meanwhile we demonstrated that sub models show non negligible influence from boundary artefacts. Using models of entire scaffolds we could provide guidelines for sub model creation. The oxygen simulations could explain why cells did not proliferate in the hydroxyapatite scaffold whereas they did proliferate in a titanium scaffold. Hence the two intermediate goals were also achieved.

However, still some limitations can be recognized:

- All simulations just reflect the conditions at that moment as they do not allow for temporal variation. They cannot cope with geometrical changes due to matrix deposition and do not account for changes in cell density or cell metabolic activity occurring during tissue engineering culture.
- Our simulations are only performed on two distinct scaffolds. Further investigation is needed in order to validate the results.

6. 2. FUTURE PERSPECTIVES

As mentioned above the models used in the investigation have their limitations and as such they have to be considered as a solid start point for further investigation. Some aspects are related to extending the predictive capacity of the models while others involve additional research to extend the validation of the simulated results.

6. 2. 1. Wall shear stress models

The current simulations are performed in empty scaffolds so estimated wall shear stress is only exerted on the scaffold wall without taking into account the presence of cells. Taking the actual cell geometry in account will however result in far more computational demanding models since the element size needs to be small enough to capture the cell geometry. Therefore those simulations are better performed in simplified models consisting of unit cells and the outcome might be incorporated in the detailed 3D model as a multiplication factor to obtain the actual wall shear stress. This multiplication factor might be related to channel diameters since cells have a higher chance to have a bridged morphology in narrow channels.

However this adjustment will only be valid just after seeding. Once cells proliferate and matrix deposition starts the actual geometry will change rapidly. To this respect the models need to be extended with functions that describe cell proliferation and matrix deposition and their dependence to wall shear stress. The most difficult step in these investigations will not be the development of the models but finding the shear stress magnitudes that trigger or abort these processes and the development of setups to validate these models.

6. 2. 2. Oxygen models

In our current model oxygen is assumed to be consumed in the entire scaffold void. In reality however cells are attached to the wall and from a thin layer where oxygen consumption takes place. We tried modelling this thin layer using a boundary mesh but mesh generation continuously failed. Such modelling is reported in regular scaffolds making use of unit cells (Truscello et al. 2011) and compared to our approach but was not found to be significantly different. We hypothesize that these findings are because of the surface/volume ratio in regular scaffolds being a constant value contrarily to irregular scaffolds with a variety of large pores and small channels. Most likely modelling oxygen uptake in a thin layer will enlarge the extremes of high and low oxygen zones. Oxygen uptake in preferential flows will be comparably lower because of the low surface/volume ratio while zones of small flow often have a higher ratio so oxygen uptake will be comparably higher.

Also our oxygen models are temporally static and do not take into account changes in cell density and metabolic activity. An extension with cell proliferation models will enhance insight in temporal behaviour of in vitro culture.

Furthermore not only oxygen tension but also other nutrient might limit tissue growth and could be implemented in future modelling investigations

6. 2. 3. References

Truscello, S., J. Schrooten and H. Van Oosterwyck (2011). "A Computational Tool for the Upscaling of Regular Scaffolds During In Vitro Perfusion Culture." Tissue Engineering Part C-Methods **17**(6): 619-630.

PART B:

EMBRYONIC HEARTS:
HOW DO THEY PUMP

Chapter 7 PROLOGUE

This prologue depicts the main motivation of the research part, deploys the organisation and postulates the research goals.

7. 1. INTRODUCTION

The heart is an amazing pumping organ. The more we get to know about it the more we get astonished by its ingenuity and its design. One of its unique capabilities is that it maintains function during development.

The heart is the first organ to start functioning. At that time the heart is a straight tube lacking any valves. Despite the simplicity of design this tube is capable of generating unidirectional flow; as we all know, a vital function which remains crucial throughout our entire live.

During heart development the heart undergoes multiple morphological changes. It is widely accepted that the driving force behind the morphological development is an interplay between genetics and fluid-mechanical factors (Hove et al. 2003). Evidently the main cause for the fluid-mechanical influences and back couplings during development is of course the pumping of the heart itself.

The pumping mechanism of this first stage heart flow has been a subject of recent debate (Manner et al. 2010). From visual perspective the pumping action is caused by generating contraction-like waves sweeping along the tubular wall from the inlet of the heart towards the outlet. The question is how the wall is able to generate wavelike motions.

There exist two possible ways to achieve net flow in valveless elastic flexible tubes:

- Peristalsis (Manner et al. 2008)
- Dynamic suction pumping (Forouhar et al. 2006)

The main motivation of this investigation is therefore to get better insight in how the embryonic heart is pumping. Understanding the working principle of simple heart might allow identification of important mechanical principles that can be applied to the complex human heart.

7. 2. ORGANISATION

Our approach was to evaluate the pumping mechanism of embryonic hearts. This necessitates high resolution (both spatial and temporal) imaging of in vivo cardiac

cell motions within a beating embryonic heart. Acquiring and analyzing data required demonstrations of principles from interdisciplinary studies, including biology and engineering. Image processing tools have been developed to provide several quantitative measurements and qualitative descriptions of cardiac mechanics.

This research is built upon three milestones which are discussed in deep in the following chapters

- development of an easy and effective tool to characterize flow in the aorta
- derivation of activation mechanism through outline of the heart muscle wall
- creation of drug induced anomalies in the pumping mechanism and relate the distorted functioning to the current embryonic heart pumping models

Chapter 2 Vertebrate heart development
The chapter provides essential background information for the research presented. We review heart development in vertebrates and explain why zebrafish are the model of choice to study dynamic cardiac function. We describe the current viewpoints concerning pumping models of the embryonic heart and mention the research outline.

Chapter 3 An effective tool for measuring embryonic heart velocities
This chapter introduces a tool for rapid measurement of aortic flow. We enumerate the advantages of investigating aortic flow and we describe the methods currently used in research. We introduce four new methods developed to fulfill the necessary requirements for easy and accurate blood velocity measuring. Each method is briefly described, together with specific requirements regarding image preprocessing and post-processing. All methods are tested for robustness and accuracy compared to a predefined ground truth and to the linescan method described in literature (Malone et al. 2007).

Chapter 4 Influence of age and drugs on aortic blood flow in zebrafish embryos
Here we apply the method evaluated in the previous chapter on two types of zebrafish embryos. We examine blood flow from the age of 28 hours post fertilization (hpf) until 34 hpf to investigate the influences of rapid cardiac development on aortic flow. The same method is used to investigate the influence of BDM, a drug that affects the response of heart muscle cells to the cardiac electrical signal. We define parameters to describe the influence of age and drug treatment in terms of cardiac contractility and relaxation.

Chapter 5 Wall motion to understand the pumping mechanism of embryonic hearts
This is an investigation of the motion of the heart wall. The chapter starts with a detailed introduction about both peristalsis and dynamic suction as pumping models for the vertebrate embryonic heart. We describe the methodology to outline the heart

wall and compare the wall motion results with results of the cardiac electrical signal reported in literature. The similarity between both is discussed.

Next we use a drug that influences the response of cardiac muscle cells to the electrical signal order to induce irregularities in the heart wall motion. We succeed in causing a situation that presents evidence contradicting dynamic suction. To this respect we then thoroughly discuss both peristalsis and dynamic suction by comparing pros and contras of both methods for embryonic heart pumping.

Taking into account the discussed points we propose a hypothetical pumping model aiming to connect the wall characteristics with the observed fluid motion characteristics. Finally we give some future prospects.

7. 3. GOALS

The major goal of this study is to enhance our insight in the pumping mechanism of embryonic hearts. Along the way some intermediate technical goals were also established:

- Quantitative assessment of aortic blood velocity as a tool for rapid comparison between embryos or treatments
- Qualitative assessment of heart wall motion to understand if all muscle cells contribute actively to the pumping mechanism

7. 4. REFERENCES

Forouhar, A. S., M. Liebling, A. Hickerson, A. Nasiraei-Moghaddam, H. J. Tsai, J. R. Hove, S. E. Fraser, M. E. Dickinson and M. Gharib (2006). "The embryonic vertebrate heart tube is a dynamic suction pump." Science **312**(5774): 751-753.

Hove, J. R., R. W. Koster, A. S. Forouhar, G. Acevedo-Bolton, S. E. Fraser and M. Gharib (2003). "Intracardiac fluid forces are an essential epigenetic factor for embryonic cardiogenesis." Nature **421**(6919): 172-177.

Manner, J., L. Thrane, K. Norozi and T. M. Yelbuz (2008). "High-resolution in vivo Imaging of the cross-sectional deformations of contracting embryonic heart loops using optical coherence tomography." Developmental Dynamics **237**(4): 953-961.

Manner, J., A. Wessel and T. M. Yelbuz (2010). "How Does the Tubular Embryonic Heart Work? Looking for the Physical Mechanism Generating Unidirectional Blood Flow in the Valveless Embryonic Heart Tube." Developmental Dynamics **239**(4): 1035-1046.

Chapter 8 VERTEBRATE HEART DEVELOPMENT

This chapter provides the necessary background information on vertebrate heart development with a focus on the tubular heart stage. We present the benefits of using the zebrafish as cardiovascular model and introduce the current viewpoint on the pumping mechanism of embryonic hearts.

8. 1. INTRODUCTION

The first documentations of the embryonic heart go back to Aristotle's observations of pulsating heart tubes in 3 day old chick embryos (as cited by Manner et al. (2010)). Since that time generations of scientists have been fascinated by the visual experience of the jumping points on top of the egg's yolk. Our current knowledge of the development and functioning of the vertebrate embryonic heart in tubular stage is synthesized in the next paragraphs.

8. 2. VERTEBRATE HEART MORPHOGENESIS

The cardiovascular system is the first major system in the embryo that starts functioning. The primordial heart and vascular system appear in the third week of human development. This early development of a circulatory system is necessary because the rapidly growing embryo can no longer satisfy its nutritional and oxygen requirements by diffusion alone. Consequently, there is a need for an efficient method of acquiring oxygen and nutrients from the maternal blood and removal of carbon dioxide and waste products (Cochard and Netter 2002; Larsen 2008; Moore and Persaud 2008). The driving forces of this process are mentioned to be an interplay balanced interplay between a genetic program and the influence of fluid mechanical stimuli (Hove et al. 2003).

8. 2. 1. Human heart development

The earliest sign of the heart is the appearance of paired endothelial strands called angioblastic cords during the third week of development (Figure 8-1B). These cords will canalize to form two thin tubes (Figure 8-2 A).

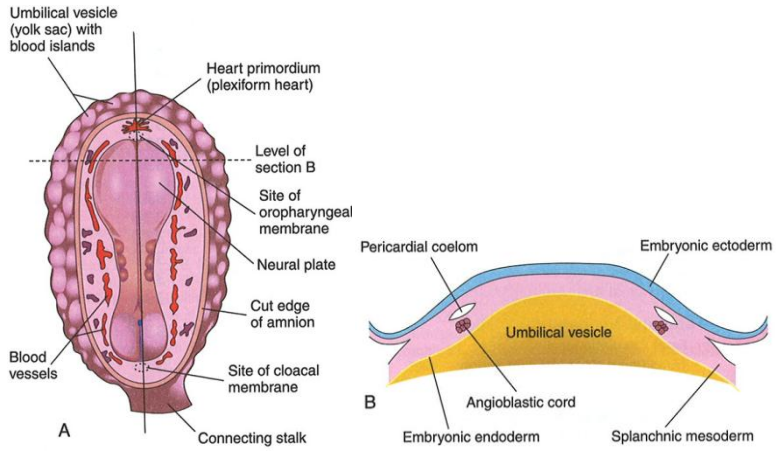

Figure 8-1. Early development of the heart. A) Dorsal view of an embryo (approximately 18 days). B) Transverse section of the embryo demonstrating the angioblastic cords in the cardiogenic mesoderm (from Cochard and Netter (2002)).

8. 2. 1. a. Heart tube formation (Figure 8-2 A-C)

As the two heart tubes fuse, the external layer of the embryonic heart – the primordial myocardium – is formed. The fusion begins at the cranial end (towards the head) of the heart tubes and extends caudally (towards the tail). At the end of the fusion the developing heart is composed of a thin endothelial tube separated from a thick primordial myocardium by a gelatinous connective tissue – cardiac jelly – of which role is still uncertain. The endothelial tube becomes the internal layer of the heart wall, also called endocardium. The myocardium becomes the muscular wall of the heart (Figure 8-2).

Although the human heart is presumed to begin beating at around the 21st embryonic day, observations of embryonic chick, mouse and zebrafish hearts suggest that the cardiomyocytes are already beating as they form the primary heart tube (Fye 1987). At first, the beating only results in an ebb and flood type motion of flow. Unidirectional flow is established soon after the formation of primary heart tube by day 28.

8. 2. 1. b. Heart looping (Figure 8-2 D-E)

Because of rapid growth of the bulbus cordis and ventricle the heart starts bending upon itself forming an S-shaped bulboventricular loop. The process of looping has been regarded as a key process in cardiac morphogenesis and pathologists have speculated since the beginning of the 20th century that several forms of congenital cardiac malformations might result from disturbances in looping morphogenesis (Manner 2009). The signalling molecules responsible for cardiac looping have been intensively studied but remain largely unknown (for reviews we refer to (Harvey 1998; Linask and VanAuker 2007)). A lot of studies describe the mechanical influence during this process (Manasek et al. 1972; Zamir et al. 2003; Nerurkar et al.

2006; Taber 2006; Filas et al. 2007; Ramasubramanian et al. 2008; Garita et al. 2011).

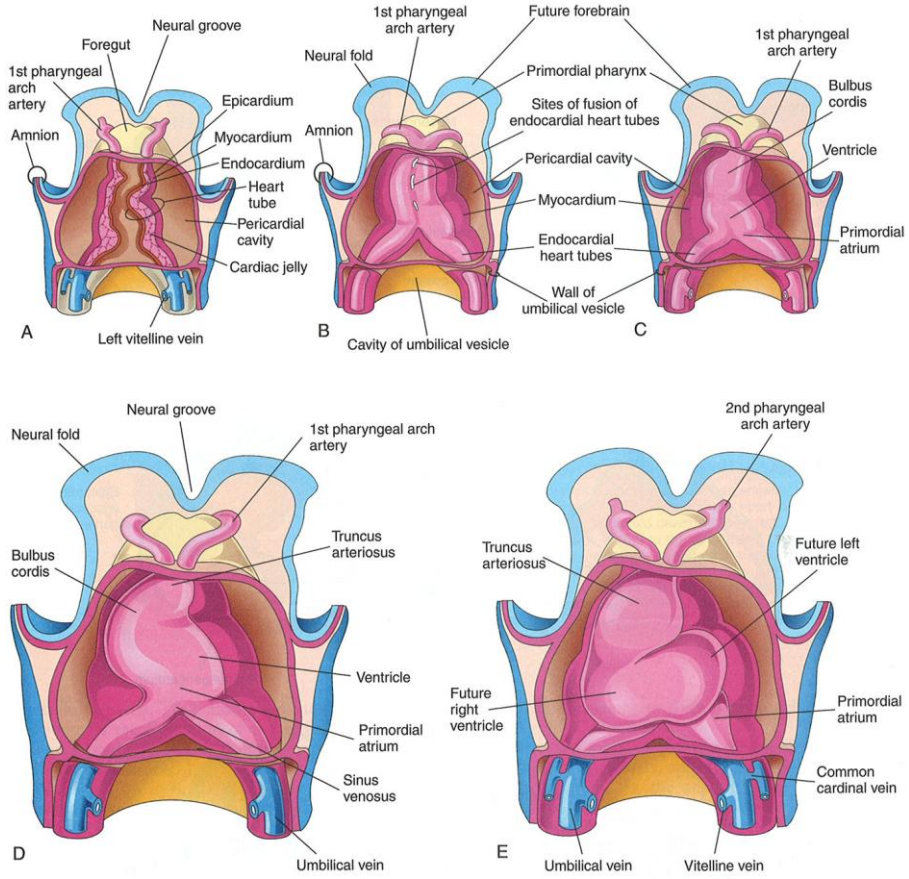

Figure 8-2. A-C) Ventral views of the developing heart (22-35 days). The ventral pericardial wall has been removed to show the developing myocardium and fusion of the two heart tubes to form a single tube. D-E) As the heart elongates it forms regional segments and bends upon itself resulting in an S-shaped heart (from Cochard and Netter (2002)).

8. 2. 1. c. Subsequent heart development stages

In the subsequent stages the premature heart will undergo partitioning to form chambers. The onset of this stage is marked by the development of endocardial cushions forming a separation between the primordial atrium and the primordial ventricle (the transition from tubelike pumping to chamberlike pumping is nicely modelled by Taber et al. (2007). These cushions will then develop into valves. A lot of investigations have been carried out to understand this process partly with the aim of in vitro tissue engineering of heart valves (for further reading we refer to (Schroeder et al. 2003; Butcher and Markwald 2007; Butcher et al. 2007; Keller 2007; Martin and Bartman 2009; Vermot et al. 2009)

In animals where the pulmonary circulation is separated from the systemic circulation the heart will transform from a single channel pump into a double channel pump were both halves will pump synchronously. This septation process will split the atrium, the ventricle and the outflow tract (for review we refer to (Lamers and Moorman 2002)).

8. 3. THE TUBULAR HEART

8. 3. 1. Anatomy of the tubular heart

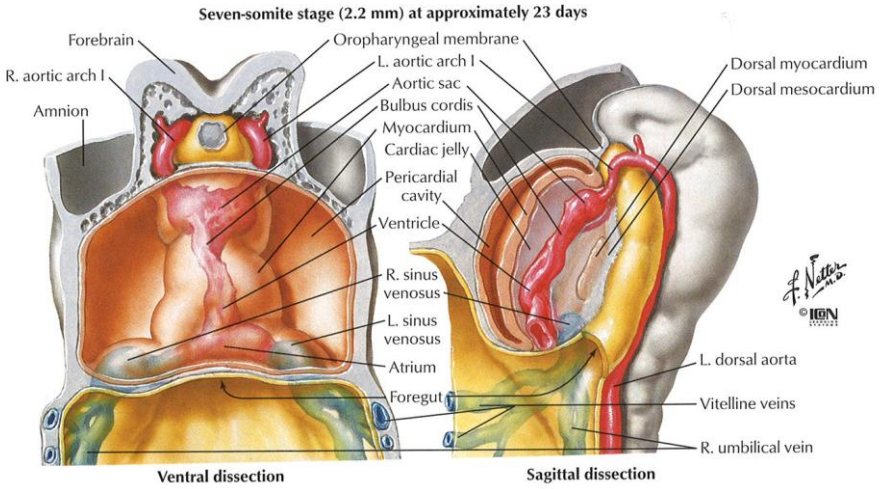

Figure 8-3. Anatomy of the embryonic human heart at 23 days (tubular heart stage).

At the tubular heart stage the heart consists of an endothelial wall in direct contact with the blood, a middle cell free extracellular matrix layer called cardiac jelly (Davis 1924) and an outer myocardial tube in direct contact with the pericardial fluid. The heart is attached through the mesoderm at the gut. The frontal side is in touch with the pericardial fluid and is able to move more freely.

8. 3. 2. Physiology of the tubular heart

Although the obvious function of the tubular heart is to pump blood, very little is known about the actual mechanism of pumping. Since no chambers or valves are present the pumping mechanism of this heart differs considerably form mature vertebrate hearts.

Blood circulation in the primordial heart is as follows: Blood enters through the sinus venosus into the primordial atrium. Peristalsis-like waves pump blood through the atrioventricular canal and the primordial ventricle into the bulbus cordis and

truncus arteriosus from which it is distributed through the aortic sac into the pharyngeal arch arteries (Figure 8-4).

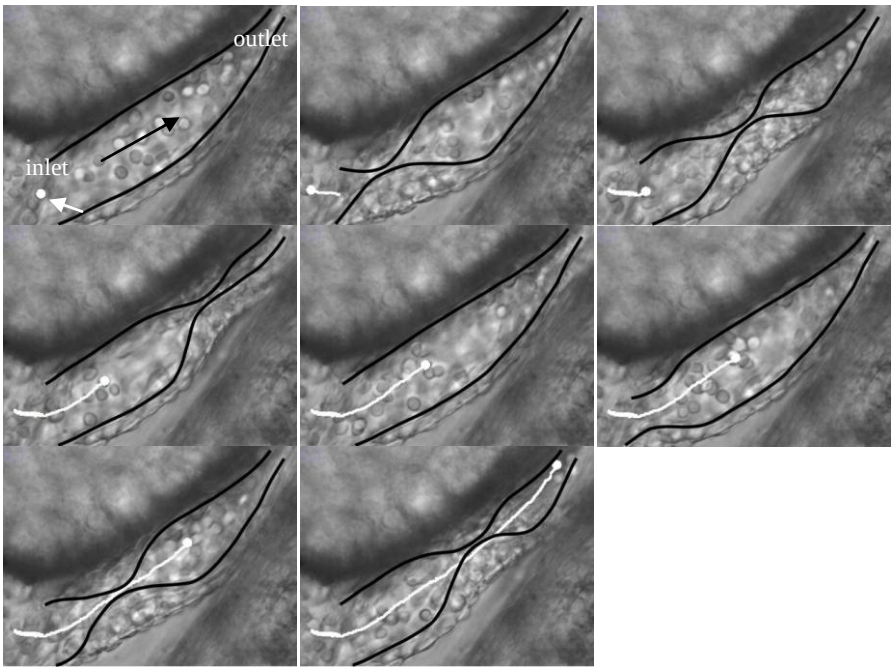

Figure 8-4. Image sequence with a time interval of 150 ms illustrating the peristalsis-like waves in the endothelial heart wall in combination with the track of one blood cell in a 30 hours post fertilization (hpf) zebrafish embryo in tubular heart stage. The endothelial heart wall is collared black, the white arrow point at the blood cell under consideration, the track of the blood cell is collared white, the black arrow indicates direction of flow. Notice that it takes two heart cycles for the blood to be pumped through the heart. (Maes et al. 2009)

Figure 8-4 shows that the contraction initially pushes blood sideways in both directions. As the occlusion moves towards the outlet is causes the blood to be sucked in. A subsequent contraction is needed to pump blood out of the heart in the primitive circulatory system.

8. 3. 3. Conducting system

As in the adult heart, active muscle contractions in the embryonic heart are induced by an electrical signal (Moorman et al. 2004; Chi et al. 2008). The signal originates by specialised cells called the pacemaker cells or sinoatrial node located close to the inlet of the heart and travelling towards the outlet. This depolarisation can be visualised as a change in intra-cellular calcium concentration. Chi and co-workers (2008) were able to use transgenic reporter constructs to convert this to an optical signal in embryonic zebrafish hearts. The results are shown in Figure 8-5.

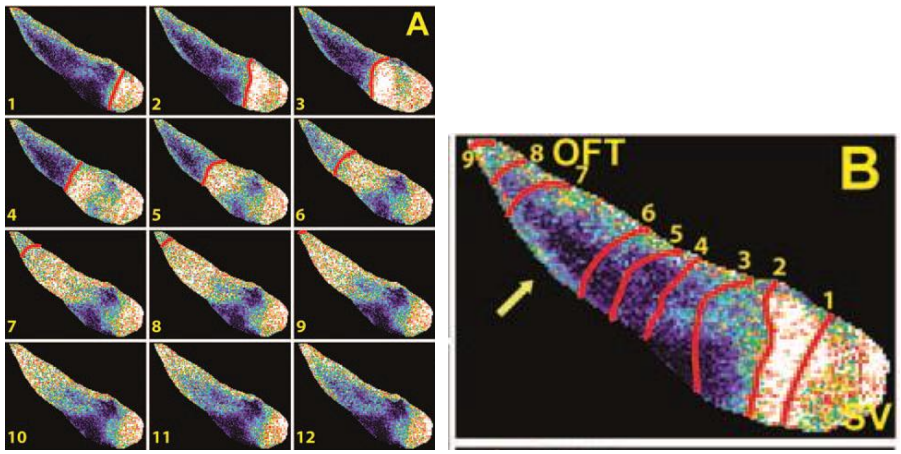

Figure 8-5 Cellular and In Vivo Electrophysiologic Analysis of 24 hpf Wild-Type Hearts (A) Sequential calcium activation images of a 24 hpf wild-type Tg(cmlc2:gCaMP)^{s878} heart during a single cycle in a live zebrafish embryo. (B) A 24 hpf optical map of calcium excitation represented by isochronal lines every 60 ms. SV: sinus venosus (inlet region), OFT: outflow tract(outlet region) (reproduced from Chi et al. (2008))

Figure 8-5 demonstrates that the electrical signal starting from the pacemaker cells shows slow linear conduction with no significant delays across the 24 hpf heart tube. This is in contrast with later stages in development where there is a distinctive delay between atrial and ventrical contractions.

8. 4. ANIMAL MODELS IN HEART DEVELOPMENT

8. 4. 1. Heart development in animal models

Because of obvious ethical reasons various animal models have been used in cardiogenesis research. The oldest reported model is probably the chick embryo. (Aristotle 384-322 B.C.). Other models commonly used to study cardiac development are embryo's of mice, amphibians, fruitflies and zebrafish.

In all vertebrates heart development shares the following four consequent stages: (i) heart tube formation, (ii) looping, (iii) chamber formation, and (iv) valve formation (for comparison between species see (Fishman and Chien 1997; Moorman and Christoffels 2003; Xavier et al. 2007) (for the further discussion the following animal groups are considered vertebrates: fish, amphibians, reptiles, and mammals)). The duration of cardiac morphogenesis, number of chambers, and final shape of the mature heart are specific to each species.

Table 8-1. Comparative table of milestones in cardiac development in human and different animals models used in cardiogenesis research. dpc: days post conception; HH hamburger-Hamilton staging (Hamburger and Hamilton 1951); hpf: hours post fertilisation dpc: days post conception. Table is adapted from (Fishman and Chien 1997)

	human	**mouse**	**chick**	**zebrafish**
Migration of precardiac cells	15-16 days	7 dpc	HH 4 18-22 hrs	5.5 hpf
Heart tube formation	22 days	8 dpc	HH 9 29-33 hrs	19 hpf
Coordinated contractions	23 days	8.5 dpc	HH 10 33-38 hrs	22 hpf
Looping	23 days	8.5 dpc	HH 11 40-45 hrs	33 hpf
Cushion formation	28 days	9.5 dpc	HH 17 50-56 hrs	48 hpf

8. 4. 2. Animals models in the study of the pumping mechanism of the tubular heart

Even though many animal models are used in heart development research only few are suitable to study the pumping mechanism of the embryonic heart. Extracorporeal and favourably transparent embryo's facilitate accessibility for *in vivo* imaging. So far studies regarding the pumping mechanism of the heart prior to valve formation are reported in embryo's of chicken *Galus galus* domesticus (Fano and Bandano 1890; Barry 1948; Dejong et al. 1992; Sakai et al. 1996; Vennemann et al. 2006; Maenner et al. 2009), quail *Coturnix ypsilophora* (Jenkins et al. 2007), fruitfly (*Drosophila spec*) (Wu and Sato 2008) and in zebrafish (*Danio rerio*) (Forouhar et al. 2006; Chi et al. 2008; Maes et al. submitted)

8. 4. 3. Zebrafish as a model of choice in heart development

The zebrafish, named after his black and white stripes, is a 3-4 cm long fresh water fish commonly found in the Ganges river. This model has gained increasing interest in the clinical and biological communities to study vertebrate heart development (for review of cardiac morphogenesis in zebrafish we refer to Yelon (2001)). It has several advantages of which we sum up a few:

- External development in transparent eggs
- Abundant offspring (several hundred from one mating)
- Rapid development (develops a mature heart in 5 days)
- Not critically dependent on the heart for several days after fertilization (unlike other vertebrate models)
- Genetically well documented (entire genome is sequenced and a lot of genetic mutants have been produced which mimic human cardiac malformations)
- Transparent (facilitating imaging) (see also Figure 8-6 A-C)
- Several transgenic strains express fluorescence in different tissue cell types (facilitating focus on the organs of target while imaging, Figure 8-6 D-H)

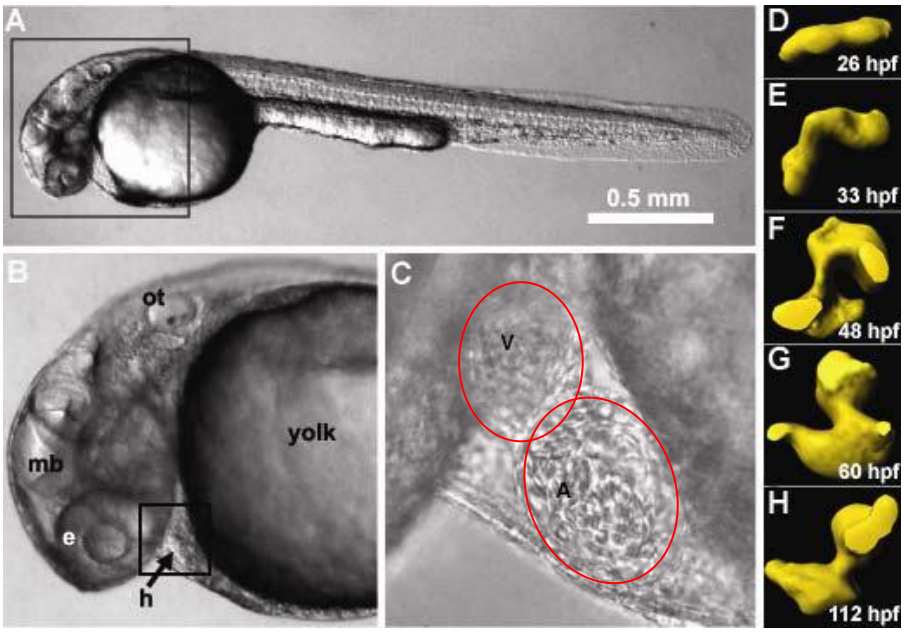

Figure 8-6 A) Embryonic zebrafish. B) Magnification showing the position of the heart. C) Enlargement with focus on the heart; atrium (A) and ventricle (V) are visible (red ellipses). D-H) 3D reconstructions of the embryonic heart during mid diastole (adapted from Liebling et al. (2006))

Despite the many advantages of using zebrafish in cardiac development research one has to keep in mind that fish are very different from humans and that results from this investigation can never quantitatively transferred to the human embryonic heart. Despite this major drawback the simple geometrical shape of the tubular heart is comparable between all vertebrate species.

8. 5. PUMPING MODELS OF THE EMBRYONIC HEART

There exists two model to describe the pumping mechanism of tubular embryonic hearts: peristalsis and dynamic suction. Peristalsis is the oldest model. Dynamic suction is introduced in 2006 by Forouhar and co-workers as novel model for the embryonic heart (Forouhar et al. 2006) (Figure 8-7).

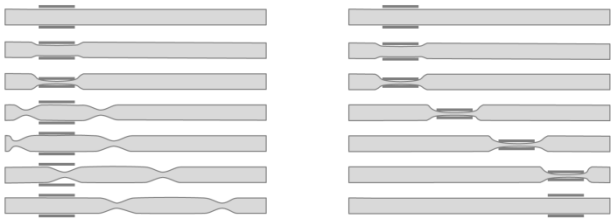

Figure 8-7 Illustration showing the working principle of dynamic suction (left) and peristalsis (right) in a tubular heart (after Hickerson et al. (2005))

Dynamic suction is characterized by a single contraction site. From there passive waves run through the heart in both directions. The wave running towards the inlet reaches its end first and reflects. Both waves, now running in the same direction, enclose a volume of fluid called the suction bolus which is transported towards the outlet of the heart.

Peristalsis on the other hand is characterized by a sequence of active contractions moving along the longitudinal axis of the heart tube. The principle relies on the coupling between the electrical signal (Figure 8-5) and the resulting muscle contraction as the electrical signal slowly moves along the longitudinal axis of the heart.

The two abovementioned pumping mechanisms both have arguments pro and contra (for details see chapter 11). The key difference between these two pumping mechanisms is the number of active contraction sites: dynamic suction is characterized by one site whilst peristalsis demonstrates sequential activation of multiple adjacent sites. Despite this simple distinction a recent review by Manner et al. (2010) notes “the question regarding how the embryonic hearts works still awaits an answer”.

8. 6. RESEARCH OUTLINE

The aim of this investigation is to get better insight in the pumping mechanism of the embryonic heart. We will do this in 2 steps:

During the first step we will create a fast and reliable method capable of detecting changes in aortic blood flow which we will need for the next step.

In the second step we will use two pathways to investigate how the heart is activated. First we will carry out a detailed study of the heart wall motion in normal embryos and compare this with the calcium transients published by Chi et al. (2008) in order to see if both show parallel behaviour. Secondly, we will pharmacologically disconnect this calcium flux - contraction relationship to induce abnormal wall motions. The aortic flow algorithm will be used to detect drug influences.

8. 7. REFERENCES

Barry, A. (1948). "The functional significance of the cardiac jelly in the tubular heart of the chick embryo." anat rec **102**.

Butcher, J. T. and R. R. Markwald (2007). "Valvulogenesis: the moving target." Philosophical Transactions of the Royal Society B-Biological Sciences **362**(1484): 1489-1503.

Butcher, J. T., T. C. McQuinn, D. Sedmera, D. Turner and R. R. Markwald (2007). "Transitions in early embryonic atrioventricular valvular function correspond with changes in cushion biomechanics that are predictable by tissue composition." Circulation Research **100**(10): 1503-1511.

Chi, N. C., R. M. Shaw, B. Jungblut, J. Huisken, T. Ferrer, R. Arnaout, I. Scott, D. Beis, T. Xiao, H. Baier, L. Y. Jan, M. Tristani-Firouzi and D. Y. R. Stainier (2008). "Genetic and physiologic dissection of the vertebrate cardiac conduction system." Plos Biology **6**(5): 1006-1019.

Cochard, L. R. and F. H. Netter (2002). Netter's atlas of human embryology, elsevier.

Davis, C. L. (1924). "the cardiac jelly of the chick embryo (abstract) " And. Rec. **27**.

Dejong, F., T. Opthof, A. A. M. Wilde, M. J. Janse, R. Charles, W. H. Lamers and A. F. M. Moorman (1992). "PERSISTING ZONES OF SLOW IMPULSE CONDUCTION IN DEVELOPING CHICKEN HEARTS." Circulation Research **71**(2): 240-250.

Fano, G. and F. Bandano (1890). "Étude physiologique des premiers stades de développemnt du coeur embryonnaire de poulet." Arch Ital Biol **13**: 387-422.

Filas, B. A., I. R. Efimov and L. A. Taber (2007). "Optical coherence tomography as a tool for measuring morphogenetic deformation of the looping heart." Anatomical Record-Advances in Integrative Anatomy and Evolutionary Biology **290**(9): 1057-1068.

Fishman, M. C. and K. R. Chien (1997). "Fashioning the vertebrate heart: Earliest embryonic decisions." Development **124**(11): 2099-2117.

Forouhar, A. S., M. Liebling, A. Hickerson, A. Nasiraei-Moghaddam, H. J. Tsai, J. R. Hove, S. E. Fraser, M. E. Dickinson and M. Gharib (2006). "The embryonic vertebrate heart tube is a dynamic suction pump." Science **312**(5774): 751-753.

Fye, W. B. (1987). "THE ORIGIN OF THE HEART BEAT - A TALE OF FROGS, JELLYFISH, AND TURTLES." Circulation **76**(3): 493-500.

Garita, B., M. W. Jenkins, M. D. Han, C. Zhou, M. VanAuker, A. M. Rollins, M. Watanabe, J. G. Fujimoto and K. K. Linask (2011). "Blood flow dynamics of one cardiac cycle and relationship to mechanotransduction and trabeculation during heart looping." American Journal of Physiology-Heart and Circulatory Physiology **300**(3): H879-H891.

Hamburger, V. and H. Hamilton (1951). "A series of normal stages in the development of the chick embryo." Journal of Morphology **88**(1): 53.

Harvey, R. P. (1998). "Cardiac looping - an uneasy deal with laterality." Seminars in Cell & Developmental Biology **9**(1): 101-108.

Hickerson, A. I., D. Rinderknecht and M. Gharib (2005). "Experimental study of the behavior of a valveless impedance pump." Experiments in Fluids **38**(4): 534-540.

Jenkins, M. W., D. C. Adler, M. Gargesha, R. Huber, F. Rothenberg, J. Belding, M. Watanabe, D. L. Wilson, J. G. Fujimoto and A. M. Rollins (2007). "Ultrahigh-speed optical coherence tomography imaging and visualization of the embryonic avian heart using a buffered Fourier Domain Mode Locked laser." Optics Express **15**(10): 6251-6267.

Keller, B. B. (2007). "New insights into the developmental biomechanics of the atrioventricular valves." Circulation Research **100**(10): 1399-1401.

Lamers, W. H. and A. F. M. Moorman (2002). "Cardiac septation - A late contribution of the embryonic primary myocardium to heart morphogenesis." Circulation Research **91**(2): 93-103.

Larsen, W. J. (2008). Human embryology, Churchil Livingstone.

Liebling, M., A. S. Forouhar, R. Wolleschensky, B. Zimmermann, R. Ankerhold, S. E. Fraser, M. Gharib and M. E. Dickinson (2006). "Rapid three-dimensional imaging and analysis of the beating embryonic heart reveals functional changes during development." Developmental Dynamics **235**(11): 2940-2948.

Linask, K. K. and M. VanAuker (2007). "A role for the cytoskeleton in heart looping." Thescientificworldjournal **7**: 280-297.

Maenner, J., L. Thrane, K. Norozi and T. M. Yelbuz (2009). "In Vivo Imaging of the Cyclic Changes in Cross-sectional Shape of the Ventricular Segment of Pulsating Embryonic Chick Hearts at Stages 14 to 17: A Contribution to the Understanding of the Ontogenesis of Cardiac Pumping Function." Developmental Dynamics **238**(12): 3273-3284.

Maes, F., B. Chaudhry, P. Segers, P. Van Ransbeeck and P. Verdonck (2009). Visualization and modeling of flow in the embryonic heart. 4th European Conference of the International Federation for Medical and Biological Engineering. J. V. P. N. M. H. J. VanderSloten. **22:** 1875-1878.

Maes, F., B. Chaudhry, P. Van Ransbeeck and P. Verdonck (submitted). "Why the tubular heart is a peristaltically activated pump instead of a dynamic suction pump." Journal of biomechanical engineering.

Manasek, F. J., M. B. Burnside and R. E. Waterman (1972). "MYOCARDIAL CELL SHAPE CHANGE AS A MECHANISM OF EMBRYONIC HEART LOOPING." Developmental Biology **29**(4): 349-371.

Manner, J. (2009). "The Anatomy of Cardiac Looping: A Step Towards the Understanding of the Morphogenesis of Several Forms of Congenital Cardiac Malformations." Clinical Anatomy **22**(1): 21-35.

Manner, J., A. Wessel and T. M. Yelbuz (2010). "How Does the Tubular Embryonic Heart Work? Looking for the Physical Mechanism Generating Unidirectional Blood Flow in the Valveless Embryonic Heart Tube." Developmental Dynamics **239**(4): 1035-1046.

Martin, R. T. and T. Bartman (2009). "Analysis or Heart Valve Development in Larval Zebrafish." Developmental Dynamics **238**(7): 1796-1802.

Moore, K. L. and T. V. N. Persaud (2008). Developing Human Clinically Oriented Embryology, Saunders.

Moorman, A. F. M. and V. M. Christoffels (2003). "Cardiac chamber formation: Development, genes, and evolution." Physiological Reviews **83**(4): 1223-1267.

Moorman, A. F. M., A. T. Soufan, J. Hagoort, P. A. J. De Boer and V. M. Christoffels (2004). Development of the building plan of the heart. Cardiac Engineering: From Genes and Cells to Structure and Function. S. Sideman and R. Beyar. New York, New York Acad Sciences. **1015:** 171-181.

Nerurkar, N. L., A. Ramasubramanian and L. A. Taber (2006). "Morphogenetic adaptation of the looping embryonic heart to altered mechanical loads." Developmental Dynamics **235**(7): 1822-1829.

Ramasubramanian, A., N. L. Nerurkar, K. H. Achtien, B. A. Filas, D. A. Voronov and L. A. Taber (2008). "On Modeling Morphogenesis of the Looping Heart Following Mechanical Perturbations." Journal of Biomechanical Engineering-Transactions of the Asme **130**(6).

Sakai, T., A. Hirota and K. Kamino (1996). "Video-imaging assessment of initial beating patterns of the early embryonic chick heart." Japanese Journal of Physiology **46**(6): 465-472.

Schroeder, J. A., L. F. Jackson, D. C. Lee and T. D. Camenisch (2003). "Form and function of developing heart valves: coordination by extracellular matrix and growth factor signaling." Journal of Molecular Medicine-Jmm **81**(7): 392-403.

Taber, L. A. (2006). "Biophysical mechanisms of cardiac looping." International Journal of Developmental Biology **50**(2-3): 323-332.

Taber, L. A., J. M. Zhang and R. Perucchio (2007). "Computational model for the transition from peristaltic to pulsatile flow in the embryonic heart tube." Journal of Biomechanical Engineering-Transactions of the Asme **129**(3): 441-449.

Vennemann, P., K. T. Kiger, R. Lindken, B. C. W. Groenendijk, S. Stekelenburg-de Vos, T. L. M. ten Hagen, N. T. C. Ursem, R. E. Poelmann, J. Westerweel and B. P. Hierck (2006). "In vivo micro particle image velocimetry measurements of blood-plasma in the embryonic avian heart." Journal of Biomechanics **39**(7): 1191-1200.

Vermot, J., A. S. Forouhar, M. Liebling, D. Wu, D. Plummer, M. Gharib and S. E. Fraser (2009). "Reversing Blood Flows Act through klf2a to Ensure Normal Valvulogenesis in the Developing Heart." Plos Biology **7**(11).

Wu, M. M. and T. N. Sato (2008). "On the Mechanics of Cardiac Function of Drosophila Embryo." Plos One **3**(12): 7.

Xavier, J., R. A. Castro, A. C. Sampaio, A. P. Azambuja, H. A. Castillo, R. M. Cravo and M. S. Simoes-Costa (2007). "Parallel avenues in the evolution of hearts and pumping organs." Cellular and Molecular Life Sciences **64**(6): 719-734.

Yelon, D. (2001). "Cardiac patterning and morphogenesis in zebrafish." Developmental Dynamics **222**(4): 552-563.

Zamir, E. A., V. Srinivasan, R. Perucchio and L. A. Taber (2003). "Mechanical asymmetry in the embryonic chick heart during looping." Annals of Biomedical Engineering **31**(11): 1327-1336.

Chapter 9 AN EFFECTIVE TOOL FOR MEASURING AORTIC BLOOD VELOCITIES IN ZEBRAFISH EMBRYOS

After a description of the methods currently used we outline the requirements for a method for easy blood velocity detection in zebrafish embryos. We propose two automated methods and one method for post processing in order to obtain one single velocity wave. All methods are evaluated for accuracy compared to manual tracking.

9. 1. INTRODUCTION

From ancient times heart characteristics have been derived from the peripheral vasculature. The best known example is probably checking someone's pulse pressure. Already ancient Egyptian writings describe the link between pulse pressure measurements and heart condition (Vlachopoulos and O'Rourke 2000). Superficial arteries have been used in characterizing heart function because arteries show far less complicated behaviour than a multi-chambered pumping organ and accessibility is not hindered by a chest.

9. 1. 1. Advantages of measuring blood flow in the embryonic aorta

Similarly as in adult vertebrates, measuring velocities in the embryonic zebrafish aorta has several advantages:

- Simple geometry, straight tube
- Cells follow linear pathways
- Easily accessible during development
- No moving wall interference; blood cells are the only cause of motion
- Images are completely in focus during entire heart cycle

In our study, measurements are done in the dorsal aorta. This vessel runs from the heart towards the tail of the embryo. Several branches outflow the aorta to provide blood to developing organs. We therefore choose a location as close as possible to the heart that could be easily located and was not visually blocked by the presence of the yolk sac (Figure 9-1 and Figure 9-2).

This location is distant from the heart and as such it has its limitations. When for example cardiac output is calculated from velocity measurements at that location one has to keep in mind that cranial flow is not incorporated.

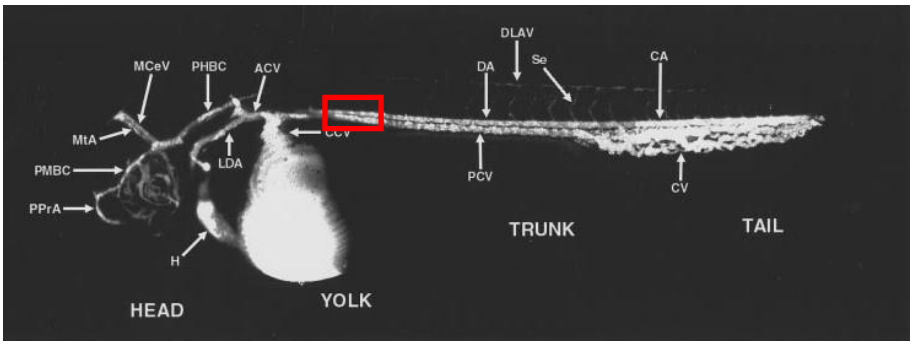

Figure 9-1. A confocal microscopy angiogram of a 36 hpf zebrafish embryo obtained from Isogai et al. (2001). The red box shows the imaging location of the dorsal aorta used in this study.

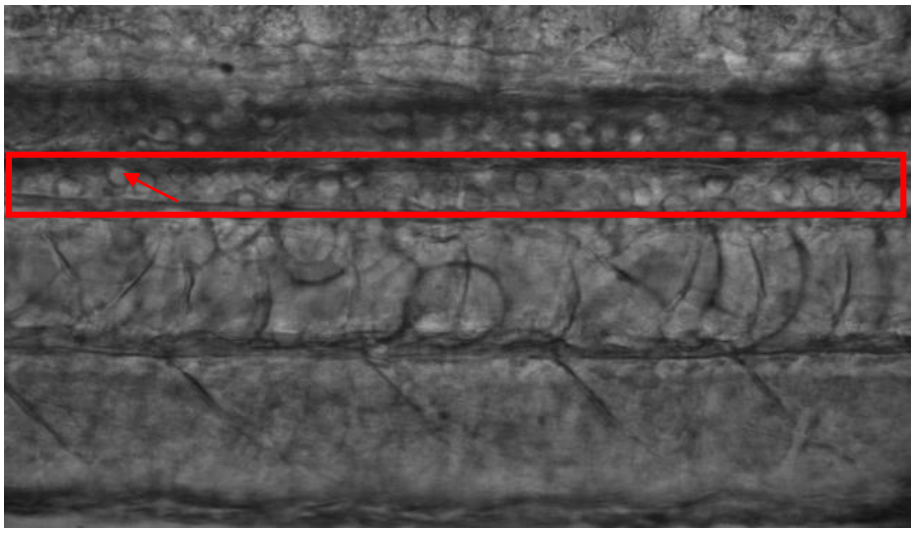

Figure 9-2. Typical bright field microscope image representing a part of a 30 hpf zebrafish aorta with length 0.25mm. Red box shows the aorta, red arrow points to a red blood cell (8µm), image is taken at the location shown in Figure 9-1.

9. 1. 2. Aortic velocity measuring methodologies in embryos

Several methods are currently being used in embryonic zebrafish research to estimate blood flow.

9. 1. 2. a. Cell tracking

Manual cell tracking is the most simple way of deriving blood velocities in small animal embryos. Displacement of cells divided by the time elapsed between subsequent frames results in an estimate of the blood velocity. The method is used in several investigations but is very time consuming (Schwerte and Pelster 2000; Schwerte and Fritsche 2003; Bagatto 2005; Forouhar et al. 2006).

9. 1. 2. b. Linescan

Linescan is a method described by Malone et al. (2007). Linescans are images constructed with laser scanning microscopes by repeatedly imaging the same one pixel wide line.

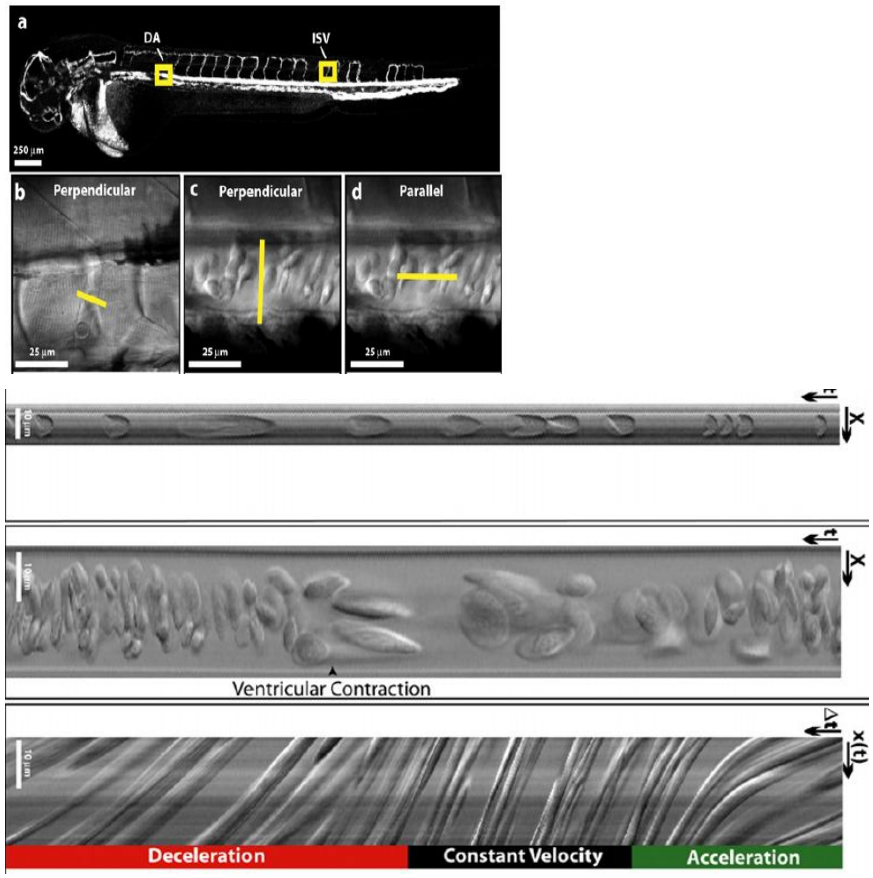

Figure 9-3. Principle of a linescan: horizontal axis represents time, vertical axis represents the scanline. Adapted from Malone et al. (2007).

Linescans typically contain spatial information in the x-dimension and temporal information in the y-dimension (or vice versa). A linescan acquired in the longitudinal direction of the dorsal aorta shows a series of lines of which the slope is inversely proportional to the velocity. Although this is an appealing method, lines have to be tracked manually.

9. 1. 2. c. Cardiac output through volume changes

Strictly this is not a method to estimate velocities since it only results in a volume per beat. It is often used to characterized heat pumping efficiency. The method relies on (manually) outlining the embryonic heart at diastole (relaxed state) and at systole (contracted state) in 2D images. The difference in surface multiplied by an estimate of the size of the heart in the dimension perpendicular to the image under

assumption the heart is a spheroid results in the stroke volume of the heart. Multiplying by the heart rate results in the cardiac output. This methods has been used in several investigations, but is only applicable when chambers are present (Burggren and Fritsche 1995; Hou and Burggren 1995; Fritsche and Burggren 1996; Mirkovic and Rombough 1998; Burggren 2004). This method gives an indication of cardiac output but is far from accurate since the actual volume is not known and since regurgitant flow is not taken in account.

9. 1. 2. d. Optical coherence tomography

This technique is the optical counterpart of CT (X ray Computer Tomography) used in clinic to visualize internal body structures. In transparent embryos it is possible to use wavelengths in the visual spectrum (or near infrared for better tissue penetration). Motion is often detected with Spectral Doppler techniques. Changes in wavelength (or color in visual spectrum) are used to obtain velocity information of a structure coming towards a source (shorter wavelength) or moving away from the source (longer wavelength). This technique is increasingly being investigated in embryology (Iftimia et al. 2008; Davis et al. 2009). The drawbacks are the cost and complexity of the hardware. Often temporal resolution is too low to obtain accurate instantaneous velocities (Davis et al. 2008).

All the above mentioned methods require either manual handling or very complex and expensive hardware. In one point or another they are all very time consuming to obtain results and therefore not applicable for comparative investigations between multiple embryos.
There is an absolute lack of any suitable pre-existing methodology for quantifying flow in microscope derived image series. This has been a hindrance to many types of biological research.

9. 1. 3. Method requirements

Considering the drawbacks for frequent use of the previously described methods the newly developed method should match the following requirements.

- Hardware:
  - Easy to use (no complex setup)
  - Cheap (e.g. bright field microscope with camera)
- Software
  - Reliable
  - Accurate
  - Robust
  - Fast (preferably automated)

We developed several fully automatic image based methods. The methods will be explained and quantitatively evaluated in the next paragraphs.

9. 2. AUTOMATIC METHODS FOR ESTIMATING BLOOD VELOCITIES IN BRIGHT FIELD IMAGES.

9. 2. 1. Image pre-processing

Since blood velocity estimation is based on the displacement of blood cells between two frames, blood cells have to be detectable. This presents a challenge since in bright field images the background is omnipresent. (Figure 9-4). We used two different methods.

9. 2. 1. a. Temporal image subtraction

This is one of the simplest methods to remove the background, in case targets are subjected to motion. We performed additional rescaling to avoid loss of negative values (Figure 9-5). Chan et al. (2009) used a variant of this technique to derive heart rate variability in zebrafish using the flow in the lower aorta. Also, Schwerte and Pelster (2000) used this technique to facilitate location of red blood cells in zebrafish embryos.

After processing these images show banana shaped displacement arches of which the centre point matches that of the blood cell (Figure 9-5).

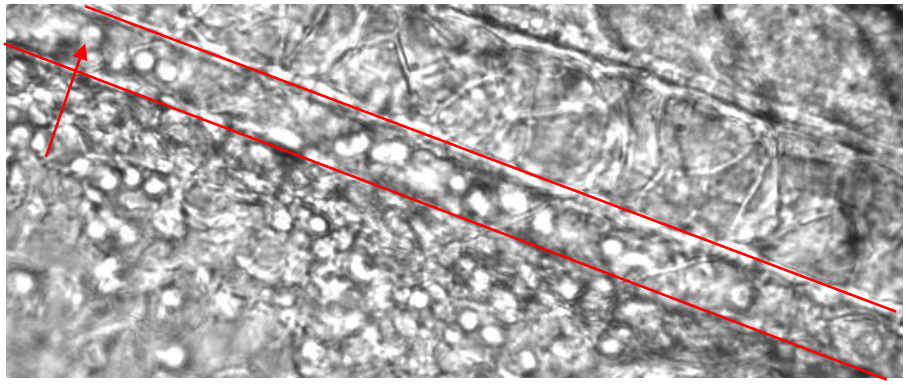

Figure 9-4. Detail of the zebrafish embryo showing blood cells inside the aorta (marked with red lines). Red arrow point to one blood cell with a dimension of 7µm

Figure 9-5. Processed movie frame of Figure 9-4 obtained by subtraction from the next frame and after rescaling and thresholding. The arrows point at the two displacement arches of the marked blood cell in Figure 9-4.

9. 2. 1. b. Background learning

This other basic technique uses a number of frames from the image sequence to create a 3D matrix (2D and time). For a given x,y position all grey values for each time point are stored in a vector. The mode value of this vector represents the grey value that occurred most of the time. Repeating this for all x,y positions of the image frame results in a representation of the background. Theoretically this method will perform best if the background is visible most of the time, in our case if the blood vessel is not entirely filled with cells. We tested this method in a 4 days post fertilization (dpf) embryo (aorta completely filled with blood cells) and results remained satisfactory.

A)

B)

C)

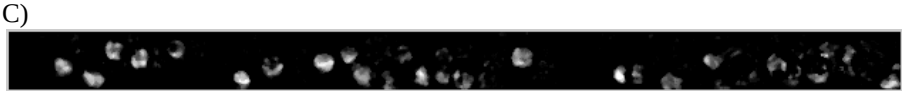

Figure 9-6. Image series showing different steps in background removal. A) standard bright field image of an aorta of a 30hfp zebrafish embryo. B) background reconstructed from background learning of 50 images. C) results of subtracting image A and B after rescaling and median filtering to remove noise.

9. 2. 2. Automatic cell detection and tracking

We used the Hough transform method to detect cells using the background subtraction images as input files. Hough transform is capable of detecting imperfect or incomplete circular gradients (for more background about the working principle we refer to Ballard (1981)). Visual results of the method are displayed in Figure 9-7.

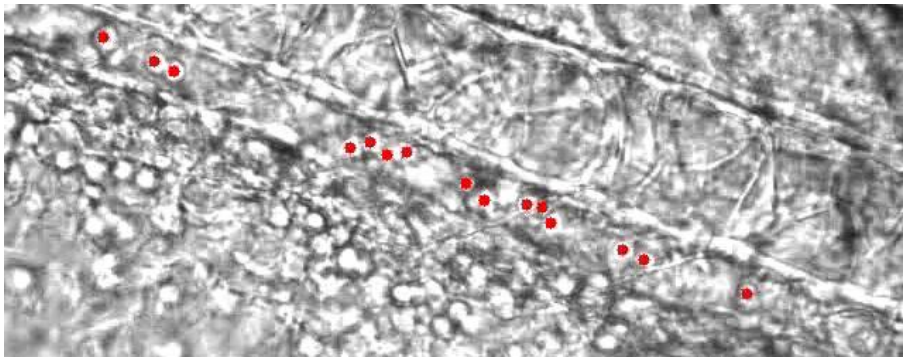

Figure 9-7. Visualisation of the results of the Hough transform using Figure 9-5 as input file.

Applying the Hough transform on an image sequence results in a sequence of blood cell positions. However there is no connection of cell positions between subsequent frames as we don't know which cell went to what position in the next frame. To overcome this we used a simplification of the IDL tracking algorithms developed by Crocker and Grier and modified by Weeks (Crocker and Grier 1996).

The x- and y-values of the circular cell bodies detected in each image were used as input for the tracking procedure. In the first image all detected cells were defined as possessing a center point and a radius equal to a predefined empirical maximal displacement of the cells. In the next image the algorithm looked for possible new locations of cell circles within the circle of maximal displacement of the cells in the previous image. The new location is the one with the smallest distance compared to the considered position in the previous image. Double assignments of a location in the next images were reevaluated by choosing the one with the smallest distance. The discarded one was reassigned to his next smallest distance. Looping this algorithm over the complete dataset produced an array showing a position sequence over time for each particle.

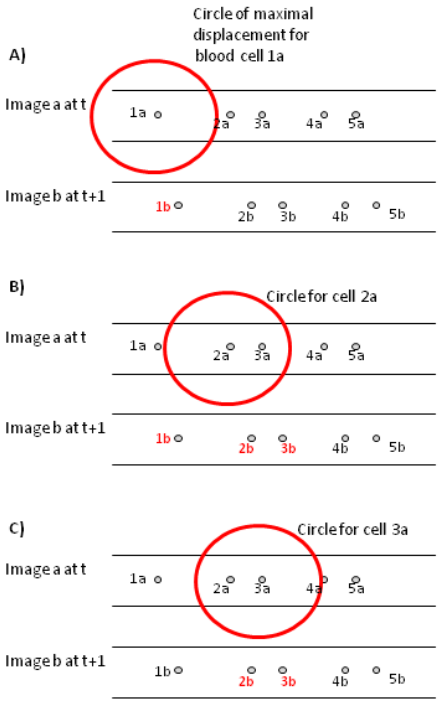

Figure 9-8. Graphical explanation of the applied IDL tracking. Black lines represent vessel wall, small labelled circles represent blood cells. A) circle of maximal displacement marked around blood cell 1 in image a; cells within the marked circle in image b: blood cell 1 (label marked in red). B) blood cells within circle of blood cell 2: 1, 2 and 3 => blood cell 2 is chosen because it has the smallest distance. C) blood cells within circle around blood cell 3: 2 and 3 => blood cell 2 has the smallest distance but is already chosen by the previous blood cell => choose blood cell 3.

First results produced an excess of short tracks, suggesting that some particles were being lost during tracking. This is probably due to the Hough transformation failing to detect cell outlines in some images. Additional code was developed to improve this aspect. Hence, if no new cell location was found in the next image, the subsequent image was analyzed for new cell locations in the same defined circle of maximal displacement. If still no particle was found then the radius of the circle was doubled, since over two image frames the maximal distance possibly traveled by a cell was also doubled. If no particle was found the track of that specific cell was ended. Conversely, the Hough transformation was occasionally found to suggest circles, which were not blood cells. These detections were short lived and easily deleted by defining a minimum number of time steps that a cell should be tracked. The resulting array consists of cell IDs and their positions in subsequent image frames.

This array is then used to calculate individual velocities of the particles. The spatial displacement of each cell was derived by calculating the square root of the squares of the x and y displacements for each blood cell in one time frame. Thus instantaneous velocity is derived. In each frame all instantaneous velocities are averaged to obtain one value for each frame.

9. 2. 3. Micro digital particle Image Velocimetry (µDPIV) based methods

Particle Image Velocimetry (PIV) is an optical technique to measure instantaneous velocities. Tracer particles, illuminated through laser light, are captured by a camera as bright dots. Subsequent images of bright dots are then compared with each other. The images are subdivided in search kernels and, after processing, each kernel results in one velocity vector (Adrian 1991; Grant 1997).

µPIV uses the same techniques but is applied on a microscopic scale. The first report in embryonic heart research using this technique *in vivo* is published by Venneman et al. (2006). Digital PIV (DPIV) on the other hand describes the image processing techniques of PIV images (Willert and Gharib 1991; Westerweel 1997). This has been tested by Forouhar and reported in his PhD thesis (Forouhar 2006). His results show that commercial software is not usable for measuring aortic velocities. The main reason is that images are not acquired on a PIV setup and need preprocessing to match the requirements of PIV images (see § 9. 2. 1.).

We defined our aortic velocity measuring technique as a µDPIV based method since we use the principles of DPIV on a microscopic scale. DPIV is in fact nothing else than trying to map an image or parts of it onto the next image by rigidly moving it in x and y directions in the spatial domain. A similarity measure is defined and

computed for every x,y-displacement. The best match assigned by the similarity measure and its corresponding x,y-position define the displacement of the blood cells.

In the next paragraphs we introduce the different similarity measures that were evaluated.

9. 2. 3. a. Minimization of the sum of absolute differences

Two subsequent frames (*A* and *B*) are subtracted and all pixels of the resulting image are added. The minimal value of all displacement points *x,y* corresponds to the best fit.

$$\min\left(\sum_{i=1}^{m}\sum_{j=1}^{n} abs\left(A_{(m,n)} - B_{(m,n)}\right)\right)_{(x,y)} \qquad 9\text{-}1$$

9. 2. 3. b. 2D Cross correlation.

In commercial software packets used for PIV processing the most common used similarity measure is cross correlation. Is has been proven to be very efficient to work with black and white images (Adrian 1991; Grant 1997).

In our case images have the same dimensions; e.g. dimensions for image *A (Ma, Na)* = dimensions for image *B (Mb, Nb)* the 2D cross correlation is computed as follows

$$C(i,j) = -\sum_{m=1}^{Ma}\sum_{n=1}^{Na} A_{(m,n)} \cdot conj(B_{m+i,n+j}) \qquad 9\text{-}2$$

Where $1 \le i < Ma+Mb$ and $1 \le j < Na+Nb$

The maximal value corresponds to the best fit. Functions in Matlab compute the cross correlation for every point in the image, far beyond the maximal displacement of the blood cells, making this a very time consuming method.

9. 2. 3. c. Mutual information

Mutual information is a technique that has initially been developed for multimodal image registration and is nowadays widely used in medical imaging to match for example CT with MRI images (Zitova and Flusser 2003). It is said to be very robust for blurry images (Maes et al. 2003).

Mutual information is based on joint entropy. This is a measure for dispersion of a 2D joint histogram. This joint histogram has the number of grey scale values (256 in our case) on the x-axis for image 1 and on the y-axis for image 2. It is created by

plotting the grey values of the same pixel location of both images on their respective axis. The entropy *H* is calculated as follows:

$$H(A,B) = -\sum_{a,b} p(a,b) \cdot \log[\, p(a,b)] \qquad 9\text{-}3$$

Where *p(a,b)* is the joint probability distribution function of *A* and *B*

Figure 9-9 Illustration of the joint histogram together with the calculation of the dispersion in the form of entropy (dispersion is increasing from left to right).

Mutual information is an extension of joint entropy by incorporating the initial entropy of the image:

$$I(A,B) = H(A) + H(B) - H(A,B)$$
$$= \sum_{a,b} p(a,b) \cdot \log\left(\frac{p(a,b)}{p(a)\,p(b)} \right) \qquad 9\text{-}4$$

Where *p(a,b)* is the joint probability distribution function of *A* and *B*, and p(a) and *p(b)* are the marginal probability functions of *A* and *B* respectively. This results in a single value for each comparison. From these values the highest peak was selected to be the best match.

We used the scripts written for Matlab by Kateryna Artyushkova (Artyushkova et al. 2010). Although the calculation of the mutual information is slow, the number of calculations can be limited to a window of expected maximal displacement, making this faster than the cross correlation.

9. 2. 4. Post processing of results

9. 2. 4. a. Cyclic averaging of velocity signal

Looping the algorithm over the complete image stack results in a cyclic pattern of velocity waves (Figure 9-10 top).

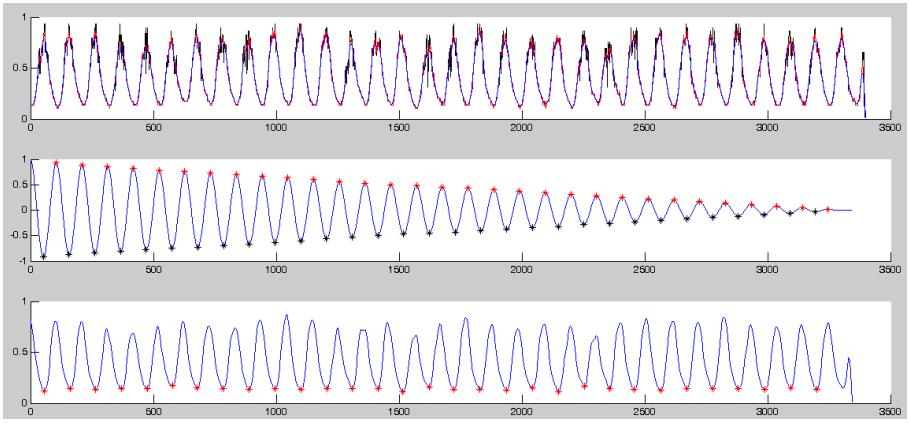

Figure 9-10. Aortic velocity in a 30 hpf zebrafish aorta. Vertical axis is velocity (mm/s) horizontal axis represents time (expressed as frame number). Top graph shows measured velocity (black), smoothed velocity using moving average of 10 samples (blue) and measured velocity with removed spikes when the measured velocity differs more than 10% from the smoothed velocity line (red). Middle graph shows the second half of the autocorrelation function used to assign the minimal values of the velocity curve. Bottom graph shows smoothed velocity with assigned minimal values used to assign the onset of each cycle on the original data.

In order to be able to rapidly compare between studies different developmental stages of embryos or different drug treatments we are interested in a single representative waveform of the aortic velocity. We choose cyclic averaging. This is possible because of the very constant period (also reported by Schwerte et al. (2006). However due to the noise determining the begin and the end of the cycle is not trivial.

Therefore we made use of the autocorrelation derived from the original data since this signal shows similar periodicity but has no noise. The autocorrelation is only used to estimate the cycle period in order to know where to find begin and end of a cycle.

Assigning the start of the cycle based on searching the minimal value in the neighborhood of an autocorrelation minimum still won't work because of noise. Therefore we smooth the original signal using a forward and backward moving average filter. This filtered signal is only used to find the location of the minimal value. This location is then projected on the original signal to assign the start of the cycle.

Averaged values are calculated from the original signal (Figure 9-10, blue curve). Little changes in periodicity are covered by a linear resampling procedure that works as follows. Take for example an average cycle length of 100 frames and one of the cycles has less than 100 frames (e.g. 98). In this case there exist 100 places (the equivalent of the average cycle length) to store a velocity measure so in this case the cycle has two places short. The following places (called bins) will be skipped:

$$skipped = round\left(i \cdot \frac{average\_cyclelength}{places\_short + 1} \right) \qquad 9\text{-}5$$

Where *i* runs from 1 to the number of places short.

In this case bin 33 and bin 67 will be skipped. If one cycle has more than 100 frames (e.g. 101) then in bin 50 two values will be stored. The average velocity wave is reconstructed from averaging the values in each of the bins.

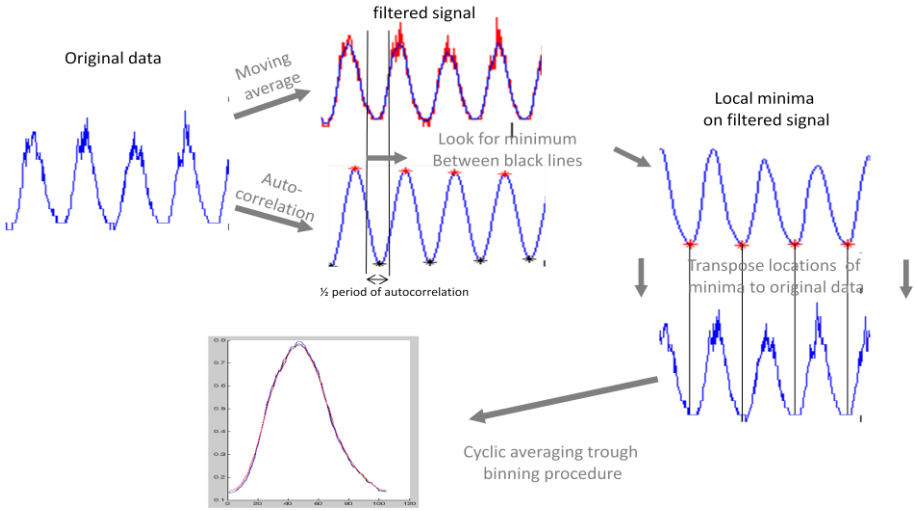

Figure 9-11. Flow chart explaining the procedure used for cyclic averaging of the original signal

9. 2. 4. b. Parameters derived from the aortic velocity

Flow rate is computed from the multiplication of the instantaneous blood velocity in the dorsal aorta with the area of the aorta at the same location under the assumption of a cylindrical aorta.

$$Flow\ rate\ \left[\frac{nl}{s}\right] = velocity\left[\frac{mm}{s}\right] * \pi * \frac{diameter[mm]^2}{4} * 1000 \qquad 9\text{-}6$$

Cardiac output is computed as follows:

$$Cardiac\ output\ \left[\frac{nl}{s}\right] = average\ velocity\left[\frac{mm}{s}\right] * \pi * \frac{diameter[mm]^2}{4} * 1000 \qquad 9\text{-}7$$

Where average velocity is the average velocity during one cycle.

Stroke volume is derived from the cardiac output:

$$Stroke\ volume\ \left[\frac{nl}{beat}\right] = \frac{cardiac\ output\ \left[\frac{nl}{s}\right]}{heart\ rate\ \left[\frac{beats}{s}\right]} \qquad 9\text{-}8$$

9. 3. RESULTS AND DISCUSSION

9. 3. 1. Definition of evaluation parameters

9. 3. 1. a. Definition of accuracy

To be able to evaluate the results of our developed method we created a ground truth by manually tracking every blood cell in the aorta over the entire frame width in 1000 image frames of a 30 hpf zebrafish embryo. The accuracy of the method is defined as the deviation from the ground truth. It is quantified trough linear regression of a joint histogram. In the example of Figure 9-12 a less accurate method 2 (compared to method 1 = ground truth) will result in a increased deviation from the regression line and in a lower R^2. For the interpretation of where methods deviate we will use Bland Altman plots (Altman and Bland 1983; Bland and Altman 1986) also called Tukey difference plots.

label	method1	method2
1	10	12
2	13	13
3	15	16
4	17	19
5	22	21
6	19	18
7	15	13
8	11	9
9	6	7
10	2	1

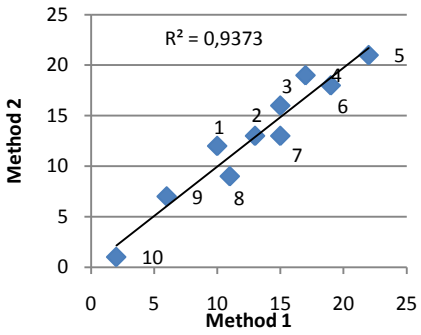

Figure 9-12 Illustration of the applied definition of accurateness using the R^2 of the linear regression of the joint histogram.

9. 3. 1. b. Definition of robustness

Robustness is the ability of finding the same results under different conditions. In our situation the measured velocity shows a cyclic behavior. We therefore defined robustness as the ability of obtaining the same velocity at a given time point of the cardiac cycle and this in every cycle. This particular time point is calculated from different cycles thus from different image pairs with different cell distributions. The higher the chance of finding the same velocity, the higher the robustness.

In our case every time point in the cardiac cycle is calculated as an averaged time point from using all cycles. An easy estimate for robustness in our samples is the standard deviation from the averaged value.

9. 3. 2. Evaluation of the developed methods for aortic velocity estimation.

9. 3. 2. a. Accuracy of the developed methods

The accuracy of the evaluated methods is displayed in Figure 9-13. Since the linescan method developed by Malone et al. (2007) is considered a reference method we applied it on our data and incorporated the results in the evaluation.

Qualitatively we see that all methods are capable of capturing the cyclic behaviour of the blood velocity in the zebrafish aorta. However, at higher velocities the automated cell detection and tracking method tend to fail. The linescan method is less accurate at higher velocities (more dispersion in the joint histogram and in the Bland Altman plot). The µDPIV based methods appear to outperform the other methods. Between those the mutual information similarity measure shows remarkable results since this method is the only method able to capture anomalies (spikes in the manual tracking) correctly.

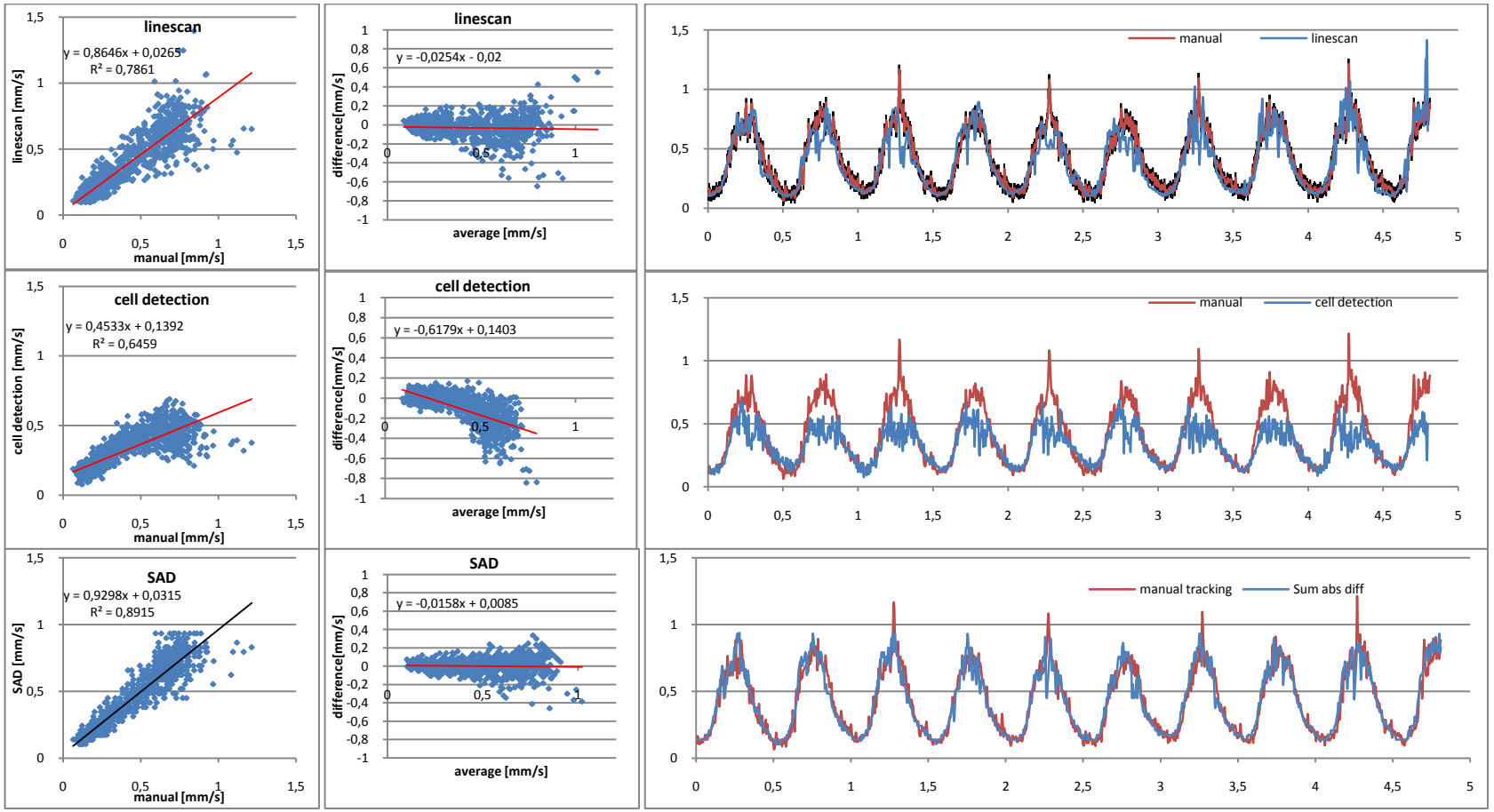
linescan
y = 0,8646x + 0,0265
R² = 0,7861
linescan [mm/s]
manual [mm/s]
linescan
y = -0,0254x - 0,02
difference[mm/s]
average [mm/s]
manual
linescan
cell detection
y = 0,4533x + 0,1392
R² = 0,6459
cell detection [mm/s]
manual [mm/s]
cell detection
y = -0,6179x + 0,1403
difference[mm/s]
average [mm/s]
manual
cell detection
SAD
y = 0,9298x + 0,0315
R² = 0,8915
SAD [mm/s]
manual [mm/s]
SAD
y = -0,0158x + 0,0085
difference[mm/s]
average [mm/s]
manual tracking
Sum abs diff

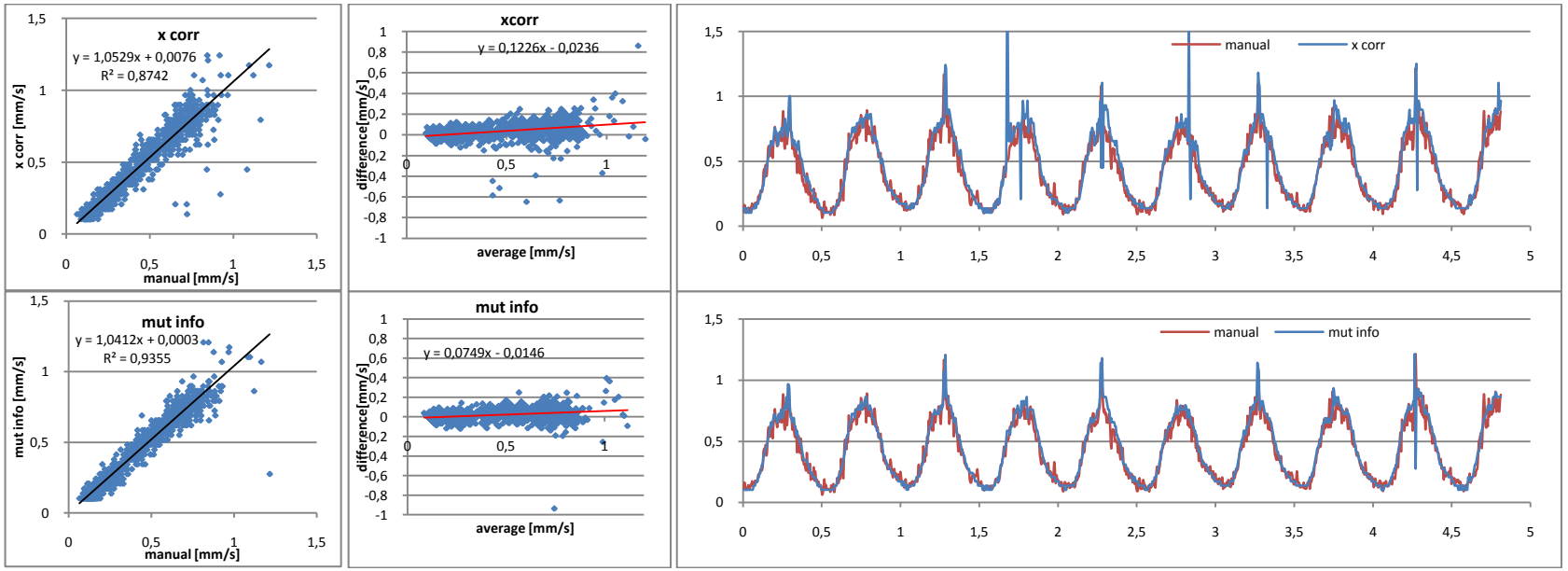

Figure 9-13. Evaluation of velocity measures compared to manual tracking (= ground truth). From top to bottom: linescan, automatic cell detection and tracking, µDPIV with sum of absolute differences, µDPIV with cross correlation, µDPIV with mutual information. Left: Quantitative joint histograms, middle Bland Altman plot, right: comparison graph (velocity [mm/s] over time [s]). All methods are tested on the same data set of 1000 frames imaged from an aorta of a 30 hpf zebrafish embryo.

9. 3. 2. b. Evaluation of robustness

All measures show higher standard deviations for higher velocities. This is mainly due to the fact that images tend to blur at higher velocities. Linescan shows to be the less robust as the standard deviation is twice as high compared to the other methods. This means that at higher velocities the method is more subjected to noise. The cell detection method, despite being incorrect at higher velocities, is more consistent.

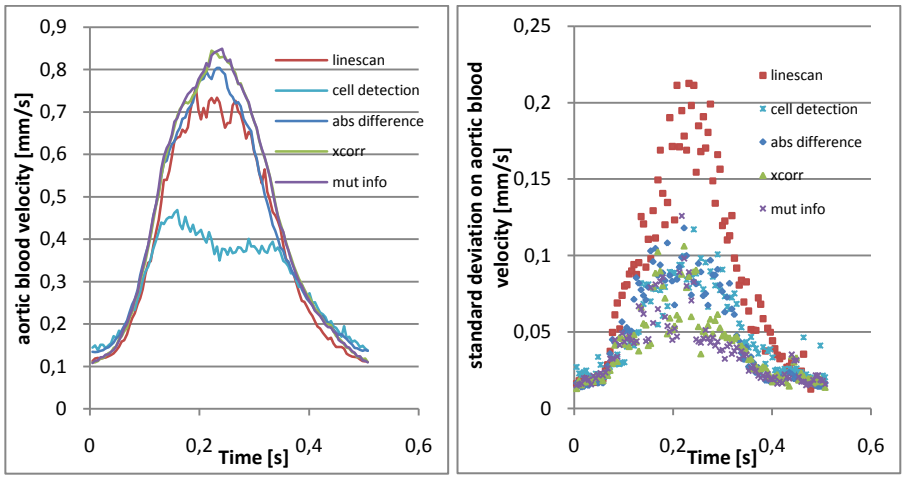

Figure 9-14. Left: graph showing the results of aortic velocity measurements using five different methodologies. Projected lines are the result of averaging 30 cycles. Right: standard deviation of the mean values plotted left. (both images have the same legend to facilitate comparison). The standard deviation can be interpreted as a relative robustness measure between the different methodologies.

9. 3. 2. c. Explanation for the failure of the cell detection method

The severe underestimating of the high velocities is most likely caused by the tracking algorithm, although the settings were applied correctly. As described in § 9. 2. 2. the tracking algorithm is not considering displacement of groups of cells but is only comparing two sets of blood cell locations. At higher velocities it often occurs that cells cross the positions of others cells in the previous frame causing mismatches in the tracking algorithm. Figure 9-15 displays a realistic setting where mismatches are very likely to yield a lower velocity. The averaged value of the red arrows in Figure 9-15D results in a much lower value than the actual velocity (black arrow).

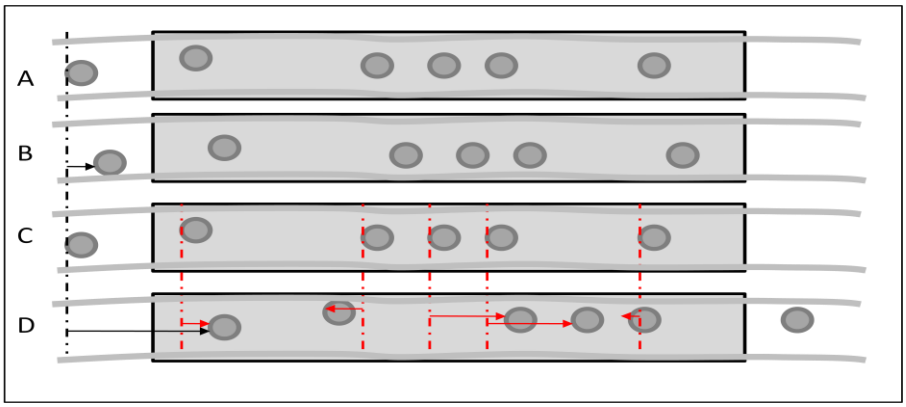

Figure 9-15: Illustration showing mismatches in the tracking algorithm when blood velocities become too high. Curved grey lines represent the vessel wall, circles are blood cells, black box represents an image to be processed, dashed line represents the displacement reference. A and B: small displacements cause reliable results. C an D: higher displacements cause the tracking program to fail (red arrows) compared to the correct displacement (black arrow).

The abundance of mismatches is dependent not only on the displacement but also on the number of cells present in the aorta. As the number of cells increase the number of possible tracks increase. With increasing number of tracks increases the possibility that a cells crosses the previous location of another cell. This method is therefore not applicable for estimating blood velocities in zebrafish embryos.

9. 3. 2. d. Explanation for the failure of the linescan method

The linescan method shows a much higher standard deviation compared to the other methods. This effect is most pronounced at the higher velocities. Beside the fact the images tend to blur at higher velocities there is also an additional cause. If velocities are higher, then the slope of the lines in the linescan increases. Since lines are drawn manually an error of one pixel on the time axis has greater influence when slopes are steep. At maximal velocities displacements are close to 10 pixels per frame. With a scanning line of 40 pixels this comes to 4 pixels in temporal dimension (x-axis), an error of one pixel yields a 25% error (close to the maximal values in Figure 9-14).

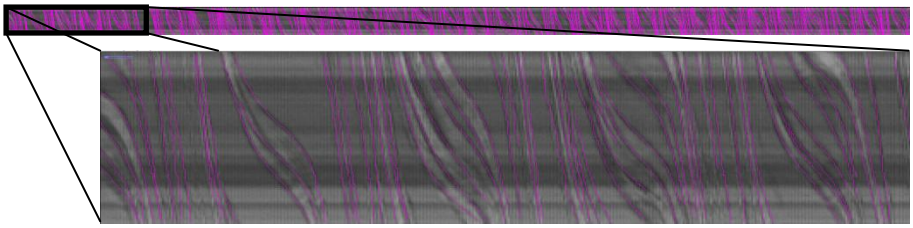

Figure 9-16. Lines drawn on the linescan of Figure 9-3 with the NeuronJ plugin of ImageJ. Horizontal axis represents time vertical axis represents space.

9. 3. 3. Method evaluation summary

We listed the main characteristics in Table 9-1.

Table 9-1 Main characteristics of linescan method, automatic cell detection and tracking method and µDPIV based methods compared to manual tracking, defined as ground truth. Test situation is aortic velocity measurement in a 30 hpf zebrafish embryo.

Method	Automated?	Time to process 3500 frames	Accuracy : R^2 of linear regression of joint histogram	Robustness: averaged standard deviation	Approximate deviation from manual tracking
Manual tracking	No	60 hours	/	/	/
Linescan	No	5 hours	0.78	0.112	- 3 %
Cell detec	Yes	2 hours	0.65	0.050	- 50 %
Abs diff	Yes	8 min	0.89	0.051	-1 %
Cross corr	Yes	1.5 hours	0.87	0.040	+ 10 %
Mut info	Yes	12 min	0.95	0.038	+ 6 %

From the qualitative comparison in Table 9-1 we can conclude that µDPIV methodologies outperform the other methods. Choosing which similarity measure of the µDPIV methods performs best is not straightforward.

In literature a lot of comparative studies have been conducted to evaluate the performance between similarity measures. Often results are contradictory. Penny et al. (1998) showed that mutual information failed to register medical images compared to cross correlation whereas Maes et. al. repeatedly demonstrated the superior accuracy and robustness of different mutual information similarity measures (Maes et al. 1997; Maes et al. 2003). This discrepancy is probably a direct consequence of the kind of images to be registered. To the author's knowledge there is no existence of studies comparing similarity measures for bright field images of zebrafish aortas.

In general cross correlation is used in unimodal images (all images are acquired with the same technique) whereas mutual information is used in multimodal images (images acquired with different techniques).

Wherever possible we used mutual information because it is fast, accurate, and is able to deal with brightness differences between images often occurring in our samples. However, our extensive tests showed that when embryos are very young, velocities are low and very few cells are present, mutual information fails because it is not able to detect displacements. The sum of absolute difference similarity measure in combination with background subtraction is capable of detecting very low velocities (order of 1 pixel/frame) and very high velocities (up to 50 pixels/frame). However, this method is slightly less accurate.

9. 4. CONCLUSIONS

We developed a µDPIV based method for estimating aortic velocities in zebrafish embryo. The method proved to be better than the current methodologies given its:

- shorter processing time
- higher accuracy
- higher robustness

The choice which estimator performs best depends on the images and the expected blood velocity magnitude. Mutual information is proven to be the most accurate but tests have shown that the sum of absolute differences estimator is able to detect a broader velocity range.

9. 5. REFERENCES

Adrian, R. J. (1991). "PARTICLE-IMAGING TECHNIQUES FOR EXPERIMENTAL FLUID-MECHANICS." Annual Review of Fluid Mechanics **23**: 261-304.

Altman, D. G. and J. M. Bland (1983). "MEASUREMENT IN MEDICINE - THE ANALYSIS OF METHOD COMPARISON STUDIES." Statistician **32**(3): 307-317.

Artyushkova, K., A. L. Garcia and G. P. Lopez (2010). "Detecting molecular separation in nano-fluidic channels through velocity analysis of temporal image sequences by multivariate curve resolution." Microfluidics and Nanofluidics **9**(2-3): 447-459.

Bagatto, B. (2005). "Ontogeny of cardiovascular control in zebrafish (Danio rerio): Effects of developmental environment." Comparative Biochemistry and Physiology a-Molecular & Integrative Physiology **141**(4): 391-400.

Ballard, D. H. (1981). "GENERALIZING THE HOUGH TRANSFORM TO DETECT ARBITRARY SHAPES." Pattern Recognition **13**(2): 111-122.

Bland, J. M. and D. G. Altman (1986). "STATISTICAL-METHODS FOR ASSESSING AGREEMENT BETWEEN 2 METHODS OF CLINICAL MEASUREMENT." Lancet **1**(8476): 307-310.

Burggren, W. and R. Fritsche (1995). "CARDIOVASCULAR MEASUREMENTS IN ANIMALS IN THE MILLIGRAM RANGE." Brazilian Journal of Medical and Biological Research **28**(11-12): 1291-1305.

Burggren, W. W. (2004). "What is the purpose of the embryonic heart beat? or how facts can ultimately prevail over physiological dogma." Physiological and Biochemical Zoology **77**(3): 333-345.

Chan, P. K., C. C. Lin and S. H. Cheng (2009). "Noninvasive technique for measurement of heartbeat regularity in zebrafish (Danio rerio) embryos." Bmc Biotechnology **9**.

Crocker, J. C. and D. G. Grier (1996). "Methods of digital video microscopy for colloidal studies." Journal of Colloid and Interface Science **179**(1): 298-310.

Davis, A., J. Izatt and F. Rothenerg (2009). "Quantitative Measurement of Blood Flow Dynamics in Embryonic Vasculature Using Spectral Doppler

Velocimetry." Anatomical Record-Advances in Integrative Anatomy and Evolutionary Biology **292**(3): 311-319.

Davis, A. M., F. G. Rothenberg, N. Shepherd and J. A. Izatt (2008). "In vivo spectral domain optical coherence tomography volumetric imaging and spectral Doppler velocimetry of early stage embryonic chicken heart development." Journal of the Optical Society of America a-Optics Image Science and Vision **25**(12): 3134-3143.

Forouhar, A. S. (2006). Dynamic Views of Strucure and Function During Heart Morphogenesis. California Institute of Technology. Pasadena. **Doctor of Phylosophy:** 147.

Forouhar, A. S., M. Liebling, A. Hickerson, A. Nasiraei-Moghaddam, H. J. Tsai, J. R. Hove, S. E. Fraser, M. E. Dickinson and M. Gharib (2006). "The embryonic vertebrate heart tube is a dynamic suction pump." Science **312**(5774): 751-753.

Fritsche, R. and W. Burggren (1996). "Development of cardiovascular responses to hypoxia in larvae of the frog Xenopus laevis." American Journal of Physiology-Regulatory Integrative and Comparative Physiology **271**(4): R912-R917.

Grant, I. (1997). "Particle image velocimetry: A review." Proceedings of the Institution of Mechanical Engineers Part C-Journal of Mechanical Engineering Science **211**(1): 55-76.

Hou, P. C. L. and W. W. Burggren (1995). "BLOOD PRESSURES AND HEART-RATE DURING LARVAL DEVELOPMENT IN THE ANURAN AMPHIBIAN XENOPUS-LAEVIS." American Journal of Physiology-Regulatory Integrative and Comparative Physiology **269**(5): R1120-R1125.

Iftimia, N. V., D. X. Hammer, R. D. Ferguson, M. Mujat, D. Vu and A. A. Ferrante (2008). "Dual-beam Fourier domain optical Doppler tomography of zebrafish." Optics Express **16**(18): 13624-13636.

Isogai, S., M. Horiguchi and B. M. Weinstein (2001). "The vascular anatomy of the developing zebrafish: An atlas of embryonic and early larval development." Developmental Biology **230**(2): 278-301.

Maes, F., A. Collignon, D. Vandermeulen, G. Marchal and P. Suetens (1997). "Multimodality image registration by maximization of mutual information." Ieee Transactions on Medical Imaging **16**(2): 187-198.

Maes, F., D. Vandermeulen and P. Suetens (2003). "Medical image registration using mutual information." Proceedings of the Ieee **91**(10): 1699-1722.

Malone, M. H., N. Sciaky, L. Stalheim, K. M. Hahn, E. Linney and G. L. Johnson (2007). "Laser-scanning velocimetry: A confocal microscopy method for quantitative measurement of cardiovascular performance in zebrafish embryos and larvae." Bmc Biotechnology **7**: 11.

Mirkovic, T. and P. Rombough (1998). "The effect of body mass and temperature on the heart rate, stroke volume, and cardiac output of larvae of the rainbow trout, Oncorhynchus mykiss." Physiological Zoology **71**(2): 191-197.

Penney, G. P., J. Weese, J. A. Little, P. Desmedt, D. L. G. Hill and D. J. Hawkes (1998). "A comparison of similarity measures for use in 2-D-3-D medical image registration." Ieee Transactions on Medical Imaging **17**(4): 586-595.

Schwerte, T. and R. Fritsche (2003). "Understanding cardiovascular physiology in zebrafish and Xenopus larvae: the use of microtechniques." Comparative Biochemistry and Physiology a-Molecular & Integrative Physiology **135**(1): 131-145.

Schwerte, T. and B. Pelster (2000). "Digital motion analysis as a tool for analysing the shape and performance of the circulatory system in transparent animals." Journal of Experimental Biology **203**(11): 1659-1669.

Schwerte, T., C. Prem, A. Mairosl and B. Pelster (2006). "Development of the sympatho-vagal balance in the cardiovascular system in zebrafish (Danio rerio) characterized by power spectrum and classical signal analysis." Journal of Experimental Biology **209**(6): 1093-1100.

Vennemann, P., K. T. Kiger, R. Lindken, B. C. W. Groenendijk, S. Stekelenburg-de Vos, T. L. M. ten Hagen, N. T. C. Ursem, R. E. Poelmann, J. Westerweel and B. P. Hierck (2006). "In vivo micro particle image velocimetry measurements of blood-plasma in the embryonic avian heart." Journal of Biomechanics **39**(7): 1191-1200.

Vlachopoulos, C. and M. O'Rourke (2000). "Genesis of the normal and abnormal arterial pulse." Current Problems in Cardiology **25**(5): 301-367.

Westerweel, J. (1997). "Fundamentals of digital particle image velocimetry." Measurement Science & Technology **8**(12): 1379-1392.

Willert, C. E. and M. Gharib (1991). "DIGITAL PARTICLE IMAGE VELOCIMETRY." Experiments in Fluids **10**(4): 181-193.

Zitova, B. and J. Flusser (2003). "Image registration methods: a survey." Image and Vision Computing **21**(11): 977-1000.

Chapter 10 INFLUENCE OF AGE AND DRUG DOSE ON AORTIC BLOOD FLOW IN ZEBRAFISH EMBRYOS

In this chapter we apply the methods evaluated in the previous chapter to investigate the blood flow changes during development and blood flow changes due to a drug that affects heart muscle response. Use of the cyclic averaged velocity wave will enable us to derive parameters that can be related to the pumping performance of the heart.

10. 1. INTRODUCTION

Throughout development the heart changes drastically. In zebrafish the first contractions start at 22 hpf. Chi et al. (2008) demonstrated a coordinative electric signal is present at 24 hpf so probably net flow is established by then. Blood cells start appearing from 24 hpf onwards (Thisse and Zon 2002). However the number of blood cells in the investigated embryos varied a lot, from very few to abundant, when filmed at 28hpf. From 32 hpf the heart starts looping and at 48 hpf the cushions start to form, initiating chamber formation. From the first beat on the heart needs to maintain function and needs to meet the ever growing nutrient and oxygen demand. The aim of this chapter is to use the µDPIV based methods described in the previous chapter to investigate how aortic flow changes during development of the heart and to investigate the influence of a drug that affects heart muscle response.

10. 2. MATERIALS AND METHODS

10. 2. 1. Embryo preparation and data acquisition

Zebrafish (*Danio rerio*) embryos were collected immediately after fertilization and allowed to develop normally at 28.5 °C. Prior to imaging, the chorion (egg case) was removed from the embryos and they were lightly anaesthetized in 0.05% tricaine to prevent movement during data acquisition.

Images were acquired using an inverted transmission light microscope (Nikon) equipped with a high-speed digital image recording system (Multipix, UK). The images were taken at 207 frames per second (480 x 640 pixels) and use of 20X and 40X objective lenses allowed tracking individual red blood cells.

10. 2. 2. Aortic flow changes during development

We investigated embryos from wildtype zebrafish (AB) and from semitransparent zebrafish (Golden). Embryos are imaged from 28 to 34 hpf. However due to circumstances not every embryo is measured every hour (a list is number of

embryos for each hour is given in Table 10-1). Since images were of low quality and blood velocities are typically very low at 28 hours, all images were processed using the µDPIV method with sum of absolute differences and background subtraction. 2000 images were used for the calculation of the cyclic average.

Several hundreds of embryos were imaged but very few datasets were useful for comparative investigation. This is mainly due to the rapid development of the embryos. This means that embryos have to be imaged within a timeframe of approximately 10 minutes around the hour of imaging otherwise blood velocities might differ considerably. To reduce natural variability we used embryos from only two or three clutches and imaged them every 2 hours. Due to multiple handlings that need to performed with extreme care and precision very often embryos get damaged causing unwanted side effects on flow patterns. A list of numbers of embryos is given in Table 10-1.

Table 10-1 number of embryos per age group

Age[hpf]	28	30	32	34	Total number of embryos
Number of AB	2	6	6	6	6
Number of Golden	3	3	4	4	5

10. 2. 3. Drug tests

2,3-butanedione monoxime (BDM) is a drug which suppresses the excitation-contraction coupling in the heart (Takasago et al. 1997). Tests are done on Golden embryos. To reduce natural variability we did paired tests on the same embryo. First images are taken as a control embryo, then the embryo is removed from the microscope and a dose of BDM is added to the swimming water. After 5 minutes the embryo is remounted and images are taken from the treated embryo.

For the evaluation of the effects of low doses BDM on the aortic flow we used the µDPIV method with mutual information and background learning. Calculations are based on 3500 images for each embryo.

For detailed description of the velocity estimation methods and parameter calculation we refer to chapter 9.

10. 3. RESULTS AND DISCUSSION OF THE INFLUENCE OF AGE

10. 3. 1. Influence of age on heart rate

The zebrafish hearts starts beating at 22 hpf (Stainier and Fishman 1994). Results of heart rates counted in AB and Golden embryos while they were still in the egg case

are presented in Figure 10-1. To allow comparison we plotted heart rates derived from the aortic velocity measurements in parallel.

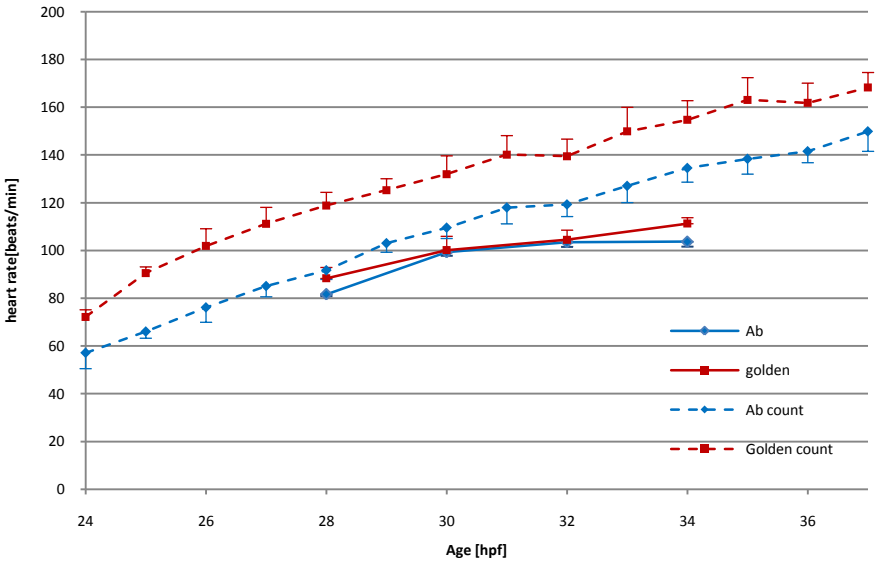

Figure 10-1 Changes of heart rate with age. Dotted lines are from heart rates counted in embryos while still in the egg case. Continues lines are heart rates calculated from aortic blood velocity measurements. Heart counts and velocity measurements are performed in different embryos. Error bars represent standard error (for number of embryos for each age group we refer to Table 10-1).

Figure 10-1 displays an increase of heart rate during development. According to Hu and Clark (1989) this is the result of an increasing demand for nutrients. AB embryos tend to have lower heart rates compared to Golden embryos. For AB and Golden the heart rates derived from aortic blood velocity measurements are significantly lower than the counted hearts. This discrepancy might be caused by dechorionating and the mounting of embryos on a stage for the velocity measurements whereas counts are done when embryos are still in the egg case. For the velocity measurements embryos are subsequently mounted and unmounted every time measurements take place. The influence of this is noticeable by the decreasing slope of these heart rates. Initially the slope is parallel to the slope of the heart rate counts but from 32 hpf on the slope starts decreasing and deviates more and more from the line of the heart rate counts. This must be caused by general weakening of the embryo since embryo hearts are not able to respond to adregenic stress before 4 dpf (Schwerte et al. 2006).

Interesting is the plateau occurring between 31 and 32 hpf where the heart rate remains constant for one hour. The heart is currently in the looping stage (from 30 hpf until 36 hpf). Why this plateau occurs remains unclear.

10. 3. 2. Influence of age on aortic blood flow

Results of one AB and one Golden embryo are plotted in Figure 10-2.

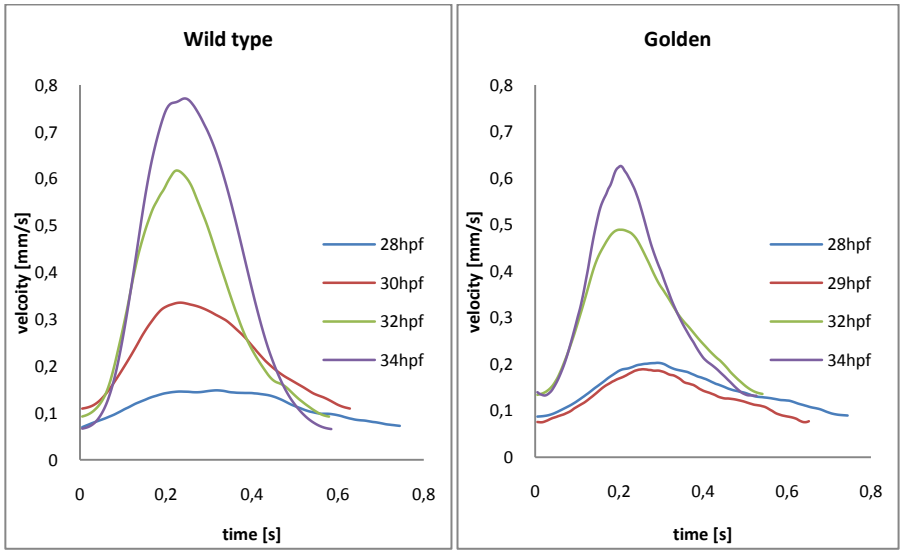

Figure 10-2. Plots of averaged aortic velocity estimated with µDPIV using background subtraction and sum of absolute difference as similarity measure. Left: AB embryo, Right: Golden embryo. Results are smoothed with a moving average filter of 1/10 of the cycle length.

Figure 10-2 shows that maximal velocity increases by up to five times in 6 hours while the cycle period decreases with approximately 25% (increasing heart rate). Also noticeable is the non zero minimal velocity caused by a compliant vessel wall.

Malone et al. (2007), making use of laserscanning velocimetry at the same location on the dorsal aorta as we did, report velocities in the order of 0.7 mm/s of embryos of one day. However, in comparison to measurements made in older fish, their data in young embryos demonstrated significant levels of noise. Their reported cardiac output is of 5 nl/min in zebrafish of one day compared to 5 nl/min measured with our methodology at 28 hpf. However they report to have trouble measuring the aortic diameter.

To our knowledge however there are no other results of aortic flow in zebrafish embryos prior to valve formation reported in literature. The Cardiac outputs mentioned are in keeping with those reported in literature for older embryos after valve formation (Bagatto and Burggren 2006; Kopp et al. 2007). Their cardiac output estimates are based on approximating volume changes of the ventricle.

Figure 10-2 also reveals that the shape of the velocity curve changes when the embryo gets older. This is of importance because it can give insight in cardiac performance of the embryonic heart during development. In Table 10-2 we listed some important parameters and their link to cardiovascular function.

Table 10-2 Measured quantities, their physiological correlates and diagnostic utility (reproduced from Malone et al. 2007)

Physical measurement	**Physiological Parameter**	**Diagnostic relevance**
Peak velocity	Peak velocity	↑ in aortic stenosis, ↓ in heart failure
Minimum velocity	Minimum velocity	Negative with valvular dysfunction
Peak acceleration	Contractility	↓ in heart failure
Peak deceleration	Peripheral resistance	Indicative of vascular tone and development
Velocity integral	Stroke volume and cardiac output	↓ in heart failure

10. 3. 2. a. Velocity characteristics

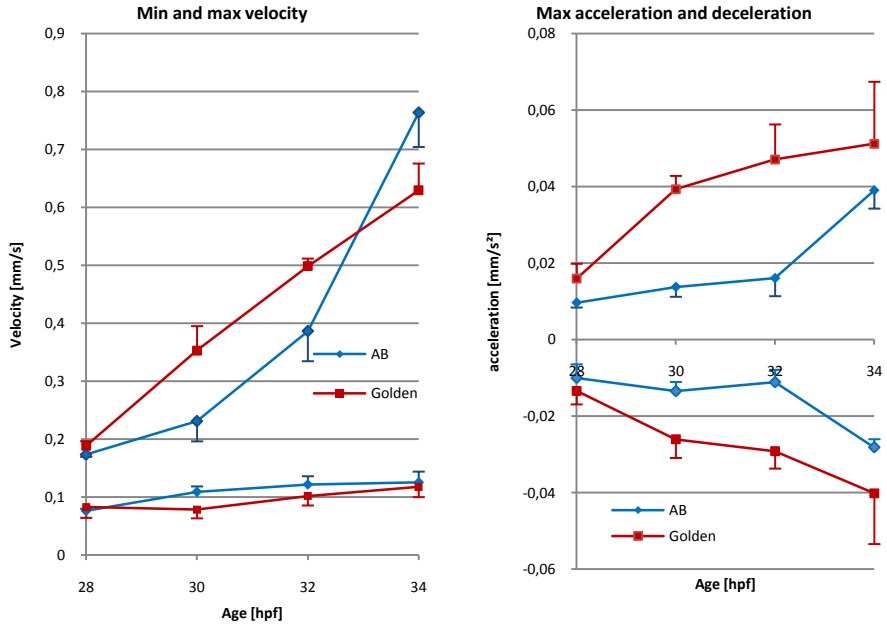

Figure 10-3 Visualization of velocity and acceleration in zebrafish embryos (wild type (AB) and Golden). Dots represent averaged values. All values are obtained from smoothed cyclic averages in order to calculate representative derivatives. Error bars represent standard error.

Peak velocity increases dramatically with age. Combined with an increase of peak acceleration this is a reflection of an increasing heart contractility. However differences exist between both embryo types. Golden embryos show a much higher peak acceleration and deceleration which is the reflection of a more narrow velocity curve.

Also minimal velocity increases implying a better functioning valve. Image sequence of the heart (chapter 2) reveal that some backflow is present in the embryonic heart at early stage. This could be seen as an improper valve functioning since occlusion of the contraction is incomplete. The fact that minimal velocity increases could imply that contraction of the heart gets stronger with age resulting in a better occlusion. The effect, however, is dampened because of the compliance of the vessel wall.

The increasing deceleration indicates increasing peripheral resistance which is probably a reflection of the ongoing angiogenesis since the arterial tree is still in full development. This will result in a need for continuously higher pressure generation. Eventually the valveless heart structure won't be able to fulfil this requirement anymore and will develop into a chambered heart (for modelling of this transition see Taber et al. (2007)).

Interestingly, the increase of acceleration is higher than the increase of maximal deceleration which suggests a change in shape of the velocity curve.

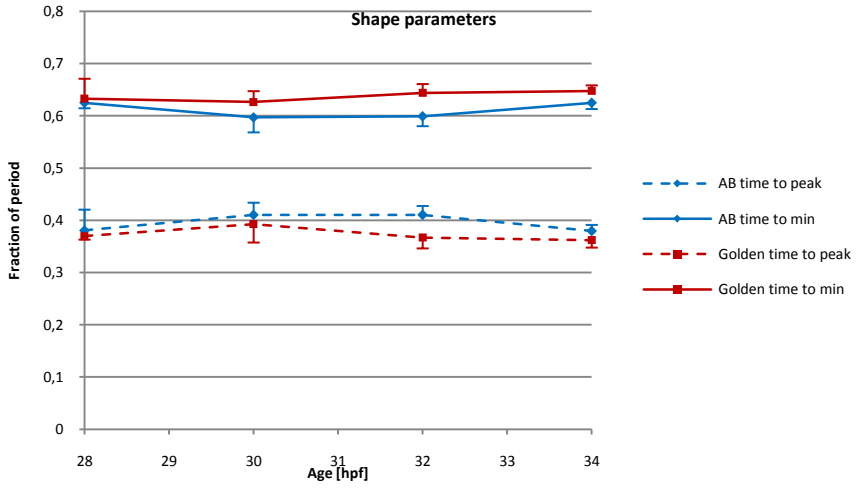

Figure 10-4. Shape parameters of the velocity curve. Time to peak and time to minimum plotted for wild type (AB) and Golden. Values are normalized with period to avoid influence of heart rate. Error bars represent standard error.

Figure 10-4 demonstrates that the velocity curve is asymmetric since the time to reach the maximum is only 40% of the heart cycle. This asymmetry could imply that the speed of the occlusion along the heart wall is not constant but has a decreasing

trend towards the outlet. This is keeping with the finding of Jenkins et al. (2007) who demonstrated that the wave speed in avian hearts is four times faster in the inlet region compared to the outlet. Although the speed difference is not that pronounced in zebrafish hearts we can notice the same phenomenon in the cardiac condition system measured by Chi et al. (2008). Their results show a higher speed of the conduction signal in the first half of the heart.

Accordingly Figure 10-4 shows that from 30 hpf, when velocity starts increasing, the time to peak velocity tends to shorten. This could be a reflection of a developing heart. Chi et al. (2008) demonstrated that in tubular heart stage the propagation of the calcium signal is continuous. When compartmenting of the heart starts the calcium signal shows an increased speed in atrial section of the heart, is delayed before the ventricle and proceeds with increased speed in the first part of the ventricular section Figure 10-5.

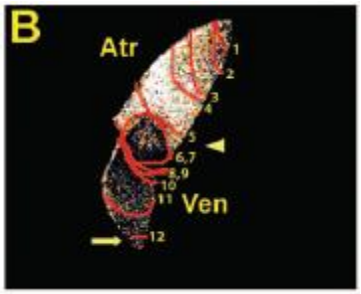

Figure 10-5 Isochrones of calcium signal in a 48 hpf zebrafish embryo. A delay is visible between atrium and ventricle. Atr: atrium, Ven: ventricle [from (Chi et al. 2008)].

Thus the shortening of the time to reach the maximal velocity in the tubular stage might be an onset to chamber pumping which is established at 48hpf in zebrafish.

10. 3. 2. b. Flow characteristics

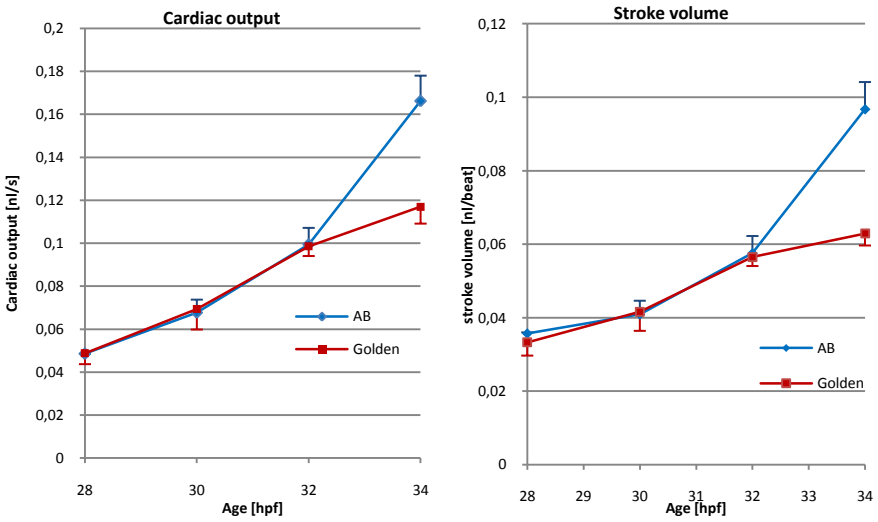

Figure 10-6 Cardiac output and stroke volume for AB and Golden zebrafish embryos. Error bars represent standard error.

The cardiac output increases with age as displayed in Figure 10-6. Golden hearts have a higher heart rate compared to AB hearts but they have lower cardiac output in older embryos.

Stroke volume increases rapidly from the age of 30 hpf. This is not a coincidence since from that time on the heart starts looping (Stainier and Fishman 1994). This time instant corresponds to the onset of heart volume increase resulting in increasing stroke volume.

It is remarkable that form 28 hpf until 32 hpf the cardiac output and the stroke volume is almost the same in both species despite the difference in heart rate, maximal velocity and peak acceleration of both embryos. The Golden embryos are characterized by a more narrow velocity curve combined with higher velocity and heart rate. The AB embryos are characterized by a broader velocity curve in combination with a lower heart rate and a lower velocity. At approximately 33 hpf the maximal velocity of the AB surpasses the maximal velocity of the Golden resulting in a higher cardiac output and stroke volume. The reason for the Golden embryos to have a lower stroke volume could be a weaker heart since morphologically the hearts of AB and Golden are perfectly alike.

10. 4. Results and discussion of BDM drug testing

In order to understand how the embryonic heart functions we used low doses of 2,3 butanedione monoxime (BDM), which suppresses the excitation-contraction

coupling in the heart (Takasago et al. 1997). This negative inotropic (force reducing) drug is clinically used for reversible cardioplegia (to arrest the heart) (Jayawant et al. 1999). It is reported to reduce the number of muscular force generating cross bridges and is assumed to reduce the force generation per cross bridge (Brixius and Schwinger 2000). A dose related study reports that force decreased by 10-82% over a dose range of 1-20 mM of BDM and no response was observed from 30mM on (Perreault et al. 1992). For more information on the working principle of BDM on mammalian myocardium we refer to Gwathmey et al. (1991).

The effect on embryonic zebrafish hearts is evaluated by analysis of flow velocity patterns in the aorta. Results are displayed in Figure 10-7.

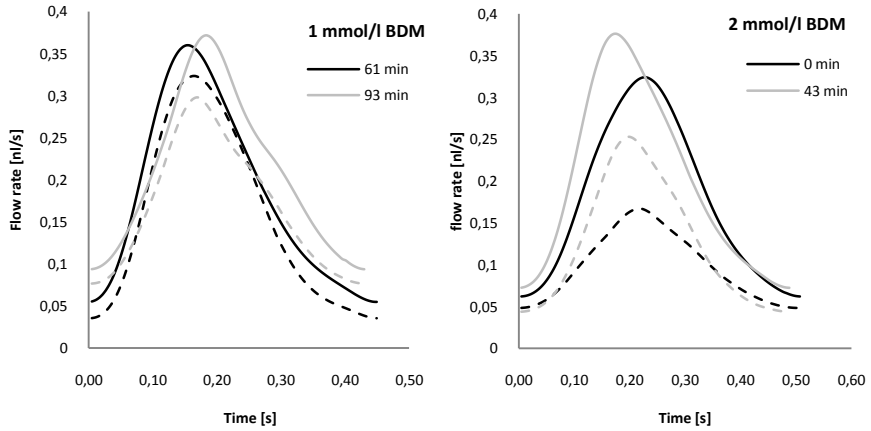

Figure 10-7. Overview of the flow rate in time plotted for the different doses of BDM. Solid line is the flow of the control, dashed line is the flow in the same embryo but treated with a dose of BDM. Lines of the same grey value are measured in the same embryo. Age of embryo is expressed in minutes starting from an embryo of 30 hpf.

The period of the heart cycle is not affected by BDM. This is also reported by Malone et al. (2007). Making use of tricaine to influence aortic velocities they showed that heart rate was independent of the tricaine dose. Schwerte et al. (2006) investigated heart rate variability through power spectrum analysis and found that the heart starts responding at adregenic stimulation at 4 dpf. They concluded that this reflects the onset of the cardiovascular regulation by the autonomic nervous system. From the age of 2dpf Elbert et al. (2005) report the importance of calcium extrusion in establishing the rhythm of embryonic heartbeats. Milan et al. (2003) report a series of molecules that affect heart rate at the age of 48 hpf when the heart exist of two chambers. However to our knowledge nothing is written about heart rate regulation prior to valve formation.

Physiological parameters are plotted in Figure 10-8 and Figure 10-9.

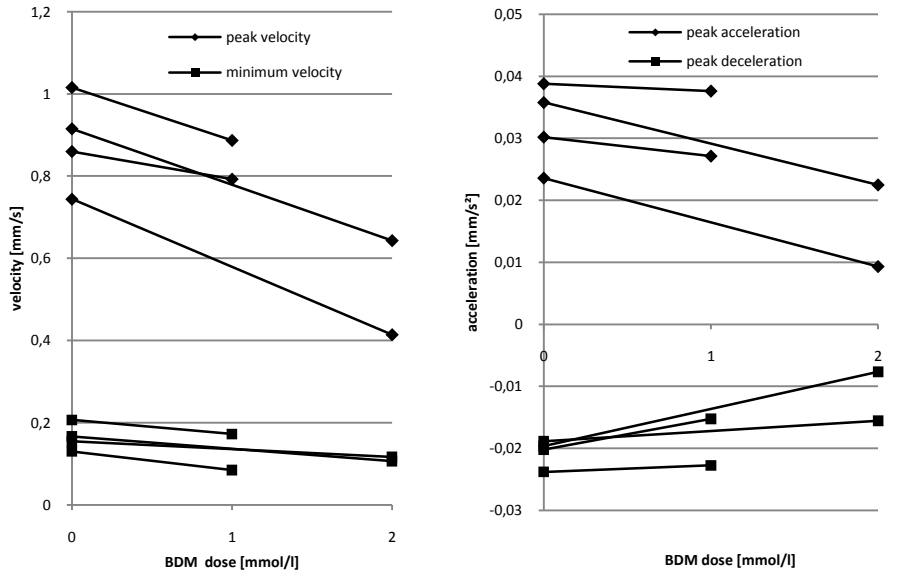

Figure 10-8. Velocity and acceleration in relation to BDM dose. Markers represent individual measurements.

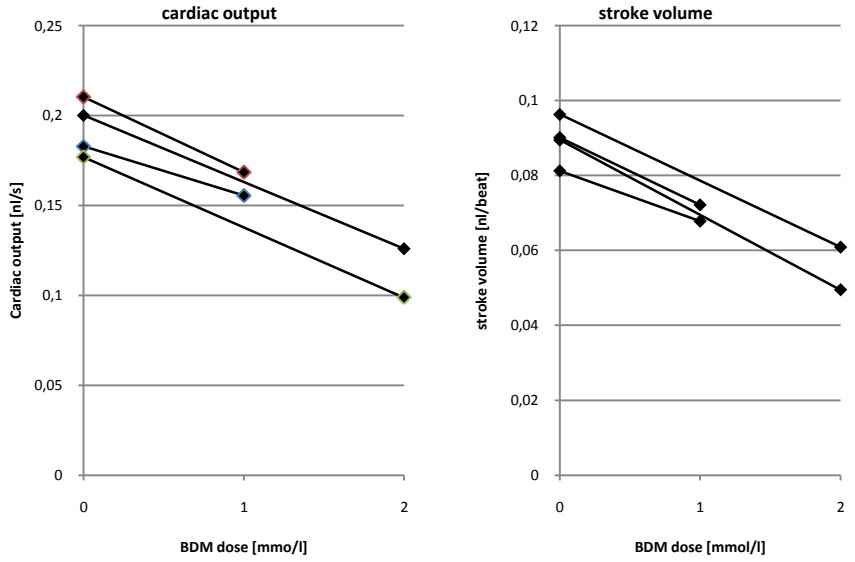

Figure 10-9. Cardiac output and stroke volume in relation BDM dose. Markers represent individual measurements.

Increasing dose of BDM causes a decreasing trend in maximal velocity, peak acceleration and stroke volume. According to Table 10-2 the decrease of all these measures is related to heart failure. Interesting is the decrease of minimal velocity insinuating valve problems. Since valves are not present it might be that the heart

wall is not fully occluded at the contraction site and backflow occurs. All these effects together result in a decrease in stroke volume.

The decreasing peak deceleration is related to decreasing vascular tone and is in accordance with the decreasing effect on blood pressure reported by Xiao and McArdle (1995).

10. 5. CONCLUSIONS

We applied the µDPIV method to estimate velocity of zebrafish embryos between 28 and 34 hpf and noticed that these embryos undergo rapid changes in heart development. In a six hour window we found that the heart function changes in following aspects:

- Increasing contractility especially when heart looping starts
- Increasing contraction wave speed in the first part of the heart

BDM is a drug that causes the heart muscle cells not to respond to the electrical signal of the heart. Our measurements demonstrate that it causes heart failure. The following changes occurred:

- General decrease in heart function caused by
    - Lower contractility
    - Lower degree of occlusion
    - Lower stroke volume
- No change in heart rate

10. 6. REFERENCES

Bagatto, B. and W. Burggren (2006). "A three-dimensional functional assessment of heart and vessel development in the larva of the zebrafish (Danio rerio)." Physiological and Biochemical Zoology **79**(1): 194-201.

Brixius, K. and R. H. G. Schwinger (2000). "Modulation of cross-bridge interaction by 2,3-butanedione monoxime in human ventricular myocardium." Naunyn-Schmiedebergs Archives of Pharmacology **361**(4): 440-444.

Chi, N. C., R. M. Shaw, B. Jungblut, J. Huisken, T. Ferrer, R. Arnaout, I. Scott, D. Beis, T. Xiao, H. Baier, L. Y. Jan, M. Tristani-Firouzi and D. Y. R. Stainier (2008). "Genetic and physiologic dissection of the vertebrate cardiac conduction system." Plos Biology **6**(5): 1006-1019.

Ebert, A. M., G. L. Hume, K. S. Warren, N. P. Cook, C. G. Burns, M. A. Mohideen, G. Siegal, D. Yelon, M. C. Fishman and D. M. Garrity (2005). "Calcium extrusion is critical for cardiac morphogenesis and rhythm in embryonic zebrafish hearts." Proceedings of the National Academy of Sciences of the United States of America **102**(49): 17705-17710.

Gwathmey, J. K., R. J. Hajjar and R. J. Solaro (1991). "CONTRACTILE DEACTIVATION AND UNCOUPLING OF CROSSBRIDGES -

EFFECTS OF 2,3-BUTANEDIONE MONOXIME ON MAMMALIAN MYOCARDIUM." Circulation Research **69**(5): 1280-1292.

Hu, N. and E. B. Clark (1989). "HEMODYNAMICS OF THE STAGE-12 TO STAGE-29 CHICK-EMBRYO." Circulation Research **65**(6): 1665-1670.

Jayawant, A. M., E. R. Stephenson and R. J. Damiano (1999). "2,3-butanedione monoxime cardioplegia: Advantages over hyperkalemia in blood-perfused isolated hearts." Annals of Thoracic Surgery **67**(3): 618-623.

Jenkins, M. W., D. C. Adler, M. Gargesha, R. Huber, F. Rothenberg, J. Belding, M. Watanabe, D. L. Wilson, J. G. Fujimoto and A. M. Rollins (2007). "Ultrahigh-speed optical coherence tomography imaging and visualization of the embryonic avian heart using a buffered Fourier Domain Mode Locked laser." Optics Express **15**(10): 6251-6267.

Kopp, R., B. Pelster and T. Schwerte (2007). "How does blood cell concentration modulate cardiovascular parameters in developing zebrafish (Danio rerio)?" Comparative Biochemistry and Physiology a-Molecular & Integrative Physiology **146**(3): 400-407.

Malone, M. H., N. Sciaky, L. Stalheim, K. M. Hahn, E. Linney and G. L. Johnson (2007). "Laser-scanning velocimetry: A confocal microscopy method for quantitative measurement of cardiovascular performance in zebrafish embryos and larvae." Bmc Biotechnology **7**: 11.

Milan, D. J., T. A. Peterson, J. N. Ruskin, R. T. Peterson and C. A. MacRae (2003). "Drugs that induce repolarization abnormalities cause bradycardia in zebrafish." Circulation **107**(10): 1355-1358.

Perreault, C. L., L. A. Mulieri, N. R. Alpert, B. J. Ransil, P. D. Allen and J. P. Morgan (1992). "CELLULAR BASIS OF NEGATIVE INOTROPIC EFFECT OF 2,3-BUTANEDIONE MONOXIME IN HUMAN MYOCARDIUM." American Journal of Physiology **263**(2): H503-H510.

Schwerte, T., C. Prem, A. Mairosl and B. Pelster (2006). "Development of the sympatho-vagal balance in the cardiovascular system in zebrafish (Danio rerio) characterized by power spectrum and classical signal analysis." Journal of Experimental Biology **209**(6): 1093-1100.

Stainier, D. Y. R. and M. C. Fishman (1994). "THE ZEBRAFISH AS A MODEL SYSTEM TO STUDY CARDIOVASCULAR DEVELOPMENT." Trends in Cardiovascular Medicine **4**(5): 207-212.

Taber, L. A., J. M. Zhang and R. Perucchio (2007). "Computational model for the transition from peristaltic to pulsatile flow in the embryonic heart tube." Journal of Biomechanical Engineering-Transactions of the Asme **129**(3): 441-449.

Takasago, T., Y. Goto, O. Kawaguchi, K. Hata, A. Saeki, T. W. Taylor, T. Nishioka and H. Suga (1997). "2,3-butanedione monoxime suppresses excitation-contraction coupling in the canine blood-perfused left ventricle." Japanese Journal of Physiology **47**(2): 205-215.

Thisse, C. and L. I. Zon (2002). "Development - Organogenesis - Heart and wood formation from the zebrafish point of view." Science **295**(5554): 457-462.

Xiao, Y. F. and J. J. McArdle (1995). "Effects of 2,3-butanedione monoxime on blood pressure, myocardial Ca2+ currents, and action potentials of rats." American Journal of Hypertension **8**(12): 1232-1240.

Chapter 11 HEART WALL MOTION TO UNDERSTAND THE PUMPING MECHANISM OF EMBRYONIC HEARTS

11. 1. INTRODUCTION

As mentioned in Chapter 2 there exist two different models that describe the pumping mechanism of embryonic hearts: peristalsis and dynamic suction (Figure 8-7).

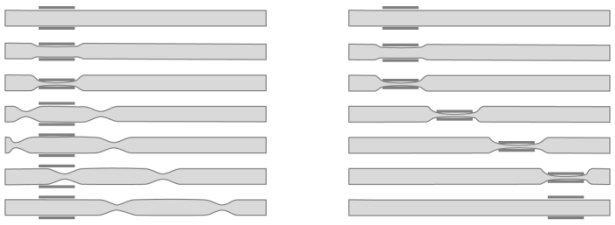

Figure 11-1 Illustration showing the working principle of dynamic suction and peristalsis in a tubular heart (after Hickerson et al. (2005))

The next two paragraphs provide a thorough introduction to understand both mechanisms; their background, their pros and contras.

11. 1. 1. The tubular heart as a peristaltic pump (Manner et al. 2010)

Visual observations of pulsating embryonic heart tubes show that their pumping action is characterized by the cyclic generation of longitudinal travelling waves sweeping from its venous (inlet) to its arterial (outlet) end. Traditionally these waves were interpreted as myocardial peristaltic waves. Historically peristalsis was broadly defined encompassing any spatially and temporally ordered sequence of muscle contractions in a unidirectional way along the length of hollow organs. According to that definition even the adult heart would perform like a peristaltic pump. During the 19th century the definition was narrowed to preferably tubular organs lacking valves showing slowly progressing contractive waves such as the gastrointestinal tract and the urethra (Manner et al. 2010).

As all definitions of peristalsis require a sequence of active contractions early research focussed on the question about the origin of the rhythmic action of the heart muscle. Two alternatives were proposed by physiologists of the 17th and 18th century (for review see Fey (1987)). The extrinsic theory, which developed later into the neurogenic theory of the heart beat, stated that myocardial contractions were guided by stimuli outside the heart within the central nervous system. The intrinsic theory

which developed later in the myogenic theory favoured the effect of local stimulation. Due to the absence of nervous elements in early stages of the embryo the first theory was discarded.

Various studies were conducted to understand this myogenic pumping action under normal and experimental conditions (for review see Kamino (1991)). The most conclusive experiments were done by Barry (1942). He discovered that if an explanted heart tube of a chick heart is dissected in multiple pieces, each of these physically isolated pieces will undergo active contractions in accordance to its location in the heart tube. The contractions are high in proximal (near the inlet) and low in distal (near the outlet) parts of the heart tube. Correspondingly Jenkins et al. (2007) recently demonstrated this *in vivo* using ultrahigh-speed optical coherence tomography. They found that the contraction of the inlet region in quail hearts is more pronounced than in the rest of the heart.

Recently imaging techniques enabled the visualisation of the conduction system in vertebrate embryonic hearts (Chi et al. 2008). For the tubular heart they report a slowly moving electrical signal in accordance to the early experiments in chick hearts (Barry 1942).

Although all these morphological arguments and studies favour peristalsis recent fluid dynamic studies reveal that the way blood is pumped through the tubular heart is not corresponding to the fluid dynamics of a peristaltic pump. Forouhar et al. (2006) therefore proposed a new mechanism capable of explaining the fluid dynamics in the heart tube.

11. 1. 2. The tubular heart as a dynamic suction pump

Forouhar et al. (2006) summed up three fluid dynamic inconsistencies for the heart being a peristaltic pump.

- Blood cell exhibits higher velocities than the velocity of the constriction site,
- Heart rate and flow rate are not linearly related
- Blood cell accelerations are highest when pressure is negative.

This last observation is only explicable by a suction mechanism.

Besides fluid dynamics that are abnormal for a peristaltic pump Forouhar et al. (2006) also reported that the endothelial wall shows a bidirectional wave. According to them these waves are initiated by a contraction close to the inlet of the heart and travel passively toward both ends of the heart tube. Since the inlet is the first region attained the wave reflects and travels toward the outlet region. Between both waves

an amount of blood – the suction bolus – is transported through the heart (Figure 8-7). This pumping mechanism requires impedance mismatches at the boundaries to induce wave reflections. The most prominent impedance mismatch is found at the inlet were a drastic change in diameter occurs.

The mechanism is based on the valveless pump discovered by Liebau (1954). The fact that this pump is used to explain aspects of the cardiovascular circulation is not new since Liebau himself used his model to explain circulation in arteries and veins (Liebau 1954; Liebau 1955a; Liebau 1955b).

Since the introduction of this mechanism as a model for the embryonic heart several experimental studies have been conducted to characterize the pumping behaviour (Hickerson et al. 2005; Bringley et al. 2008). The main findings of these investigations are listed below:

- the pump must have a flexible wall and a finite length
- there must be an impedance difference at the pumps ends
- only a small section of the pump needs to be actively contracted
- the contraction must be at an asymmetric location along the tube
- the flow generated is pulsatile
- the flow direction is dependent on location and frequency of pinching
- bidirectional waves develop in the walls of the tube
- the wall wave speed is not necessary identical to blood velocity
- there is a nonlinear relationship between frequency and flow.

All above mentioned findings could be related to the pumping mechanism and fluid dynamics of the heart tube and are in keeping with the observations of Fourohar et al. (2006).

Also other studies report findings that might support the dynamic suction pump theory. Concerning the morphological dynamics Jenkins et al. (2007) also discovered that the wave speed of the contractions in tubular quail hearts is up to four times faster in the inlet region compared to the outlet region. They called this the region of the “kick-start” which initiates a wave. This propagates then more passively through the rest of the tube while undergoing dampening. Also Hu and Clark (1989) and Hu et al. (1991) found hemodynamic data indicating that only a part of the embryonic heart is actively contributing to the pumping.

Although all these findings seem to contribute to the dynamic suction pump theory of Forouhar et al. (2006) we still have to keep in mind that there is evidence for a

conduction system running along the entire embryonic heart tube (Chi et al. 2008) suggesting that all myocardial cells might be stimulated to actively contract.

11. 1. 3. Investigation outline.

The main difference between both methods is the number of contraction sites. Dynamic suction is characterized by one while peristalsis requires multiple adjacent contractions. In case of peristalsis a governing electrical signal needs to be present to assign at what time which myocardial cells need to contract. The relation to and influence of the electrical signal is the backbone of this chapter.

We will follow two pathways in order to distinguish the pumping method in live embryos:

- Comparison of wall motion with electrical signal
- Study of the influence of BDM as a decoupling drug between muscle cells and electrical signal

11. 2. SEMI-AUTOMATED METHOD TO OUTLINE THE HEART WALL MOTION

Together with the "Vision systems" research group of Peter Veelaert (University College Ghent) we investigated if it was possible to describe features of the heart wall as series of parabolas (Deboeverie et al. 2009). We found that the method outperformed active contours (Gonzalez and Woods 2002; Liu et al. 2011) in accuracy and processing time. Although results were promising on high quality bright field images they failed on regular quality images.

Therefore, to delineate the heart wall and allow comparison, we developed a graphical user interface in Matlab (version 2008a, Mathworks, Natick, Massachusetts, U.S.A.). A Bezier spline with adjustable markers is manually plotted on the heart wall. This initial spline is then copied onto the next image where the adjustable markers are moved to match the heart wall this process is repeated for all image frames.

Although biological variation was reduced by imaging the same embryo before and after treatment with BDM, the embryo had to be removed from the microscope to be treated. As such, the position of the heart on the both the control and treated image series was slightly different. To overcome this we developed a Matlab routine that used image registration techniques. Briefly; images of the heart in end-diastole were approximately aligned using manual point markers. Then, the position and angle were adjusted using the heart as a region of interest and comparing positions and

angles by using mutual information as a similarity measure (Zitova and Flusser 2003).

11. 3. COMPARISON OF THE HEART WALL MOTION WITH THE CONDUCTION SYSTEM

As in the adult heart, active myocardial contractions in the embryonic heart are induced by an electrical signal (Moorman et al. 2004; Chi et al. 2008) beginning at the inflow of the heart, by specialised cells called the pacemaker cells. This depolarisation can be visualised as a change in intra-cellular calcium concentration. Chi and co-workers (2008) were able to use transgenic reporter constructs to convert this to an optical signal in embryonic zebrafish hearts. In Figure 11-2 we outlined the myocardial wall of the embryonic heart and pictured the calcium measurements published by Chi et al. (2008) in parallel.

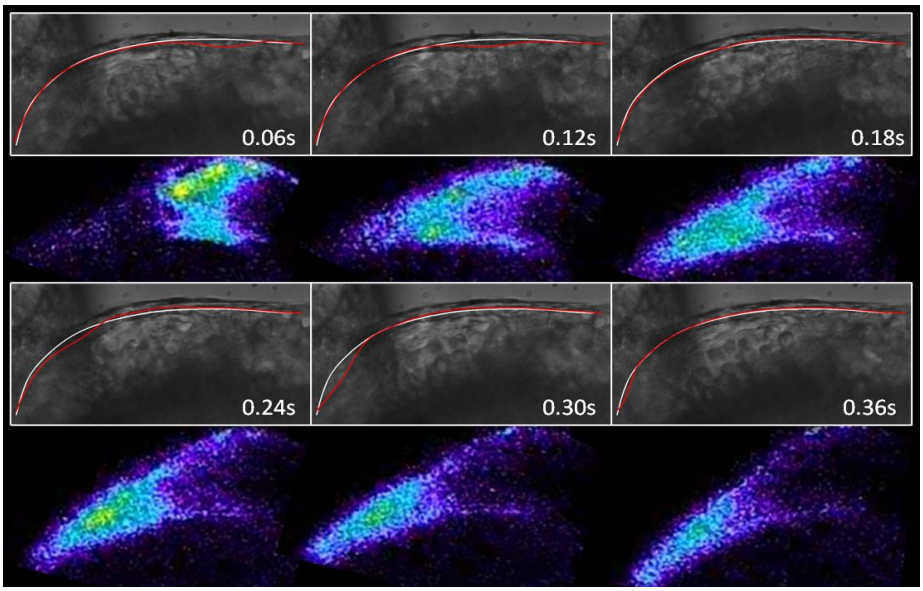

Figure 11-2. Visualization of the myocardial wall close to the embryo's chest at different time frames in the cardiac cycle. 0.00s is defined as the start of the systole, when the first movement of the myocardial wall is noticeable. The heart cycle period is 0.49s (last frames are omitted because of no apparent motion). The red line shows the position of the myocardial wall at that time frame, the white line is the position of the myocardial wall just before the onset of the systole. The calcium wave recorded by Chi et al. (2008) is pictured under the corresponding picture of the heart wall.

The myocardial wall shows a travelling wave without any disruptions. Interestingly, the myocardial wall in our embryo also closely follows the calcium wave demonstrated by Chi et al. (2008). Both the contractions we demonstrated and the calcium wave shown by Chi et al. (2008) appear to travel unidirectionally. Looking

closely one notices that the contractions with the highest amplitude are found at the inlet of the heart tube and that those are correspondingly heralded by higher concentrations in the calcium signal (green, yellow). This zone has been suggested to contain the pacemaker cells of the heart (Moorman et al. 2004).

Focussing at the calcium concentration Figure 11-2 suggests that onset of the cardiac cycle is characterized by a strong calcium signal that is damped further on. However at t = 0.24 s a strong calcium signal reappears over the ventricle.

Focussing at the heart wall we notice a remarkable accordance between calcium signal and heart wall motion. The onset shows a short contraction site with relatively high amplitude (in keeping with the strong calcium signal). Further on this contraction site broadens whilst the amplitude decreases until around t = 0.18 s (in accordance with a dampening of the calcium signal). At t = 0.18 s the amplitude of the contraction is at its lowest. At t = 0.24 s the contraction has again higher amplitude (together with a stronger calcium signal), both calcium signal and contraction amplitude decrease near the caudal end of the heart tube. At t = 0.38 s (not shown) the relaxation phase of the hearts starts.

The similarities between our measurements of the heart wall motion and the mapping of the electrical signal by Chi and co-workers, as shown in Figure 11-2 are remarkable, moreover since they were recorded in different embryos. These similarities seem to confirm that the myocardial wall is responding to the calcium wave. However, we still cannot prove this, since Chi and co-workers had to immobilize the heart wall motion using a high dose of BDM in order to be able to visualize the optical signs of the calcium signal (Chi et al. 2008).

If we reflect these findings to the model of Forouhar et al. (2006) the pacemaker cells would be the only cells which are being induced to actively contract in their dynamic suction pump hypothesis. The wall contraction generated at that point is assumed to propagate by passive wave propagation and reflection at the heart tube boundaries. From the data of Chi et al. (2008) it can be seen that indeed the pacemaker cells have the highest calcium signal. Thus the question remains: are the pacemaker cells the only cells capable of inducing a contraction, or, in order words are myocardial cells only listening to a high calcium signal?

11. 4. BDM INDUCED IRREGULARITIES ON THE HEART WALL

To give an answer to that question we investigated the influence of the drug BDM. This drug suppresses the excitation-contraction coupling in the heart (Takasago et al. 1997). This means that while the calcium signal is there, the muscle cells are

partially or not responding to that signal. Chi et al. (2008) used the same drug to arrest the heart to avoid wall motion interference while imaging calcium signal.

The velocity measurement results elucidated in chapter 10 show that BDM has the following influences on the heart function:

- No influence on heart rate
- Heart failure by decreasing the contractility
- Occlusion of the constriction probably becomes incomplete

These points seem to suggest that BDM causes the myocardial cells to be less contractile resulting in an overall drop in contraction magnitude. Outlines of the myocardial wall however contradict this hypothesis (Figure 11-3).

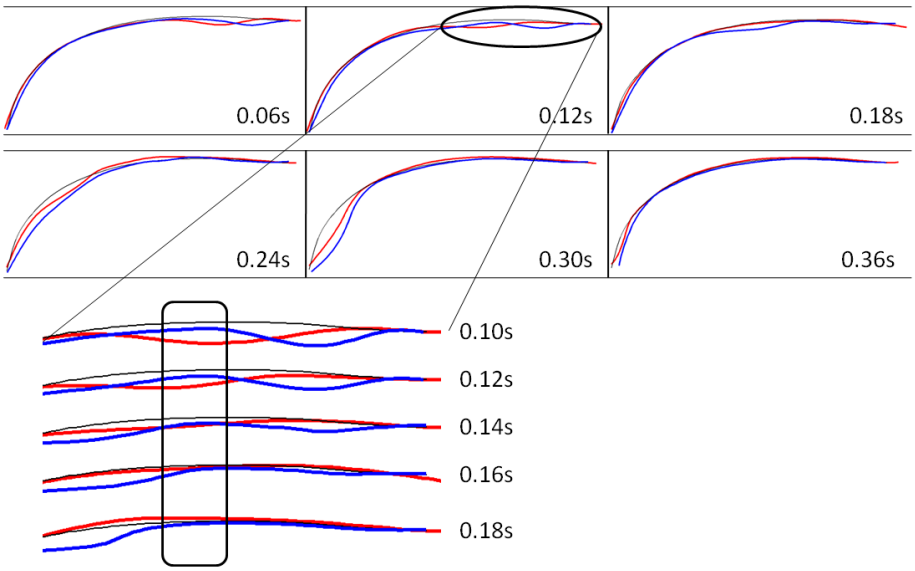

Figure 11-3. Comparison of the myocardial wall motion of a 30hpf zebrafish embryo. The red line shows the motion of the control embryo. The blue line shows the movement of the myocardial wall in the same embryo after 2 mmol BDM treatment. Reference position of the myocardial wall at the end of the diastole is colored black. The rounded rectangle in the enlargement shows a site where myocardial cells in the BDM treated embryo are not subjected to any motion.

Figure 11-3 shows that contraction amplitude (highest contraction amplitude is approximately 5 µm) of the myocardial wall is comparable before and after treatment with BDM. Comparisons of the heart wall motion show that in the proximal part (near the inlet) of the heart tube possible irregularities occur. The more distal part (near the outlet)of the heart however responds normally. Detailed observation revealed that one zone seemed not to respond to the calcium signal (blue

line in rectangle showing a non moving zone in Figure 11-3). We were able to repeat this phenomenon in two embryos (Figure 11-4).

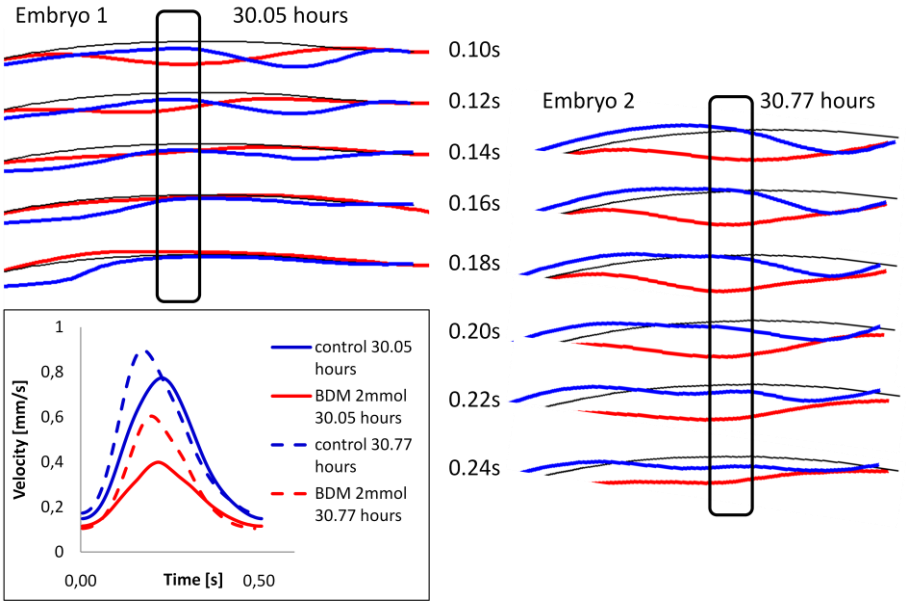

Figure 11-4 Comparison of influence of 2mmol on two different embryo's. All blue lines are control embryo, all red lines are from the same embryo but treated with BDM. Rectangle indicates the zones of no motion caused by BDM

The results depicted in Figure 11-3 and Figure 11-4 are keeping with our conclusions from the aortic velocity measurements. Contractility is indeed decreased, not on the entire myocardial wall as we excepted, but locally instead. It is indeed the non moving zone that will be the cause of an imperfect occlusion. This imperfect occlusion will cause increased backflow as also demonstrated in chapter 10. Interestingly there is a inverse correlation noticeable between the decrease in velocity and the amount of muscular response at the zone of influence. For Embryo 2 in Figure 11-4 the decrease in velocity is less pronounced, correspondingly there is still little response at the influenced zone whereas embryo 1 displaying a higher velocity decrease shows no response anymore at the influenced zone.

11. 4. 1. Experimental results contradict dynamic suction

These data of a drug induced situation are of particular interest in understanding how the heart is activated. They show in two ways that the heart cannot be a dynamic suction pump:

- If BDM would cause a decrease in contractility in a dynamic suction pump the amplitude of the (single activated) contraction would decrease resulting in waves with a lower amplitude. However this is not what is seen in our experiment.
- In recalling the mechanism proposed by Forouhar et al. (2006) the motion of heart wall cells other than the pacemaker cells is suggested to be due to passive traveling waves in the heart wall. However it is not possible to generate a stationary node within a travelling wave. For example, if a travelling wave is generated, for instance in a rope, every point of the rope must go up and down. A stationary point is impossible in a dynamic suction pump.

The zone where cells did not move is likely to be a zone where the contractile apparatus of the cells was uncoupled from the calcium signal by BDM. Of note is that the location corresponds to a zone which, in normal conditions, would be activated by relatively low calcium concentration (Figure 11-5).

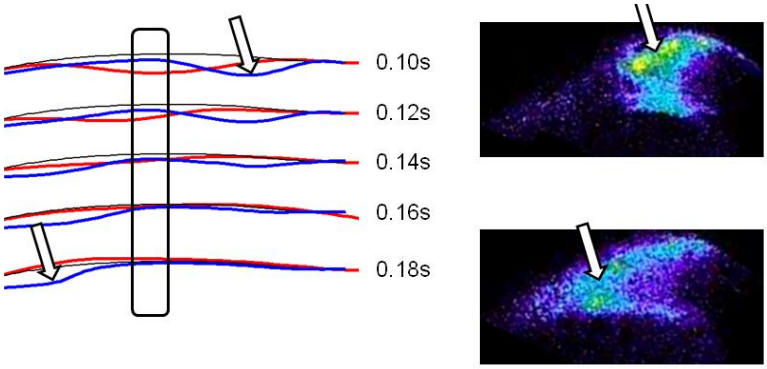

Figure 11-5. Picture demonstrating that the contraction after the zone of no motion caused by a low calcium signal. This indicates that cells not only respond to a high calcium signal caused by the pacemaker cells, suggesting that the entire myocardial wall is actively contracting.

If the myocardial cells at that location respond to low calcium concentrations it is very likely that other myocardial cells respond to the calcium signal even if this signal is not strong. This support the idea of peristaltic pumping.

11. 4. 2. Literature supports that dynamic suction is not suitable for embryonic heart pumping

Since the initial publication suggesting the embryonic heart is a dynamic suction pump (Forouhar et al. 2006) more researchers have investigated this pumping mechanism. An experimental study is performed by Hickerson et al. (2005). They showed that mean exit flow is linearly dependant on the amplitude of pinching, linearly decreasing with resistance, but non-linearly with respect to frequency of

excitation. Based on those experiments a numerical Fluid Structure Interaction (FSI) model has been developed by Avrahami and Gharib (2008) trying to mimic the pumping mechanism. They concluded that pumping is the result of a constructive wave interaction located at the extremity of the elastic tube distant to the pincher. Loumes et al. (2008) used the same model as Avrahami and Gharib (2008) but ameliorated it by modelling the influence of the cardiac jelly in the pumping mechanism. Because of the incompressible nature of the jelly layer the amplitudes of the passing waves were amplified and they could generate a higher net flow. However his results indicated a high amount of backflow every cycle, which is not consistent with visual observations in the embryonic heart. In her PhD Loumes describes the results of his model at higher frequencies of pinching and noticed that, although conditions were exactly the same as before the frequency change, flow changed direction (Loumes 2007). This would be lethal in a life embryo!

Bringley et al. (2008) also showed that this type of pumping is inefficient at low Reynolds numbers. However Reynolds numbers characteristic for flow in the zebrafish heart are in the order of 0.01-0.1, and as such much lower than the window of practical use for dynamic suction pumping.

11. 4. 3. Additional arguments against dynamic suction pumping in tubular heart stage

Besides the previous inconsistencies between characteristics of dynamic suction pumping and observations in life embryos dynamic suction pumping has some additional points which are very difficult to explain using the dynamic suction pump theory:

- During development heart rate gradually increases, according to Hu and Clark (1989) this is the result of increasing demands for nutrients. However Hickerson et al. (2005) proved the system to be resonance based. This would imply that at resonance frequency net flow would be highest. But increasing the frequency from that point on would result in a decrease in blood flow, the opposite of what the embryo needs.
- In the animal kingdom vertebrate heart size differs considerably between species. It would be a miracle to fine tune the appropriate frequency for each heart size.
- In the previous chapter we show that heart wall speed is not constant along the heart. Also Jenkins et al. (2007) demonstrated that in the avian heart wall speed is four times higher in the first halve of the heart tube. However if the wall motion would be caused by passive waves and the wave would undergo dampening this would affect its amplitude and not its wave speed.
- The working principle of dynamic suction is based on an eccentric location of active contraction producing waves traveling in both directions. This

stage however needs to develop in a geometry with atrial and ventricular contraction. Thus two locations of active contraction each causing waves traveling in both directions. It is very unlikely that in such conditions a suction bolus would be created or persist.

- During development the wave speed along the heart needs to change from a more constant to a phase like motion (first atrial cells then a little pause and then ventricle cells) needed for chamber pumping. This transition is impossible without a governing electrical signal.
- During looping the curvature of the heart increases meaning that the outer curvature myocardial wall is longer than at the inner curvature myocardial wall. In case of passive traveling waves this could result in non matching occlusions since it takes longer for the wave to travel the outer curvature than the inner curvature. However a very interesting study analytically showed that light to moderate curvature increases pumping efficiency of peristaltic pumping (Jaffrin 1973). This article shows that backflow is decreased with increasing curvature, meanwhile it gives a possible explanation why the hearts starts bending upon itself.

Liu suggested that peristaltic activation might be energetically less favourable than dynamic suction (Liu et al. 2009). However, as resonance based systems are prone to instabilities when changes occur, dynamic suction pumping may be undesirable during a period of rapid embryonic growth. Here is once more an example where nature chooses stability (peristalsis) in favour of energy cost which in case of a vital organ like the heart is for sure a genius choice

11. 5. A HYPOTHETICAL MODEL THAT COMBINES FLOW CHARACTERISTICS WITH WALL CHARACTERISTICS BASED ON THE INFLUENCE OF THE CARDIAC JELLY

In the previous part we proved that the myocardial wall is actively contracting and that these active contractions are guided by the electrical signal of the heart. This is clearly peristalsis. However Forouhar and co-workers (2006) performed several interventions to prove the hypothesis of a dynamic suction pump. They showed that:

- during contracting, the distance between the endothelial and myocardial wall increases
- there is a non-linear relationship between cardiac flow and heart rate.
- blood cells are moving faster than the contraction site
- blood cell accelerations are highest when pressure is negative, suggesting a suction effect.

Although all these arguments seem to favour the dynamic suction pump theory we believe they are all directly or indirectly linked to the presence of the cardiac jelly regardless of any pumping mechanism.

The cardiac jelly is a gelatinous, acellular, extracellular matrix lying between the endothelial lining and the myocardial layer of the hearts at early stages of heart development. It contains numerous molecules playing an important role in the regulation of cellular events (Bowers et al. 2010; Lockhart et al. 2011). Most studies about the role of the cardiac jelly in early cardiac development focus on cushion formation and the steps of cells migration and tissue remodelling resulting in valve formation (Schroeder et al. 2003; Butcher and Markwald 2007; Butcher et al. 2007).

Barry (1948) was the first to assume that the cardiac jelly assists in the pumping mechanism. He reasoned that a myocardial shortening of 20% would never be enough to result in full closure upon contraction. In a thick-walled tube made by an incompressible material that transmit the force of the contraction, full closure can also occur in tubes with larger diameters. For this reasoning being valid one must assume that the cardiac jelly has little longitudinal mobility. Therefore its volume will be almost identical before and after contraction resulting in the situation shown in Figure 11-6. This also explains why the cardiac jelly thickens when compressed.

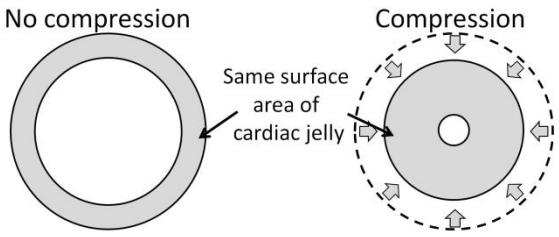

Figure 11-6. Illustration explaining how the cardiac jelly assists in the pumping mechanism. Meanwhile the illustration shows why the cardiac jelly thickens when compressed.

Loumes et al. (2008) modeled a multilayer impedance pump. Interestingly their results also show that at the location of active contraction the cardiac jelly was thicker than during non contraction. However the simulations show only a minor rise of contraction amplitude because they modeled the cardiac jelly as a viscous material which inherently include longitudinal motion. To prevent this motion a matrix should be present in the cardiac jelly.

A study by Manner et al. (2008) showed that the cardiac jelly indeed causes a different deformation of the endothelial layer compared to the circular deformation of the myocardial layer. Besides causing different flow patterns it also indicates that the cardiac jelly must have a matrix.

The presence of a matrix can be derived from the behavior of the cardiac jelly during pumping. We therefore used the movies created by Forouhar and co-workers as input data (Forouhar et al. 2006). We outlined the myocardial wall and the

endothelial wall and noticed that both walls move accordingly. A selection of frames is displayed in Figure 11-7.

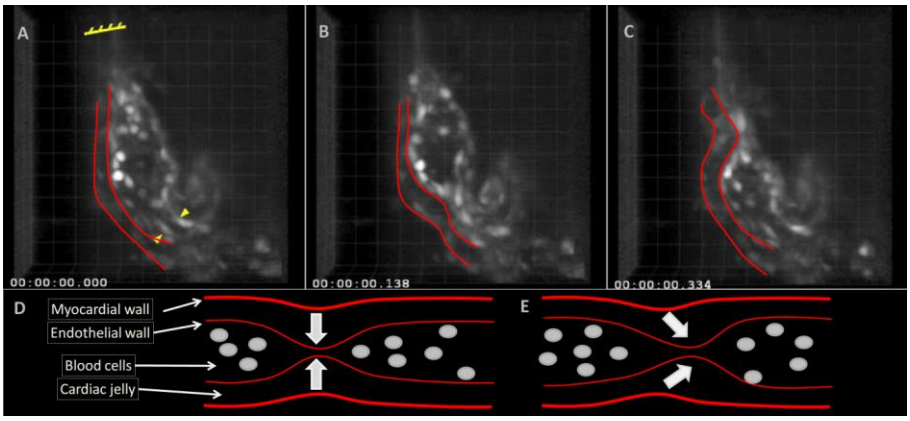

Figure 11-7. Key frames taken from a movie created by Forouhar et al. (2006). (republished with permission). Red lines represent the outer layer of the endocardial wall and the outer layer of the myocardial wall. In the first frame A at the onset of the systole both lines are almost parallel. Figure B and C show situations where the cardiac jelly responds asymmetrically upon contraction. In B the endothelial wall proceeds the contraction site. In C the situation is opposite to B. In both B and C at the location of the contraction the distance between both layers is greater than at the onset of the cycle (A). D and E show the difference between a normal contraction (D) and a contraction where the cardiac jelly responds asymmetrically (E).

The frames in Figure 11-7 show that apart from a symmetric contraction (Figure 11-7 D) asymmetries occur (Figure 11-7 B and C) during the heart cycle. Of particular interest is the asymmetry in Figure 11-7 B. The cardiac jelly is pushed sideways against the force induced by the pressure difference over the contraction. We hypothesize that this is caused by the presence of a molecular matrix.

An interesting article reveals that indeed elastic molecules like emilin and fibrilin are present in the cardiac jelly, whereas elastin and collagen are not present at that stage (Hurle et al. 1994). However very little is known about the exact impact of those molecules on mechanical behaviour of the heart (Fomovsky et al. 2010). Despite this, matrix forming molecules collagen and scaffolding proteins such as titin are known to cause recoil in the adult heart (Granzier and Irving 1995; Opitz et al. 2003). This recoil is believed to induce suction during diastole in the adult heart (Zhang et al. 2008). Since emilin and fibrilin are described to have an elastic nature we hypothesize that the suction phenomenon seen by Forouhar et al. (2006) is induced by recoil of the highly deformed cardiac jelly. This suction inducing recoil of the cardiac jelly and annex myocardial wall explains the velocities of the blood cells being higher than the propagation of the contraction site and the maximal acceleration being maximal when pressure is negative.

A possible explanation of the nonlinear relationship between heart rate and cardiac flow might be found in asymmetric behavior of the cardiac jelly upon compression. The extreme situations of asymmetry plotted in Figure 11-7 B and C occur when displacements of the myocardial and endothelial wall are high. In these extreme situations the cardiac jelly is pushed sideways from the contraction of the myocardial wall. The places where this phenomenon happens must be guided by an interplay of material properties of the cardiac jelly and the fluid-mechanical environment of the blood. When one changes for example the temperature, like Forouhar and coworkers (2006) did to change the heart rate of the embryo, it is very likely that this would change the material properties of not only the entire vascular system but also of the cardiac jelly. Thus, it cannot be excluded that a change of temperature combined with a change of heart rate could alter the locations and time points where and when the cardiac jelly is pushed sideways from the contraction site. As described higher in the article relative small changes in the activation of the myocardial wall, induced by a low dose of BDM, caused a drop of almost 50 % in cardiac output. It is therefore plausible that changes in longitudinal displacements of the cardiac jelly could result in significant changes in cardiac flow, moreover their influence is likely to cause a nonlinear relation with heart rate.

11. 6. CONCLUSIONS

We used two pathways to understand the pumping mechanism of embryonic vertebrate hearts.

- Comparison of the electrical signal with muscle contraction
- Drug induced anomalies to exclude one of the pumping mechanisms

Both ways pointed out that the heart is peristaltically activated:

- Muscle cells follow the electrical signal remarkably well
- The drug induced anomalies did not give the outcome we would expect from a dynamic suction pump but created a non moving zone in the myocardial wall which is an impossible situation in a dynamic suction pump

To match the flow characteristics uncommon for peristalsis with the observed peristaltic wall motion, we propose a new model. In this model the cardiac jelly increases the pumping efficiency and induces suction because of the elastic recoil.

11. 7. REFERENCES

Avrahami, I. and M. Gharib (2008). "Computational studies of resonance wave pumping in compliant tubes." Journal of Fluid Mechanics **608**: 139-160.

Barry, A. (1942). "The intrinsic pulsation rates of fragments of the embryonic chick heart." Journal of Expermental Zoology **91**: 119-130.

Barry, A. (1948). "The functional significance of the cardiac jelly in the tubular heart of the chick embryo." anat rec **102**.

Bowers, S. L. K., I. Banerjee and T. A. Baudino (2010). "The extracellular matrix: At the center of it all." Journal of Molecular and Cellular Cardiology **48**(3): 474-482.

Bringley, T. T., S. Childress, N. Vandenberghe and J. Zhang (2008). "An experimental investigation and a simple model of a valveless pump." Physics of Fluids **20**(3): 15.

Butcher, J. T. and R. R. Markwald (2007). "Valvulogenesis: the moving target." Philosophical Transactions of the Royal Society B-Biological Sciences **362**(1484): 1489-1503.

Butcher, J. T., T. C. McQuinn, D. Sedmera, D. Turner and R. R. Markwald (2007). "Transitions in early embryonic atrioventricular valvular function correspond with changes in cushion biomechanics that are predictable by tissue composition." Circulation Research **100**(10): 1503-1511.

Chi, N. C., R. M. Shaw, B. Jungblut, J. Huisken, T. Ferrer, R. Arnaout, I. Scott, D. Beis, T. Xiao, H. Baier, L. Y. Jan, M. Tristani-Firouzi and D. Y. R. Stainier (2008). "Genetic and physiologic dissection of the vertebrate cardiac conduction system." Plos Biology **6**(5): 1006-1019.

Deboeverie, F., F. Maes, P. Veelaert, W. Philips and Ieee (2009). LINKED GEOMETRIC FEATURES FOR MODELING THE FLUID FLOW IN DEVELOPING EMBRYONIC VERTEBRATE HEARTS. New York, Ieee.

Fomovsky, G. M., S. Thomopoulos and J. W. Holmes (2010). "Contribution of extracellular matrix to the mechanical properties of the heart." Journal of Molecular and Cellular Cardiology **48**(3): 490-496.

Forouhar, A. S., M. Liebling, A. Hickerson, A. Nasiraei-Moghaddam, H. J. Tsai, J. R. Hove, S. E. Fraser, M. E. Dickinson and M. Gharib (2006). "The embryonic vertebrate heart tube is a dynamic suction pump." Science **312**(5774): 751-753.

Fye, W. B. (1987). "THE ORIGIN OF THE HEART BEAT - A TALE OF FROGS, JELLYFISH, AND TURTLES." Circulation **76**(3): 493-500.

Gonzalez, R. C. and R. E. Woods, Eds. (2002). Digital Image processing, Prentice Hall.

Granzier, H. L. and T. C. Irving (1995). "PASSIVE TENSION IN CARDIAC-MUSCLE - CONTRIBUTION OF COLLAGEN, TITIN, MICROTUBULES, AND INTERMEDIATE FILAMENTS." Biophysical Journal **68**(3): 1027-1044.

Hickerson, A. I., D. Rinderknecht and M. Gharib (2005). "Experimental study of the behavior of a valveless impedance pump." Experiments in Fluids **38**(4): 534-540.

Hu, N. and E. B. Clark (1989). "HEMODYNAMICS OF THE STAGE-12 TO STAGE-29 CHICK-EMBRYO." Circulation Research **65**(6): 1665-1670.

Hu, N., D. M. Connuck, B. B. Keller and E. B. Clark (1991). "DIASTOLIC FILLING CHARACTERISTICS IN THE STAGE-12 TO 27 CHICK-EMBRYO VENTRICLE." Pediatric Research **29**(4): 334-337.

Hurle, J. M., G. T. Kitten, L. Y. Sakai, D. Volpin and M. Solursh (1994). "ELASTIC EXTRACELLULAR-MATRIX OF THE EMBRYONIC

CHICK HEART - AN IMMUNOHISTOLOGICAL STUDY USING LASER CONFOCAL MICROSCOPY." Developmental Dynamics **200**(4): 321-332.

Jaffrin, M. Y. (1973). "INERTIA AND STREAMLINE CURVATURE EFFECTS ON PERISTALTIC PUMPING." International Journal of Engineering Science **11**(6): 681-699.

Jenkins, M. W., D. C. Adler, M. Gargesha, R. Huber, F. Rothenberg, J. Belding, M. Watanabe, D. L. Wilson, J. G. Fujimoto and A. M. Rollins (2007). "Ultrahigh-speed optical coherence tomography imaging and visualization of the embryonic avian heart using a buffered Fourier Domain Mode Locked laser." Optics Express **15**(10): 6251-6267.

Kamino, K. (1991). "OPTICAL APPROACHES TO ONTOGENY OF ELECTRICAL-ACTIVITY AND RELATED FUNCTIONAL-ORGANIZATION DURING EARLY HEART DEVELOPMENT." Physiological Reviews **71**(1): 53-91.

Liebau, G. (1954). "Arterielle und venöse Repulsation." Zeitschr f Gesamte Med **123**: 71-90.

Liebau, G. (1954). "Über ein Ventilloses pumpprinzip." Naturwissenschaften **41**: 327.

Liebau, G. (1955a). "Herzpulsation und Blutbewegung." Zeitschr f Gesamte Med **125**: 482-489.

Liebau, G. (1955b). "Strömungsprinzipien des Herzens." Zeitschr f Kreislaufforschung **44**: 677-684.

Liu, A. P., R. K. K. Wang, K. L. Thornburg and S. Rugonyi (2009). "Dynamic variation of hemodynamic shear stress on the walls of developing chick hearts: computational models of the heart outflow tract." Engineering with Computers **25**(1): 73-86.

Liu, C., F. Dong, S. Zhu, D. Kong and K. Liu (2011). "New Variational Formulations for Level Set Evolution Without Reinitialization with Applications to Image Segmentation." Journal of Mathematical Imaging and Vision **41**(3): 194-209.

Lockhart, M., E. Wirrig, A. Phelps and A. Wessels (2011). "Extracellular Matrix and Heart Development." Birth Defects Research Part a-Clinical and Molecular Teratology **91**(6): 535-550.

Loumes, L. (2007). Multilayer impedance pump: a bio-inspired valveless pump with medical applications. California insitute of Technology. Pasadena. **PhD:** 114.

Loumes, L., I. Avrahami and M. Gharib (2008). "Resonant pumping in a multilayer impedance pump." Physics of Fluids **20**(2): 11.

Manner, J., L. Thrane, K. Norozi and T. M. Yelbuz (2008). "High-resolution in vivo Imaging of the cross-sectional deformations of contracting embryonic heart loops using optical coherence tomography." Developmental Dynamics **237**(4): 953-961.

Manner, J., A. Wessel and T. M. Yelbuz (2010). "How Does the Tubular Embryonic Heart Work? Looking for the Physical Mechanism Generating Unidirectional Blood Flow in the Valveless Embryonic Heart Tube." Developmental Dynamics **239**(4): 1035-1046.

Moorman, A. F. M., A. T. Soufan, J. Hagoort, P. A. J. De Boer and V. M. Christoffels (2004). Development of the building plan of the heart. Cardiac

Engineering: From Genes and Cells to Structure and Function. S. Sideman and R. Beyar. New York, New York Acad Sciences. **1015:** 171-181.

Opitz, C. A., M. Kulke, M. C. Leake, C. Neagoe, H. Hinssen, R. J. Hajjar and W. A. Linke (2003). "Damped elastic recoil of the titin spring in myofibrils of human myocardium." Proceedings of the National Academy of Sciences of the United States of America **100**(22): 12688-12693.

Schroeder, J. A., L. F. Jackson, D. C. Lee and T. D. Camenisch (2003). "Form and function of developing heart valves: coordination by extracellular matrix and growth factor signaling." Journal of Molecular Medicine-Jmm **81**(7): 392-403.

Takasago, T., Y. Goto, O. Kawaguchi, K. Hata, A. Saeki, T. W. Taylor, T. Nishioka and H. Suga (1997). "2,3-butanedione monoxime suppresses excitation-contraction coupling in the canine blood-perfused left ventricle." Japanese Journal of Physiology **47**(2): 205-215.

Zhang, W., C. S. Chung, L. Shmuylovich and S. J. Kovacs (2008). "Is left ventricular volume during diastasis the real equilibrium volume, and what is its relationship to diastolic suction?" Journal of Applied Physiology **105**(3): 1012-1014.

Zitova, B. and J. Flusser (2003). "Image registration methods: a survey." Image and Vision Computing **21**(11): 977-1000.

Chapter 12 GENERAL CONCLUSIONS AND FUTURE PERSPECTIVES OF PART B

The first section of this chapter summarizes the content of this investigation part. The most important conclusions are highlighted and discussed in relation to the goals of this investigation. The second part indicates some perspectives for future research.

12. 1. SUMMARY AND CONCLUSIONS

More than 20 years of genetic research in heart development drastically increased our understanding and deepens our appreciation for the marvellously intelligent design of the heart. However today the pumping mechanism is still a subject of debate. This investigation part is therefore dedicated to reveal how embryonic hearts in tubular heart stage pump and the impact on the flow generated in the aorta.

This investigation focussed on two parts. Firstly a method for estimating aortic blood velocity is developed and tested. Parameters were derived in order to understand the changes in pumping capacity during development and under the influence of drugs . Secondly the heart wall motion is used to understand the pumping mechanism. Because of the micro scale direct measurement of flow is impossible. Therefore we made use of microscopic images and image processing techniques.

After the introductory chapters, chapter 3 describes different methods for fast and accurate blood velocity estimation that can be used on standard bright field microscopic images. All methods were compared to manual tracking set as ground truth. From the comparison tests it can be concluded that:

- The linescan method and the cell detection and tracking method failed to capture high velocities correctly
- Micro digital particle image velocimetry (µDPIV) based methods outperform all other methods in processing time and accuracy.
- For the µDPIV based methods three different similarity measures were evaluated. Mutual information was found to be the most accurate but extensive testing showed that Sum of Absolute Differences is capable of capturing a broader velocity range.

In chapter 4 the blood velocity estimating methods were used to investigate the influence of age on heart performance during development. And to identify the influence of 2,3-butadionemonoxime (BDM) a drug that uncouples the muscles from the electric signal of the heart. From the results we could conclude that:

- During a 6 hour period the maximal velocity and peak acceleration increase. This indicates an increase in heart contractility
- During development the velocity wave tends to becomes more asymmetric indicating an increase in wave speed in the first halve of the heart. This could be seen as a start of the development into chamber pumping
- BDM causes general heart failure characterized by lower contractility, incomplete occlusion at the constriction location and lower stroke volume. Heart rate is however not affected.

Chapter 5 is dedicated to study of the pumping mechanism of the tubular embryonic heart. To distinguish which one of the two pumping models (peristalsis versus dynamic suction) is correct we focused at the number of active contraction locations. This was done in two ways. First we compared the myocardial wall motion with the electrical signal recorded by (Chi et al. 2008). Secondly we used small doses of BDM to induce heart failure. From the results the following conclusions were drawn:

- Muscle cells follow the electrical signal remarkably well suggesting active contraction and thus peristalsis
- The drug induced anomalies did not give the outcome we would expect from a dynamic suction pump but created a non moving zone in the myocardial wall which is an impossible situation in a dynamic suction pump

Chapter 5 continues with the proposition of a hypothetical model aiming to match the flow characteristics which are contradictory for peristalsis with the observed peristaltic wall motion. In that model the cardiac jelly is a buffer zone between the driving myocardial wall and the endothelial wall in contact with the blood. It amplifies the contraction and causes suction induced through recoil.

12. 2. SUGGESTIONS FOR FURTHER RESEARCH

12. 2. 1. Blood velocity estimation

The blood velocity estimations algorithms are a very powerful tool. They could be used for heart performance characterization for heart development research or large scale drug tests. For easy development and testing the scripts are written in Matlab. This calculation package is not very commonly used in biological research it may therefore be desirable to rewrite the algoritms for a package as ImageJ.
The current algorithms only work on blood vessels. For investigation of blood flow in the heart additional scripts have to be developed to remove the moving heart wall from the image.

12. 2. 2. Heart pumping mechanism

We created a situation that is not explicable by dynamic suction pumping. Additional proof could be assembled by the following experiments.

- Put weight on an explanted heart. If the wave is passing the imposed weight contraction must be active past the location of the imposed weight
- Create a CFD model based on the endothelial wall motion.
    - Investigate pressure magnitudes on the wall: high pressures are likely to be caused by active contraction

Such CFD models are not yet reported in literature. One model is described in the PhD thesis of Heeboll-Christensen (2011). He implemented a model using Matlab. Input for the model were optical coherence tomography images of chick embryos. However the solver of Matlab was not powerful enough to generate results within reasonable time.

To fully clarify the role of the cardiac jelly in the flow inconsistencies further investigation is needed.
We suggest the following:

- 4D (3D + time) visualization of a beating heart if possible with a fluorescent myocardial and endothelial wall:
    - Investigate motion of both walls
    - Investigate possible role of the cardiac jelly
- Create a CFD model of a peristaltic pumping heart with and without a cardiac jelly layer and compare fluid motion in both situations.
- Create a setup that actively control the frequency of the electrical signal in order to investigate flow – frequency relations without changing the material properties of the heart.

12. 3. REFERENCES

Chi, N. C., R. M. Shaw, B. Jungblut, J. Huisken, T. Ferrer, R. Arnaout, I. Scott, D. Beis, T. Xiao, H. Baier, L. Y. Jan, M. Tristani-Firouzi and D. Y. R. Stainier (2008). "Genetic and physiologic dissection of the vertebrate cardiac conduction system." Plos Biology **6**(5): 1006-1019.

Heeboll-christensen (2011). mathematical models of flow characteristics in the embryonic heart. Department of science, Systems and Models. Roskilde, Roskilde University. **PhD**.

The book you just read tries to give an answer of how things work. And indeed that is what research is all about. All investigations start in one way or another with a question HOW; how does this work? How does it develop? How can we model it? How can we use it? But is this what we really should care about?

The first question word probably all us mentioned is not 'how'. Try to remember… if you have children in the age of two, or now somebody who has, what do they ask? Not HOW but WHY. They ask it so often that parents become crazy of it. A lot of their and probably also our questions often remain unanswered as we learn to adapt to the 'important' or the 'adult' world. But the instinctive urge of asking questions remains. We of course as adults have to come up with a way to answer our own questions and, admit it, it doesn't feel good when you, time after time, are not able to answer a question.

So what did we as 'smart', 'intelligent', 'scientific' persons do? We changed the type of question. We changed "why" in "how". We created a complete scientific environment around it. We even were able to lift it to a standard. People look up to science. People even start to believe that science will provide the answers and come up with solutions for the problems we face in our world today.

But, how satisfying are "how"-questions, even if we are able to answer them? As people grow older, retire, take more distance from the hectic world, often they spend time to think, think about the simple things in live: a friendly smile, a warm handshake. If you have something very important to ask them will your question start with how? Do you think they bother about how? Somehow we see persons with a lifetime of experience as persons who might have sensed the meaning of life. In one way we hope that they found answers to: why are we here, why is there so much misery, why do we die…? Because if they haven't, how will we ever find answers to those questions we try to suppress so hard?

So keep asking WHY, don't stop, and maybe you might discover that answers are often closer and far more simple than we think. But it will require a very difficult attitude: humility.

Draw close to God,
and he will draw close to YOU
James 4:8